Characterization of Unsteady Flow Processes in a Centrifugal Compressor Stage

by

Kenneth A. Gould

B.S. (Mechanical Engineering) Carnegie Mellon University (2000)
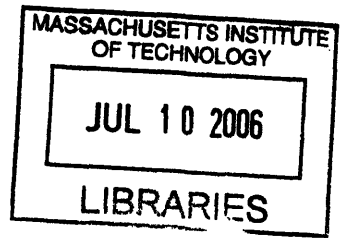
Submitted to the Department of Aeronautics and Astronautics in partial fulfillment of the degree of

Master of Science

at the

MASSACHUSETTS INSTITUTE OF TECHNOLOGY

February 2006

Author... 2/3/2006 ....
Department of Aeronautics and Astronautics
February, 2005

Certified by..
Choon S. Tan
Senior Research Engineer, Gas Turbine Laboratory
Thesis Supervisor

Certified by..
Jaime Peraire
Professor of Aeronautics and Astronautics
Chair, Committee on Graduate Students

Characterization of Unsteady Flow Processes in a Centrifugal Compressor Stage

by

Kenneth A. Gould

Submitted to the Department of Aeronautics and Astronautics
on February 3rd, 2006 in partial fulfillment of the
requirements for the degree of
MASTER OF SCIENCE

Abstract

Numerical experiments have been implemented to characterize the unsteady loading on the rotating impeller blades in a modern centrifugal compressor. These consist of unsteady Reynolds-averaged Navier Stokes simulations of three-dimensional and quasi-two dimensional approximate models. The interaction between the rotating impeller and the stationary downstream diffuser has been identified as strong source of unsteady loading on the impeller blades. First of a kind unsteady calculations haven been carried out to elucidate an upstream manifestation of a downstream stimulus experienced in a particular centrifugal compressor stage. Here the upstream manifestation is the considerable unsteady loading in the splitter blade leading edge while the downstream stimulus is the unsteady impeller-diffuser interaction

Three key parameters that control the level and extent of the unsteady loading are the impeller-diffuser gap, stage loading, and the impeller passage relative Mach number. Impeller-diffuser gap has been shown to control the peak level of unsteady loading on the blade. Stage loading has been shown to control the upstream attenuation of the loading. A hypothesis has been put forward that increased diffusion associated with increased stage loading increases the impeller sensitivity to the downstream disturbance. The relative Mach number has been shown to set the chordwise distribution of the unsteady load on the blade.

Unsteady blade loading has been computed through a quasi two-dimensional model in which an unsteady pressure boundary condition is imposed at the impeller exit to approximate the presence of the downstream diffuser. Results of this approximate model have been shown to yield unsteady loading characteristics that are in accord with the full three-dimensional unsteady model. An implied utility of this result is that a quasi-2D approximation could be used during the design phase to approximate the unsteady loading in a timeframe that is compatible with the design environment. The effect of unsteady flow on mass flow capacity of a fluid device is eliminated as a source for over-predictions in mass flow when a steady-state approximation is used.

Thesis Supervisor: Dr. Choon S. Tan
Title: Senior Research Engineer, Gas Turbine Laboratory

Acknowledgements

I would like to thank my advisors for their outstanding support throughout this process, without whom I would not have been able to complete this work. Dr. Choon Tan of the Gas Turbine Lab at MIT has provided excellent guidance and greatly enhanced my learning experience at MIT. Dr. Michael Macrorie of General Electric has been very generous by offering his time to review my work and provide valuable insight and direction to the research.

I would also like to thank Professor Edward Greitzer for offering his advice and encouraging me to focus on the important concepts. Also Professor Nicholas Cumpsty for reviewing the research and providing suggestions.

I would like to thank GE's management for allowing me to pursue this degree while employed at GE. Both Byron Pritchard and Spiro Harbilas have been very accommodating during this time. I would also like to thank Mark Pearson, Aspi Wadia, Fred Pineo, Bob Tameo, Bob Kursmark, and George Pultz for supporting the public release of the results along the way. I also appreciate the counsel of several GE engineers, namely Bill Steyer, Zee Moussa, Bob Walters, Jeff Nussbaum, Carrie Granda, and Basu Srivastava...all of whom have been very willing to share their knowledge.

I also must thank my friends who were also willing to spent hours discussing our research and providing feedback, namely Brenden Epps, Curtis Moeckel, and Will DeShazer.

My girlfriend Katie has been very patient and willing to help me through this process, which is very much appreciated. Thanks also to my sister Laura for keeping the pressure on me to finish this thesis. Most of all I would like to thank my parents Chuck and Angel for giving me the encouragement and constant support throughout my entire academic career.

Table of Contents

Nomenclature

Subscripts
1: Impeller Inlet
2: Impeller Exit
3: Diffuser exit
n: Normalized by reference value

Symbols
A: area
c: wave speed
Closs: Diffuser loss coefficient
Cp: Pressure recovery factor
f: frequency
k: Harmonic number
L*:   Distance from impeller trailing edge where disturbance is 50% of peak value
$\dot{m}$:   mass flow rate
$\dot{m}_a$:   mass flow rate per unit area
$\dot{m}_{ca}$:   Normalized corrected mass flow rate per unit area (referred to as "mass flow")
M: Mach Number
N_d: Number of diffuser vanes
N_i: Number of impeller splitter blades
NPR: Nozzle pressure ratio
P_{amb}:   Ambient static pressure
P_n: Static pressure difference from rotor inlet, normalized by tip dynamic head
P_s: Static pressure
P'_s: Normalized static pressure delta from the local time-averaged value
P_t: Total Pressure
P_f: Static pressure fluctuation over 1 period of time
r: Diffuser radial position, measured from impeller trailing edge
S: Streamwise position from impeller inlet to impeller exit
t: Time
Tt: Total temperature
Ts: Static temperature
u: Velocity in absolute frame
w: Velocity in relative frame

Greek
α_1:   Impeller absolute frame inlet flow angle
α_2:   Impeller absolute frame exit flow angle
β: Reduced frequency
β_1:   Impeller relative frame inlet flow angle
β_2:   Impeller relative frame exit flow angle
Δ: Difference from a baseline value

8

$\Delta \dot{m}_a$: Percent Difference (between time-averaged and steady-state corrected mass flow)

ΔLs: Difference in maximum and minimum splitter load during 1 period of revolution

π: Pressure ratio

η: Adiabatic efficiency

λ: Diffuser pitch

θ: Circumferential angle relative to top-dead-center

ρ: Density

τ: Characteristic period

τ_{imp}: Impeller temperature ratio

ω: Frequency

Ω: Rotational speed

Expressions

1-D: One-dimensional

2-D: Two-dimensional

3-D: Three-dimensional

Loading: Pressure difference across blade normalized by tip dynamic head

Chord: Non-dimensional distance along splitter chord

List of Figures

List of Tables

1. Introduction and Motivation

1.1 Motivation

Centrifugal compressors are widely used in industry, ranging from gas pumps, aircraft propulsion, and stationary power generation. Compressors are exposed to a variety of unsteady forces that can increase stress levels in the part, and lead to premature structural failure. One significant source is the unsteady loading due to the presence of upstream and downstream bladerows. These time-varying loads can induce vibratory stresses in the blades that are significantly higher than the steady-state stresses. Material failure due to vibratory stresses is usually referred to as high-cycle fatigue, or HCF.

Current methods deal with the centrifugal compressor HCF problem by minimizing exposure to stimuli that excite the resonant frequencies of the compressor components. The condition where a modal frequency and a stimulus frequency coincide is referred to as a resonant crossing. Due to the large number of structural modes and potential stimuli, some resonant crossings are always present in an engine's operating range. The decision on which crossings remain in the operating range relies on past experience and engineering judgment. Often, this leads to unexpected difficulties during initial testing of a new or fielded engine. Engine companies can spend valuable time and money fixing an HCF problem during the engine development phase. Knowledge of the aerodynamic forcing function prior to engine test would allow a design engineer to eliminate the exposure to the most severe operating conditions prior to manufacturing the initial hardware.

Thus there is a need for a research effort to understand and predict unsteady loading on the compressor components, namely blades and vanes, and the conditions under which aeromechanical difficulties such as HCF can occur. Improved understanding of the basic design variables that control the level of unsteady loading can aid in identifying crossings of concern. By defining an adequate model for predicting the time-dependent flow field, a designer would have the essential forcing function required for forced response analysis. Prediction of the forced response level in a compressor would allow for early

identification of high stress crossings so that they can be removed from the operating range. This would lead to more robust designs and significantly reduce the risk of encountering HCF problems during the engine development phase.

1.1 Technical background

1.2.1 The centrifugal compressor

The major advantage of the centrifugal compressor over axial designs is that high pressure ratios (greater than 8:1) can be obtained in a single stage. The use of a centrifugal compressor can greatly reduce the weight, cost, and parts count when a high pressure rise is required. Centrifugal compressors are generally used in low mass flow gas turbine applications where they can obtain high efficiency and do not require an excessively large frontal area [1].

Total pressure rise is obtained in the centrifugal compressor via two specific mechanisms. First, aerodynamic diffusion in the relative frame results in a net increase in kinetic energy in the absolute frame. Second, there is a centrifugal force on the air that is a consequence of the increase in radius from inlet to outlet [2]. The centrifugal effect is the main differentiation between axial and centrifugal compressors. Centrifugal work transfer does not require relative frame diffusion, so the magnitude of the pressure rise is not limited by airfoil separation as in the axial compressor.

A centrifugal compressor consists of an impeller followed by a diffuser. Airflow enters the rotating impeller in the axial direction at station 1 and exits the impeller in the radial direction at station 2, as shown in Figure 1-1. Torque is transferred to the fluid via the rotating blades on the compressor disk. Often times, main (long) and splitter (short) blades are used. This allows for large flow area at the inlet, while maintaining adequate solidity for high slip factors at the exit.

Airflow leaves the impeller with high kinetic energy and high absolute Mach number. The diffuser is a stationary component consisting of radial passages that de-swirl and diffuse the high Mach number flow prior to entering the combustor. Often, a de-swirling bend section is used downstream of the main diffuser to turn the flow towards axial

before entering the combustor. Combustor stability requirements often require a substantial level of diffusion in the diffuser stage [2]. Aerodynamic losses in both the impeller and diffuser limit the overall pressure rise capability and adiabatic efficiency of the machine.

1.2.2 Compressor durability

Compressor durability refers to the ability of the compressor to withstand its operating loads over the required mission life of the part. Durability is a critical design constraint, as it effects the safety, operational cost, and readiness of the flight vehicle system. Two common modes of material failure in a compressor are low-cycle fatigue and high-cycle fatigue.

High cycle fatigue is a phenomenon where mechanical vibration induces significant unsteady stress levels in a part. One source of vibration is forced response, where an unsteady forcing function excites a structural mode, leading to high unsteady stress levels. Metallic materials typically have a known endurance limit, a combination of mean and alternating stress levels that the material can withstand indefinitely without experiencing material failure. Fatigue margin can be defined as the relative difference between the peak operating stresses in a part and the known endurance limit (Figure 1-2). In the limit where no vibratory stresses are present, the fatigue limit represents the ultimate strength of the material.

The blade mean stress is set by design variables such as material density, rotational speed, and gas temperature. Finite-element methods have been shown to provide reasonably adequate assessments of the mean stress. The alternating, or vibratory stress is more challenging to quantify. Vibratory stress levels are set by design variables such as the material thickness, strength of the unsteady blade loading and damping forces. Forced response analysis can be used to analytically assess the magnitude of the vibratory stresses, but an adequate representation of the forcing function is needed to obtain valid results. Partly because of this reason, current industry practice for centrifugal compressors relies on engine test measurements rather than analytic prediction [3].

1.3 Previous work

Availability of resources in high-speed computing makes three dimensional time-accurate simulations feasible for generating aerodynamic data for rotating turbomachinery. Time accurate simulations which account for the relative motion of the rotor are essential to developing an understanding of the flow phenomena which set the levels of unsteady loading in a centrifugal stage. Consideration of previous work aids in understanding the state-of-the-art and provides a starting point for this research.

Computational fluid dynamic (CFD) simulations of centrifugal compressors have been successfully used to calculate stage performance by several researchers. Srivastava and Macrorie performed a steady-state mixing plane calculation for a centrifugal stage with a GE MOD-2 type diffuser using the Tascflow code [4]. Calculated stage performance, in terms of pressure rise and efficiency, was within 1% of the experimental results from rig tests. Roberts and Steed also performed mixing plane calculations using CFX [5]. This stage had a "fish-tail" style pipe diffuser close-coupled to a tandem blade impeller. Results showed that CFD calculations for stage performance were also within 1% of the experimental results. Both calculations capture the trends of stage performance with operating conditions. Results from these steady state analyses provide confidence in the capability of CFD to make reasonable predictions of centrifugal compressor performance.

In recent years, there has been an increasing focus in using CFD to calculate time-accurate flowfields in centrifugal compressors. Shum [6] quantified the effect of impeller-diffuser interaction on centrifugal stage performance. Mainly concerned with stage performance, Shum [6] identified the impeller-diffuser gap as a controlling parameter for unsteady interaction in the stage. Strong fluctuations observed in the last 10-15% of the vane passage for a baseline design with a 9% radius ratio demonstrate the upstream influence of the diffuser static pressure disturbance. Murray [7] verified Shum's findings, and put forth a hypothesis that gap-to-pitch ratio is the controlling parameter which sets the impact of unsteadiness on compressor performance. An

unsteady simulation was undertaken by Sheng [8] on a different centrifugal compressor. He showed that a Reynolds-averaged code U2NCLE provided a reasonably adequate assessment of the performance trends near the design speed.

Unsteady blade loading and its implication on HCF has been recently researched by Caitlin Smythe [9]. Smythe [9] compared the unsteady flowfield for two similar compressor designs, one of which has known aeromechanics difficulty. Results showed that this compressor had stronger unsteady fluctuations along the blade surfaces than the baseline compressor. The use of unsteady CFD analysis for aeromechanics design was discussed by Kielb [10]. He showed that recent calculations for resonant response, including unsteady CFD, compare well with experimental measurements.

Ziegler et al performed experimental investigations of impeller-diffuser interactions in a centrifugal compressor [11]. Comparisons between two diffuser configurations showed significantly higher levels of velocity fluctuations at the impeller exit when the radius was decreased from 14% to 4%.

1.4 Selection of a research compressor

For the purpose of studying the unsteady flow field, a research centrifugal compressor is chosen. A compressor recently developed at the General Electric Company showed evidence of aeromechanics difficulty during the product development stage. Indications of HCF were found at the splitter blade leading edge. Further investigation into the problem revealed two resonant crossings in the operating range of the machine.

A Campbell diagram is commonly used to depict resonant crossings. Modal frequencies and stimulus frequencies are plotted on the vertical axis against rotor speed on the horizontal axis. The Campbell diagram for this particular machine shows the two modal frequencies crossing the diffuser passing frequency in the operating range (Figure 1-3). Follow on engine testing revealed high levels of vibratory response for the 6th modal crossing, but significantly lower levels for the 5th mode. Thus this provides a clear indication of an upstream manifestation (indication at splitter LE) of a downstream stimulus (diffuser passing frequency).

The centrifugal stage of interest consists of a backswept impeller with alternating full and partial-passage splitter blades. The stator consists of a GE Mod-2 diffuser coupled to a radial bend and a deswirl cascade (Figure 1-4). The Mod-2 diffuser is a 3-dimensional diffuser that is formed by discrete passages machined into a solid metal ring. The diffuser shape consists of several distinct sections, shown in Figure 1-5.

Investigation of the flowfield of this compressor serves to identify the conditions under which impeller-diffuser interaction action can drive high levels of vibration. Although the physical speed of the crossings occur at different values, the centrifugal compressor operating point is essentially identical for the two modes. Due to the temperature rise which occurs in the upstream axial compressor and the fact that the two compressors run at the same physical speed, the centrifugal compressor operating line remains fixed over the range of rotor corrected speeds (Figure 1-6).

Although a design fix has been developed for this machine, the basic behavior of this machine provides a valuable source of information. Analysis of the flowfield of this machine provides insight to the link between unsteady blade loading and high vibratory stress in the airfoils.

1.5 Technical objectives

Based on the observations in the research compressor, three objectives are put forward for this research project

1) Identify the physical mechanism responsible for the observed aeromechanics phenomena and quantify the level of unsteady loads acting on the splitter blade

2) Identify the design parameters that control the level of unsteady loading in a centrifugal compressor stage

3) Define an adequate model for predicting unsteady loading in a centrifugal stage

1.6 Research contributions

The specific contributions of this research are: (1) First of a kind unsteady numerical experiments have been implemented to elucidate an upstream manifestation of a downstream stimulus for a centrifugal compressor stage with a Mod-2 diffuser. (2) The controlling parameters identified are impeller-diffuser gap, stage loading (characterized by DeHaller number), and relative Mach number; the impeller-diffuser gap sets the strength of the unsteady loading, while stage loading sets the extent of the upstream manifestation of unsteady loading. (3) The results of a quasi-2D isolated impeller model in which an unsteady static pressure boundary condition is used to approximate the presence of a downstream diffuser have been shown to capture the key features of the unsteady blade loading. (4) The effect of time-averaging the unsteady inlet conditions has been eliminated as a source of over-predictions in the choked flow capacity of a fluid device.

An implied utility of the contributions are: (i) Identification of the controlling parameters as noted in (2) can provide direction in the future when there is a need to reduce the level of unsteady loading so as to avoid occurrence of aeromechanics difficulty; and (ii) the quasi-2D approximation could be used during the design phase to approximate the unsteady loading in a timeframe that is compatible with the design environment.

1.7 Thesis outline

This thesis is presented in the following manner:

Chapter 2:

Chapter two describes the overall approach used to analyze the unsteady flow fields in the centrifugal compressor. CFX is assessed and showed to be an adequate computational tool for performing the unsteady calculations.

Chapter 3:

Chapter 3 is focused on assessing the impact of unsteady flow on the choked flow capacity of a simple nozzle. The goal is to confirm whether unsteady effects play a role in the over-prediction of choked flow when steady-state approximations are used. Results from quasi-steady analysis and unsteady CFD show that there is no inherent unsteady, inviscid effect that leads to over-predictions of choked flow when steady methods are used.

Chapter 4:

Chapter 4 presents the results of quasi-2D unsteady analysis of the centrifugal stage. Four specific diffuser geometries are considered (baseline, increased throat, increased gap, increased gap and throat). The results are synthesized in order to identify the key parameters that control the level of flow unsteadiness in a centrifugal stage.

Chapter 5:

Chapter 5 presents the results from a quasi 2-D unsteady analysis of a centrifugal impeller. An unsteady pressure boundary condition is used to simulate the presence of the downstream diffuser. The goal of this analysis is to assess the hypothesis that operating conditions effect the attenuation of an unsteady disturbance. Specifically, increased mass flow and the resulting decreased diffusion leads to enhanced upstream attenuation of the unsteady pressure disturbance in the impeller passage.

Chapter 6:

Chapter 6 presents the results of the 3-D unsteady calculation of the research compressor at the design point. The peak levels and upstream extent of the unsteady load on the splitter blade is quantified. Unsteady blade loading computed from the quasi 2-D model is shown to be in accord with the unsteady blade loading computed from the full 3-D model.

Chapter 7:

Chapter 7 provides a summary of the research and provides suggestions for future work.
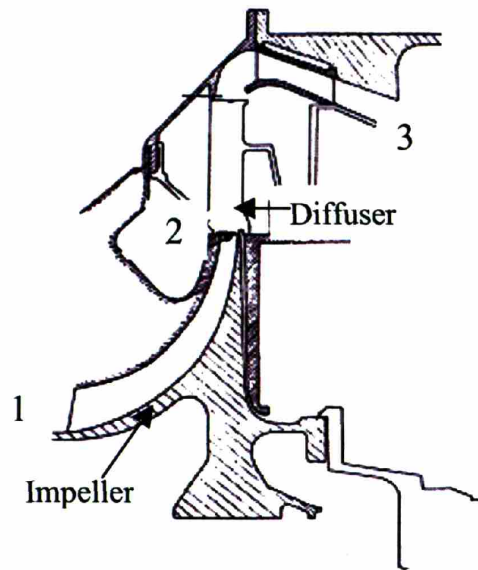
Figure 1-1 Sketch of centrifugal compressor, showing stations 1,2 and 3 which delineate the impeller inlet, impeller exit, and diffuser exit respectively
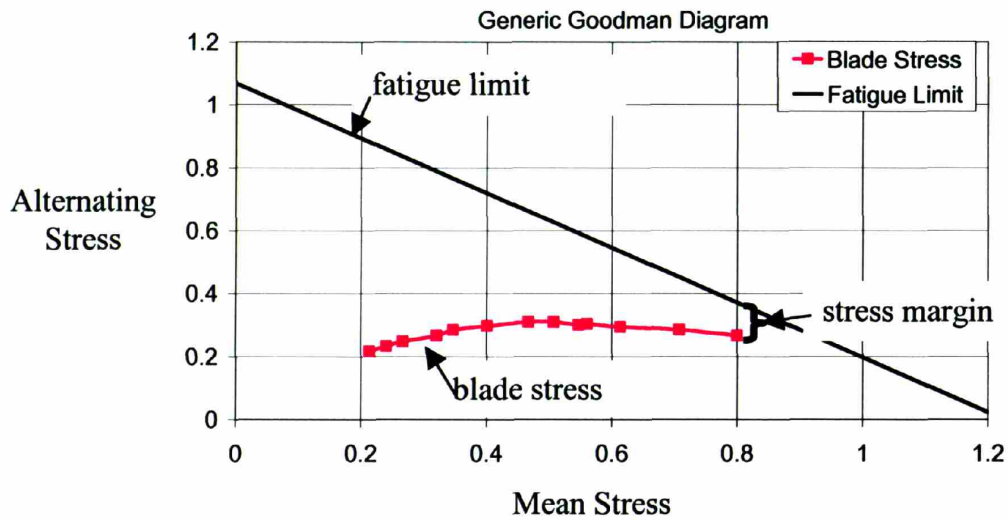
Figure 1-2 Generic goodman diagram to illustrate the definition of stress margin
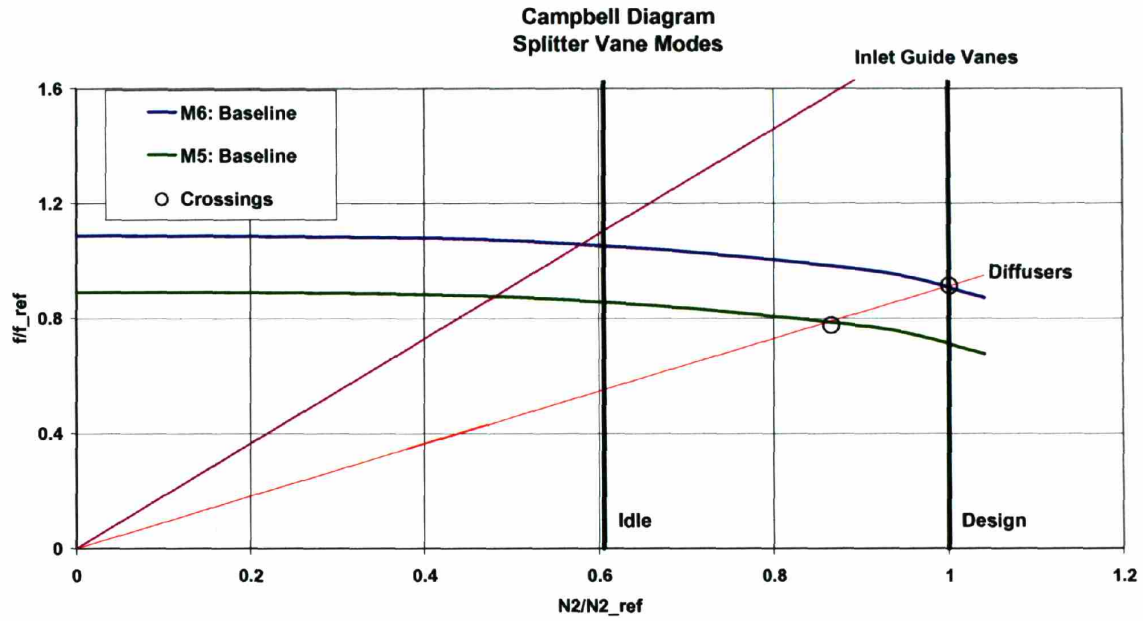
Figure 1-3 Campbell diagram for the research compressor showing the diffuser frequency crossing the 5th and 6th modal frequencies of the splitter
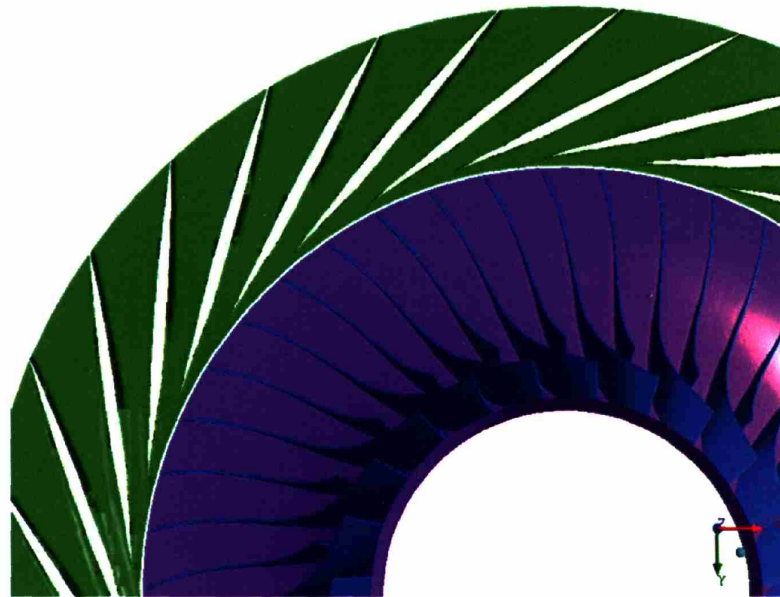
Figure 1-4 Partial view of full stage including impeller and GE MOD-2 diffuser
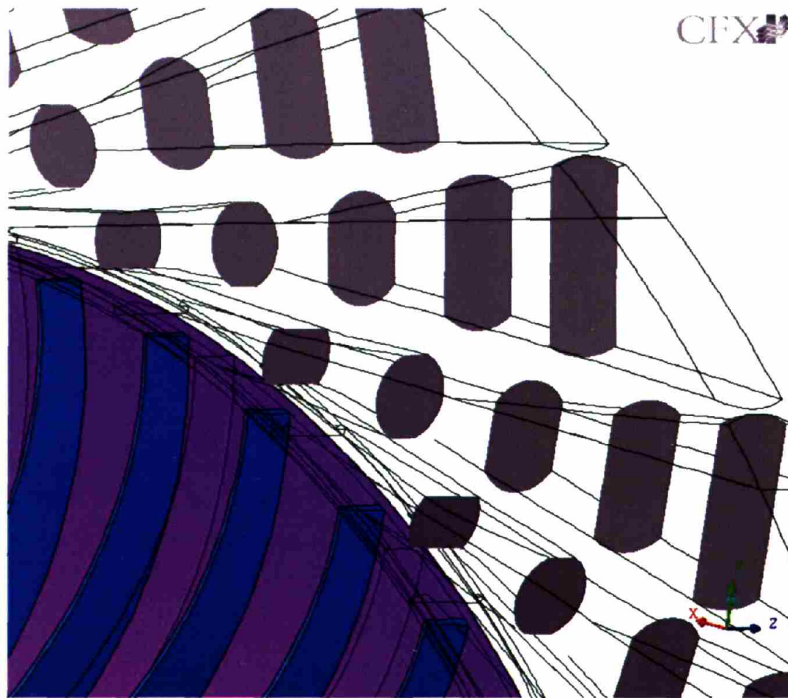
Figure 1-5 MOD-2 diffuser cross-sections which indicate the complex 3D nature of the diffuser design
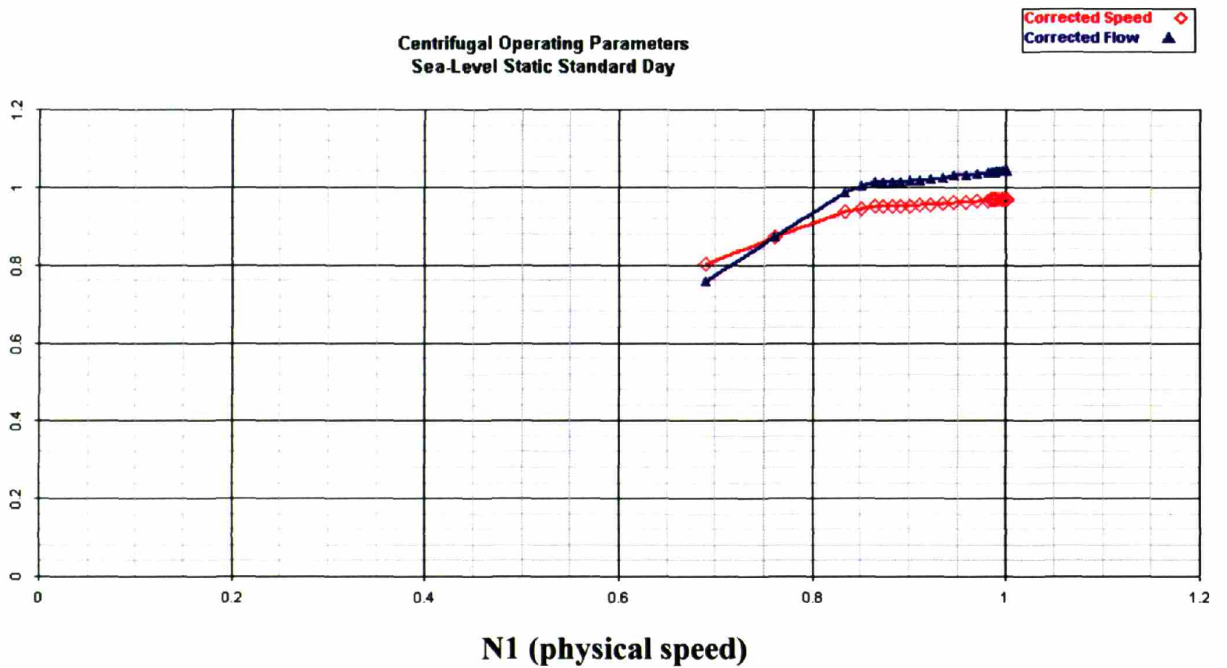
Figure 1-6 Centrifugal compressor corrected speed and flow vs. rotor speed showing small changes in operating parameters for a range of physical speeds

2. Technical Approach

2.1 Introduction

This chapter describes the methodology used in performing the numerical experiments required to address the research questions posed in chapter 1. Section 2.2 provides a description of the computational tool utilized for these experiments, and the method used to reduce the data into relevant metrics. Section 2.3 describes the specific models used for the computational experiments. Section 2.4 presents the results of code assessment studies for the models described in section 2.3. The models are first checked for numerical adequacy, and then compared with measured rig data. Results of these studies show that the selected tool is adequate for answering the research questions.

2.2 Computational Tool

2.2.1 Description of CFX code

Computational fluid dynamics (CFD) is selected as a tool to analyze the unsteady flowfield of the research compressor. The results are used to extract physical understanding and identify the specific flow process of interest. CFD can be used during the design phase to provide valuable insight in to the unsteady flow behavior prior to testing a new design

The commercial code CFX 5.7.1[1] has been used for all calculations described in this thesis. CFX is a finite-volume based flow solver that solves the set of equations for 3D unsteady compressible flow over a discretised fluid domain. The control-volume form of the 5 conservation equations (mass, momentum (3), and energy) is applied at finite volumes formulated at each node in the discretised domain. CFX uses a fully implicit coupled iterative solver that updates flow variables until all conservation equations are satisfied within a specified tolerance. Second order accuracy is obtained by a "numerical advection correction" which uses a gradient-based correction for

---

[1] CFX is a registered trademark of ANSYS, Inc.

approximating primitive variables at integration points. A second-order backwards Euler scheme is used to approximate transient terms. The use of CFX for calculating turbo machinery rotor-stator flow has been reported in a paper by Galpin, et al [12].

Turbulence is modeled using the shear-stress transport (SST) model. SST is a Reynolds-averaged turbulence modeling approach that accounts for the turbulent stresses by representing only the mean quantities in a flow field [13]. SST combines the k-ε and the k-ω turbulence models via a blending function which forces k-ω in the boundary layer and k-ε in the freestream. This method has been shown to produce acceptable and consistent results for a wide range of mesh sizes[14].

2.2.2 Computational Grid

The numerical procedure described in section 2.2.1 requires an adequate grid to represent the fluid device of interest. The grid used to model the research compressor is shown in Figure 2-1. This figure shows the grid on a section through the mid-span of the impeller and the diffuser. Structured hexahedral elements are used on the impeller, while unstructured tetrahedral elements are used on the diffuser. Generating an adequate structured grid for the diffuser proves difficult due to the complex 3D shape, so the unstructured grid has been chosen. Unstructured mesh has been shown to provide adequate results by several researchers [5,6,8]. Figure 2-2 shows a cross-section of the mesh at the diffuser throat. Note the incorporation of inflation layers near the walls in order to adequately model the shear layer in the wall region.

2.2.3   Boundary Conditions

Boundary conditions must be specified at all boundaries of the grid where specific conditions are known. Inlet boundary conditions consist of specifying the total pressure, total temperature and flow angle. These conditions are based on measurements from the

experimental rig. Physical mass flow is specified at the domain exit, except near choke conditions where static pressure is specified.

Boundary conditions must also be specified on the surfaces in the domain that represent rigid walls. In general, walls are specified as smooth, no-slip walls that are fixed in the appropriate reference frame. The one exception is wall boundaries for the quasi-2D model. In this case, the model uses a thin cut through the passage, and free-slip walls are used on lower and upper boundaries spanning between the blade surfaces.

Blades in a compressor are usually evenly spaced, thus the flow in the compressor exhibits blade-to-blade periodicity. In other words, the flow field can be represented by multiple repeated sections. One can take advantage of this fact and significantly reduce the memory requirements for a model. A periodic boundary is applied at surfaces-of-revolution that bound a single impeller passage. These boundary conditions forces flow variables to be equal at corresponding nodes.

One additional boundary condition that requires some attention is the interface between the impeller and the diffuser. In order to calculate a steady solution, an approximation is made. The CFX stage (also known as mixing plane) model is chosen to approximate the flow at the diffuser inlet. Mixing plane uses an averaging procedure to mix-out the impeller exit profile in order to develop average boundary conditions at the diffuser inlet. Density, radial velocity, tangential velocity, and static temperature are averaged across the interface in a manner that conserves mass flow, radial momentum, tangential momentum, and energy across the interface. Figure 2-3 shows circumferential distribution of radial velocity at the impeller-diffuser interface. Note that the impeller profile is mixed-out to a uniform velocity imposed on the downstream diffuser. The physical implication of mixing plane is that the static pressure influence of the diffuser is not passed into the impeller, and thus unsteady effects are not accounted for. Figure 2-4 shows the circumferential distribution of static pressure at the interface. Note that the static pressure profile at the impeller is not reflective of the downstream static pressure disturbance at the inlet to the diffuser. The mixing plane formulation is used to obtain an initial condition for unsteady calculations and to estimate the stage performance, but cannot be used to obtain the unsteady blade loading.

In order to assess the unsteady blade loading, multiple time-accurate simulations are performed. Rather than averaging flow variables across the interface, the sliding plane formulation is used at the impeller-diffuser interface. Sliding plane directly maps flow quantities across the interface using an interface grid. Relative motion between the impeller and diffuser is accounted for by updating the position of the impeller relative to the diffuser for each timestep.

Pitch differences are accounted for by scaling flow quantities across the interface. In other words, the interface grid is "stretched" or "compressed" in the circumferential direction when the impeller blade and diffuser passage counts differ. The physical implication is that the wavelength of the diffuser disturbance does not replicate the true wavelength. Therefore, all unsteady models use 3 impeller passages and 4 diffuser passages. This ratio of impeller blades and diffuser passages is assumed to closely approximate the full geometry. The geometry used for the unsteady calculation is depicted in Figure 2-5.

2.2.4 Data-Reduction Method

All post-processing is performed with CFX POST. Eight governing equations are used to solve for 8 primitive flow variables for each interior node. All derived variables, such as Mach number, total pressure, total temperature, and entropy can be calculated from the primitive variables.

ρ from Conservation of mass

U_x from Conservation of momentum (x-direction)

U_y from Conservation of momentum (y-direction)

U_z from Conservation of momentum (z-direction)

H from Conservation of energy

T_s from Constitutive equation (dH=Cp*dT)

P_s from Thermodynamic state

k   from Turbulent kinetic energy transport

ω   from Turbulent frequency transport

Compressor performance is calculated for all steady state and transient cases. For all cases where time-accurate flow simulations are used, time-averaging followed by mass-averaging is used to calculate the operating point and overall performance of the machine. Time averaging of a flow variable ϕ at a given node is given by

$$\bar{\phi} = \frac{\sum_{i=0}^{i=m} \phi_i}{\tau}$$

(eq 2.1)

where $\bar{\phi}$ is the time-averaged value, ϕ is the instantaneous value corresponding to time-instant i, m is the number of timesteps included in the time averaging, and τ is the characteristic period over which the variable is time-averaged. This period represents the time required for the splitter blade to proceed from a diffuser vane leading edge to the next, referred to as the diffuser passing period.

Mass averaging of $\bar{\phi}$ is obtained by using

$$\bar{\phi}^{ma} = \frac{\sum_{i=0}^{N} (\bar{\rho}_i \bar{\vec{V}}_i \bullet \hat{n} dA_i)\bar{\phi}_i}{\sum_{i=0}^{N} (\bar{\rho}_i \bar{\vec{V}}_i \bullet \hat{n} dA_i)}$$

(eq 2.2)

where $\bar{\phi}^{ma}$ is the averaged quantity, N is the total number of nodes on the surface of interest, $\hat{n}$ is the surface normal vector, dA_i is the area of a surface bounding the finite volume at a given node i, and $\bar{\phi}_i$ is the time-averaged flow quantity at the given node i.

6 major metrics are used to quantify machine performance at a given operating condition. Impeller pressure ratio, π_{imp}, is given by

$$\pi_{imp} = \overline{P}_{t2}^{\ ma} / \overline{P}_{t1}^{\ ma}$$

(eq 2.3)

while impeller efficiency is given by

$$\eta_{imp} = \frac{\pi_{imp}^{\frac{\gamma-1}{\gamma}} - 1}{\tau_{imp} - 1}$$

(eq 2.4)

where temperature ratio, τ_{imp}, is given by

$$\tau_{imp} = \overline{T}_{t2}^{\ ma} / \overline{T}_{t1}^{\ ma}$$

(eq 2.5)

Temperature ratio represents the amount of work needed to obtain the pressure ratio, π_{imp}. Pressure ratio and efficiency define the overall performance and are two major design parameters for a compressor.

Diffuser performance is defined by the pressure recovery and pressure loss coefficient. The goal of the diffuser is to convert the high dynamic pressure at the impeller exit into high static pressure. The recovery coefficient, C_p,

$$C_p = \frac{\overline{P}_{s3}^{\ ma} - \overline{P}_{s2}^{\ ma}}{\overline{P}_{t2}^{\ ma} - \overline{P}_{s2}^{\ ma}}$$

(eq. 2.6)

represents the fraction of the available dynamic pressure that is recovered. Pressure loss coefficient, C_{loss},

$$C_{loss} = \frac{\overline{P}_{t2}^{\ ma} - \overline{P}_{t3}^{\ ma}}{\overline{P}_{t2}^{\ ma} - \overline{P}_{s2}^{\ ma}}$$

(eq 2.7)

represents the reduction in total pressure due to irreversible processes that occur in the diffuser.

The overall performance of the stage accounts for the impeller performance and additional losses that occur in the diffuser. Stage pressure ratio, π_{stage},

$$\pi_{stage} = \overline{P_{t3}}^{ma} / \overline{P_{t1}}^{ma}$$ (eq 2.8)

represents the net pressure ratio created in the stage, including losses in the diffuser. Stage efficiency, η_{stage},

$$\eta_{stage} = \frac{\pi_{stage}^{\frac{\gamma-1}{\gamma}} - 1}{\tau_{imp} - 1}$$ (eq 2.9)

represents the ratio of ideal temperature rise for the given pressure rise to the actual temperature ratio required.

Several additional variables are calculated from the CFD results to quantify the unsteady behavior in the stage. A metric for quantifying the level of unsteadiness, P_f, is defined as

$$P_f = \frac{P_{max,\tau} - P_{min,\tau}}{.5\rho_1 U_{tip}^2}$$ (eq 2.10)

where $P_{max,\tau}$ and $P_{min,\tau}$ represent the maximum and minimum static pressure which occur during one characteristic period, respectively. P_f represents the strength of unsteadiness by comparing the peak-to-peak pressure fluctuations. The time-accurate load across the splitter blade is of utmost interest because this sets the level of peak strain, and thus has strong implications for aeromechanics response. The expression for splitter loading is given by

$$\Delta P_s = \frac{P_{PS} - P_{SS}}{.5\rho_1 U_{tip}^2} \qquad \text{(eq 2.11)}$$

where P_{ps} and P_{ss} represent the static pressure on the pressure and suction side of the splitter, respectively. This equation uses the time-accurate static pressure difference across the blade at a given streamwise location. A metric for quantifying the level of load fluctuations on the blade, ΔLs, is given by

$$\Delta L_s = \Delta P_{s\,max,\tau} - \Delta P_{s\,min,\tau} \qquad \text{(eq 2.12)}$$

where $\Delta P_{s\,max,\tau}$ and $\Delta P_{s\,min,\tau}$ represent the maximum and minimum load that occurs during 1 characteristic period, respectively.

2.3 Technical Framework

2.3.1 Structured numerical experiment

Four sets of numerical experiments (denoted as Parts I, II, III, and IV) are designed and implemented for addressing the three research questions posed in chapter 1. The results are interrogated and assessed in a manner that serves to answer the research questions.

Part I constitutes a set of steady-state mixing plane calculations of the research compressor at the design speed. The calculation is performed for a range of corrected mass flowrates from stall to choke. Part I is required for two specific reasons. First, the results of the calculations are compared with experimental rig data to provide a quantitative assessment of the code. Second, a converged steady state solution is required to provide initial conditions for the unsteady calculation.

With code assessments complete, CFX can then be used to perform unsteady calculations. Part II consists of four quasi-2D unsteady stage calculations. A thin cut

through the impeller and diffuser meanline is used to approximate the compressor geometry. Figure 2-6 shows the model. It can be seen that the geometry is representative of the research compressor. Impeller blade and diffuser vane angles are maintained. Scaling of hub and casing profiles maintain the impeller stream-wise area distribution. Impeller-diffuser gap and diffuser pitch is also maintained. This model is referred to as case A.

The quasi-2D model is chosen for unsteady analysis for several reasons. First, it includes the unsteadiness associated with the interaction of the diffuser inlet static pressure disturbance with the upstream rotating impeller. A simpler model allows for clearer interpretation of the results. Second, the computational effort is significantly reduced relative to a full 3D unsteady model. Comparison of 2D and 3D calculations are performed to determine if a 2D model is adequate for estimating the unsteady loads. This is done to confirm if the 2D approximation is acceptable for estimating the loading.

Because the 2D model includes the unsteadiness associated with the interaction of the diffuser inlet static pressure disturbance with the upstream rotating impeller, it is used to identify parameters that control the level of unsteady loading in a centrifugal compressor stage. Two parameters are chosen for study, one being the impeller-diffuser gap and the other the diffuser throat area. Thus, three additional perturbations on the baseline diffuser geometry are modeled in part II. Case B uses the baseline throat, but an impeller-diffuser gap that is twice that of the baseline (denoted as 2X gap). Case C uses the baseline gap, but a diffuser throat area that is 20% greater than that of the baseline (denoted as 1.2X throat). Case D has a 2X gap with a 60% increase in throat. The goal of case D is to investigate the combined effect of increasing these two parameters. Figure 2-7 shows the solid models for the four 2-D diffuser configurations analyzed. It shows the change in gap between case A and B and the change in throat between case A and C.

Results from part II show clear differences in unsteady loading with increased throat, but the effect of throat cannot be isolated from the effect of corrected mass flow. Therefore, part III of the study is used to isolate the effect of corrected mass flow on unsteady loading. Figure 2-8 shows the computational grid used in part III. It shows that the impeller model is identical to part II, but the diffuser geometry is removed from the

model. Presence of the diffuser is simulated via an unsteady static pressure boundary condition at the impeller exit,

$$P_s(\theta,t) = \overline{P_s} + \partial p \sin(2\pi \frac{N_d}{N_i} - \omega t) \qquad \text{(eq 2.13)}$$

where $\overline{Ps}$ is the mean static pressure (varied in order to set the mass flow), ∂p is the magnitude of the static pressure disturbance, N is the number of diffuser vanes, M is the number of impeller blades, θ is the circumferential location, and ω is the diffuser passing frequency, defined as

$$\omega = N\Omega \qquad \text{(eq 2.14)}$$

where Ω is the rotational speed of the impeller in radians/sec. The value for ∂p is selected in order to match the strength of the static pressure disturbance at the meanline as calculated by the 3D mixing plane calculation. Figure 2-9 shows the circumferential variation of static pressure. It shows how equation 2.14 results in a harmonic wave that represents the static pressure disturbance at the impeller-diffuser interface plane.

While calculations from part II and III provide useful results on unsteady loading in a centrifugal compressor, they are obtained using a simple model of the actual compressor. Thus there is a need to implement full 3D unsteady calculations at the design point and this constitutes Part IV. Interrogation of this final calculation serves several purposes. First, the unsteady time-averaged performance is compared with experimental rig data as an additional step in code assessment. Second, the unsteady loading on the impeller blade is quantified. Third, the unsteady behavior is compared to the 2D model results to determine if the 2D model is adequate for calculating unsteady loads.

Comparison of the unsteady results from parts II, III, and IV provide valuable unsteady data that is used to answer the research questions. Table 2-1 provides a summary of all of the calculations discussed in this section. For reference, several variables that characterize the operating condition are included. The mass flow shown is

the computed corrected mass flow per unit area normalized by the design point value, herein referred to as "mass flow". α_1 is the absolute frame inlet flow angle (relative to the design point), while β_1 is the impeller flow angle in the relative frame (relative to the design point).

Calculation	Part	Diffuser	Dim	$\overline{\dot{m}c_a}$	α_1	β_1
A	II	A	2D	.68	36.5	-0.5
B	II	B	2D	.65	36.5	1.7
C	II	C	2D	.78	36.5	-10.8
D	II	D	2D	.89	36.5	-24.0
5	III	N/A	2D	.69	36.5	-1.7
6	III	N/A	2D	.77	36.5	-9.5
7	III	N/A	2D	.89	36.5	-24.0
8	III	N/A	2D	.57	36.5	8.8
9	III	N/A	2D	1.00	0	0
10	IV	A (3-D)	3D	1.05	0	-1.0
11	IV	A (3-D)	3D	1.10	0	-3.0

Table 2-1 Summary of Unsteady Calculations

2.3.2 Implication of mass flow and incidence angle changes on impeller loading

Development of the quasi-2D model results in one parameter that cannot be set to the same value as the 3D model, that being the impeller inlet-to-diffuser throat area ratio. The ratio of impeller-inlet to diffuser throat is decreased by 40% in the 2D model. This is a consequence of the 3D geometry of the diffuser. Because the diffuser width increases with radius, a thin cut through the meanline results in a lower diffuser inlet area for a

given impeller inlet area. Thus the mass-flow-per-unit area at the impeller inlet is reduced to perform the 2-D calculation.

In order to maintain similar flow conditions in the impeller, the rotor inlet angle, β_1, must be maintained. Velocity components for the rotor inlet velocity vector, is shown in Figure 2-10. Velocity components denoted with solid lines represent the design point, while the dashed line represent the vector diagram for the quasi-2D model. It shows that an equivalent β_1 is achieved by adjusting the absolute frame flow angle to maintain β_1 at the lower mass flow. Rotor inlet angle β_1 can be calculated using the inverse tangent function

$$\beta_1 = \tan^{-1}(\frac{W_{\theta 1}}{C_{z1}}) \qquad \text{(eq 2.15)}$$

and an expression for $W_{\theta 1}$ in terms of known variables C_{z1}, U_1, and α_1

$$W_{\theta 1} = U_1 - U_{\theta 1} \qquad \text{(eq 2.16)}$$

Combining equations 2.15 and 2.16 results in an expression for β_1 in terms of know quantities

$$\beta_1 = \tan^{-1}(\frac{1}{\phi} - \tan \alpha_1) \qquad \text{(eq 2.17)}$$

where ϕ, referred to as the flow coefficient, is defined as

$$\phi = \frac{C_{z1}}{U_1} \qquad \text{(eq 2.18)}$$

Figure 2-11 shows the variable β_1 (normalized by the reference value) plotted against flow coefficient for two different values of α_1. This figure illustrates how absolute frame incidence angle is increased in order to maintain the design value of β_1 at a lower inlet mass flow.

The decrease in corrected mass flow also affects the rotor exit velocity vector, as shown in Figure 2-12. Assuming that the slip factor does not change, the relative frame exit angle, β_2, is identical for both cases because the rotor metal angle remains fixed. One implication of this change is that relative frame diffusion(W_2/W_1), also known as the DeHaller number, is similar for both cases. This is illustrated by considering the exit relative frame velocity,

$$W_2 = C_{z2}\cot(\beta_2)$$
(eq 2.19)

which is expressed in terms of the exit flow velocity C_{z2} and the relative frame flow angle, and the inlet frame velocity

$$W_1 = C_{z1}\sqrt{1+\frac{1}{\phi^2}-\frac{2}{\phi}\tan(\alpha_1)+\tan^2(\alpha_1)}$$
(eq 2.20)

to arrive at an expression for the DeHaller number in terms of known variables

$$Dehaller = \frac{C_{z2}\cot(\beta_2)}{C_{z1}\sqrt{1+\frac{1}{\phi^2}-\frac{2}{\phi}\tan(\alpha_1)+\tan^2(\alpha_1)}}$$
(eq 2.21)

The DeHaller number is shown in Figure 2-13. It shows that at the 2D flow coefficient of 0.6, the DeHaller number is identical to the DeHaller number of the 3D model at a flow coefficient of 1.0, which is the design point.

The reduced mass flow capacity of the 2D coupled model is due to the difficulty in maintaining the same diffuser throat to impeller inlet area ratio when using a 2D stream tube approximation. This difficulty is overcome in 2 ways. First, the absolute frame incidence angle is adjusted to obtain impeller incidence angles and stage loading similar to the 3D case. Second, in part III of the calculations, the diffuser is removed from the calculation and corrected mass flow per-unit-area can be set to the same value as the 3D design (calculation 9).

2.4 Results of Code Assessment Studies

2.4.1 Grid Refinement studies

2.4.1.1 3D steady results

Grid refinement studies for the impeller have been previously studied on this machine by Srivastva and Macrorie [4]. Three grid refinement levels have been performed, and stage performance in terms of pressure rise and efficiency has been compared. Calculated performance has been shown to be similar for the medium and the fine grids. Therefore, the medium grids for the impeller and deswirler grids are used.

Grid refinement studies are required for the diffuser grid. Table 2-2 below summarizes the diffuser performance for three levels of grid refinement. The results show that changes in grid size do not cause significant changes in diffuser performance, so the again medium grid is selected for all studies.

	Elements	Cp	Δ	ω	Δ
Coarse	340K	.834		.172	
Medium	540K	.837	+.003	.169	-.003
Fine	970K	.845	+.008	.161	-.008

Table 2-2 3D diffuser grid refinement study, where K referrers to thousands.

2.1.1.1   2D unsteady results

Similar grid refinement studies were carried out for the quasi-2D model. The unsteady calculation is performed on the baseline grid at the design point. The numerical timestep is set to 16 steps per blade pass. The calculation is performed with finer timestep sizes of 160 steps-per-pass and 320 steps-per-pass to arrive at an adequate timestep. The

calculation is then performed with the medium grid. Peak values of P_f are used to measure the initial strength of the disturbance, and upstream (20-40% chord) values are used to measure the level of decay that occurs in the impeller passage. Time-averaged efficiency is assessed to ensure that calculated performance variation is within acceptable limits.

Table 2-3 summarizes the results for all unsteady grid refinement studies. Comparison of the second and third calculations shows small differences between the 160 and 320 timesteps-per-blade pass. Midspan P_f values are with 0.10 units, and time-averaged efficiency is within 0.24 points. Based on this calculation, the numerical timestep of 160 timesteps-per-bladepass is deemed adequate for this unsteady calculation. This is consistent with timestep studies performed by Sheng [8]. The calculation is then performed with a grid that is twice as fine as the baseline grid, referred to as the medium grid. The results show midspan P_f values within 0.18 units and efficiency within 0.40 points of the baseline case with 160 timesteps-per-bladepass. Figure 2-14 shows the variable Pf along the splitter chord for the four calculations performed in this grid study. It shows that the decay of the static pressure disturbance is similar for the baseline grid (denoted as triangles) and the medium grid (denoted as an asterisk). Based on these results, the baseline impeller grid with 160 timesteps-per-period is chosen for all analyses.

Elements (impeller)	Timestep	Impeller	Diffuser	Mid		Peak		Efficiency	
				P_f	Δ	P_f	Δ	η_{imp}	Δ
38.6K	T/16	Base	Base	.14		1.49		5.73	
38.6K	T/160	Base	Base	.60	.46	1.62	.13	5.32	-.41
38.6K	T/320	Base	Base	.70	.10	1.72	.10	5.56	.24
100K	T/160	Med	Base	.78	.18	1.43	-.19	5.72	.40

Table 2-3 Results of 2D unsteady grid refinement study

2.1.1.2   3D unsteady results

Although the 3D impeller grid is shown to be adequate for steady flow, this does not imply that it would be adequate for unsteady flows. Therefore, additional unsteady grid refinement studies are performed on the impeller. Table 2-4 contains the results for the 3D study. It shows that results are similar for both the medium and fine cases. Midspan Pf values are within 0.01 units and peak Pf values are identical. Figure 2-15 shows Pf along the splitter chord (both pressure and suction surfaces), and illustrates that both the medium and fine grid result in similar decay of the static pressure disturbance. Based on this study, the medium grid is chosen for the 3D unsteady calculations.

	Elements (impeller)	Timestep	Impeller	Diffuser	Mid		Peak		Efficiency	
					Pf	Δ	Pf	Δ	η	Δ
1	660K	T/160	Base	Base	0.16		1.00		-1.09	
2	1.3M	T/160	Med	Base	0.30	.14	0.92	0.8	-1.28	-0.19
3	2.1M	T/160	Fine	Base	0.29	-.01	0.92	0.0	-1.24	0.04

Table 2-4 Results of 3D unsteady grid refinement study, where M stands for millions

2.4.2 Steady state performance trends

Having demonstrated that the computational model of the stage is adequate, the next step is to assess the calculated steady-state stage performance against experimental data obtained in a test rig. The research compressor has been tested in a rig facility at GE Aircraft Engines in Lynn, MA. A calibrated venturi has been used to measure mass flowrate, and total pressure/temperature rakes have been used to measure pressure and temperatures at the impeller inlet, impeller exit, and the deswirler exit.

Figure 2-16 and Figure 2-17 show diffuser loss coefficient and recovery coefficient, respectively. Both figures show that the results of CFX are similar to previous calculations performed in TASCFLOW. TASCFLOW is a computational tool previously used at GE Aircraft Engines for calculation centrifugal compressor

performance. TASCFLOW has been shown to provide an adequate assessment for centrifugal compressor flow, and therefore provides a baseline that can be used to assess CFX [4,12]. Both the magnitude and trend with inlet corrected flow are reproduced. CFX results for diffuser performance are in accord with previously calculated results. Both figures suggest that the CFD codes over predict the performance. The results do show that both CFD codes reproduce the performance trend as mass flow is varied.

Figure 2-18 and Figure 2-19 show stage pressure ratio and efficiency, respectively. Note that these variables have been normalized by the measured design point values. Both figures indicate that the performance trends are similar to both the TASCFLOW and measured rig data. The overall level is somewhat over-predicted by CFX, but within a reasonable range. Stage pressure ratio is approximately 3% higher at the design point, and efficiency is approximately one point higher at the design point.

Steady-state analysis of the stage indicates that of both the diffuser performance and the overall performance of the stage are approximately in line with measured values. Both the trends with corrected flow and the overall levels are in reasonable agreement. Based on this assessment, CFX is deemed adequate for capturing the relevant flow processes in the research compressor.

2.5 Summary

The technical framework for addressing the research questions posed in chapter 1 is presented in the chapter. The framework consists of designing and implementing steady and unsteady simulations of flow in an impeller-diffuser stage. A quasi-2D representation of the impeller-diffuser is used in order to achieve a significant reduction in required computational resources. Four diffuser designs with varying impeller-diffuser gap and diffuser throats are considered. In addition, an isolated impeller with an imposed downstream static pressure field is designed in order to isolate the effect of corrected mass flow. Results of several code assessment studies indicate that the selected tool is adequate for assessing the flowfield for the selected research compressor. In the following chapters, the results are to be interrogated in order to address the research

questions posed in chapter 1.
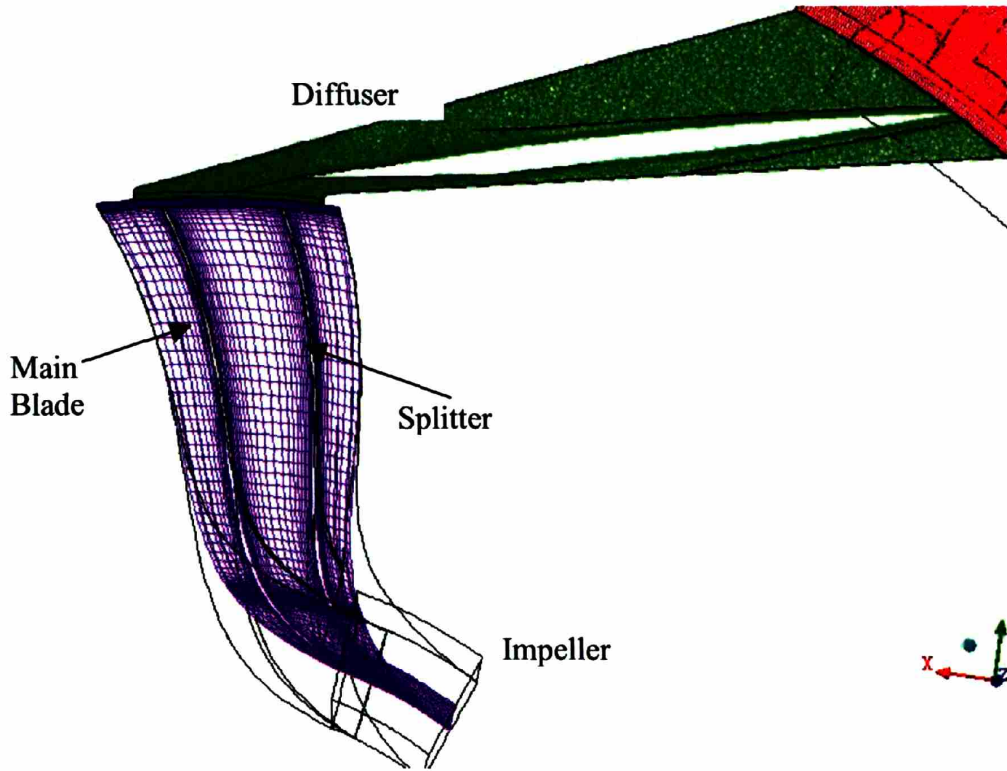
Figure 2-1 Computational grid for the research compressor which shows the structured grid used to model the impeller
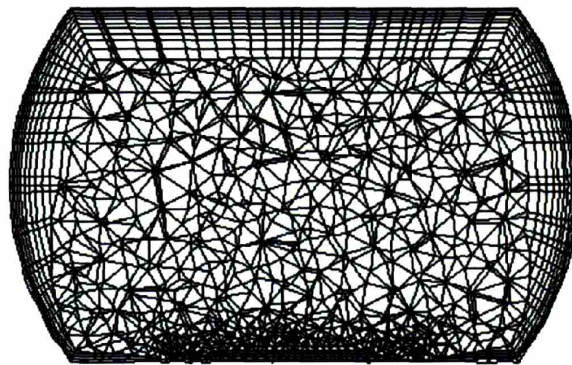
Figure 2-2 Cross-section of grid at diffuser throat which has unstructured tetrahedral elements in the passage, but utilizes inflation layers on the diffuser walls.

Impeller Interface Profiles
Radial Velocity
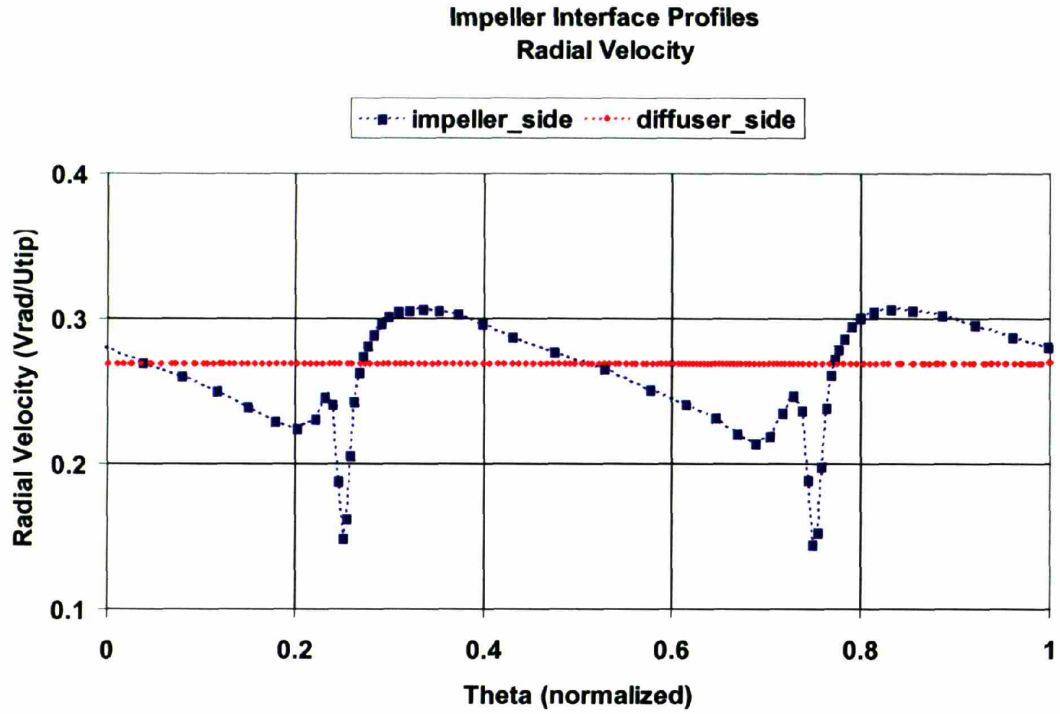
Figure 2-3 Radial velocity at impeller-diffuser interface showing the mixed-out radial velocity imposed on the downstream diffuser interface

Impeller Interface Profiles
Static Pressure
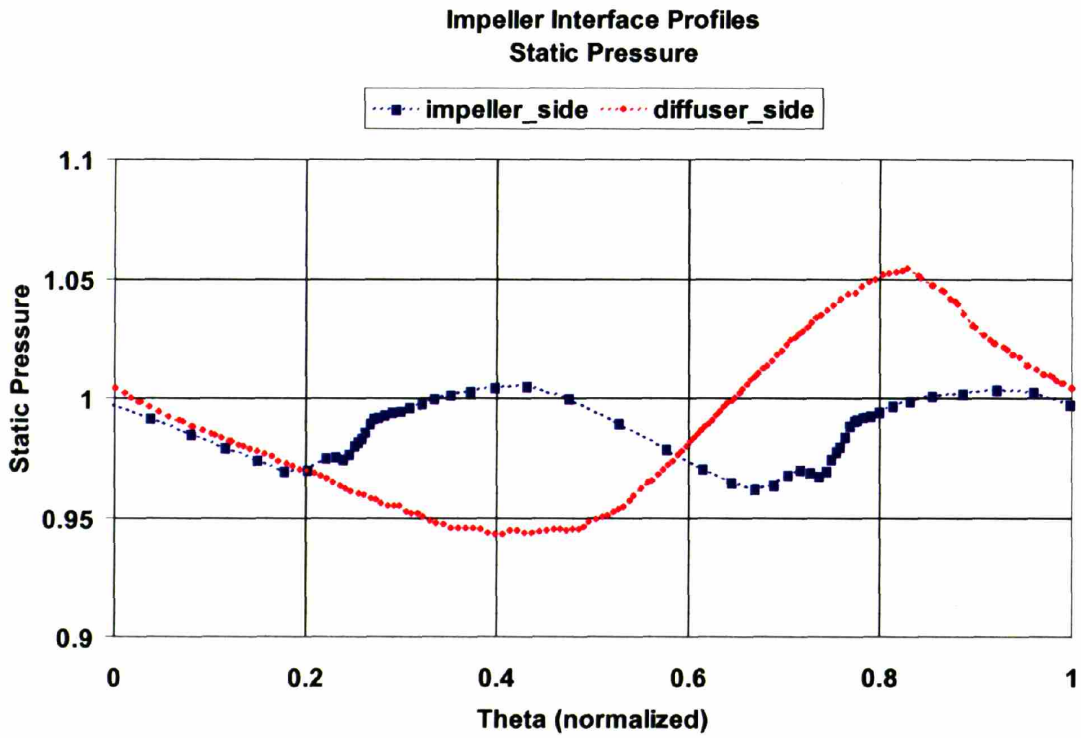
Figure 2-4 Static pressure (normalized) at impeller-diffuser interface showing that the downstream static pressure does not coincide with the upstream pressure when mixing plane is used

Figure 2-5 Domain used in 3D unsteady model which includes 3 impeller passages and 4 diffuser passages
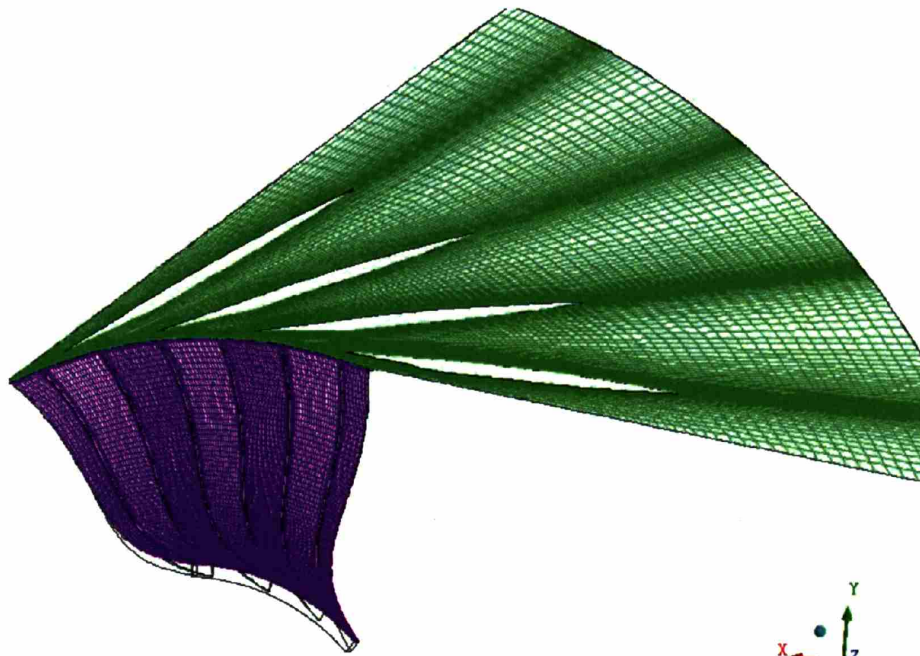
Figure 2-6 Computational grid for Part II, a quasi-2D representation of the full 3D stage

Case A

Case B

Case C

Case D
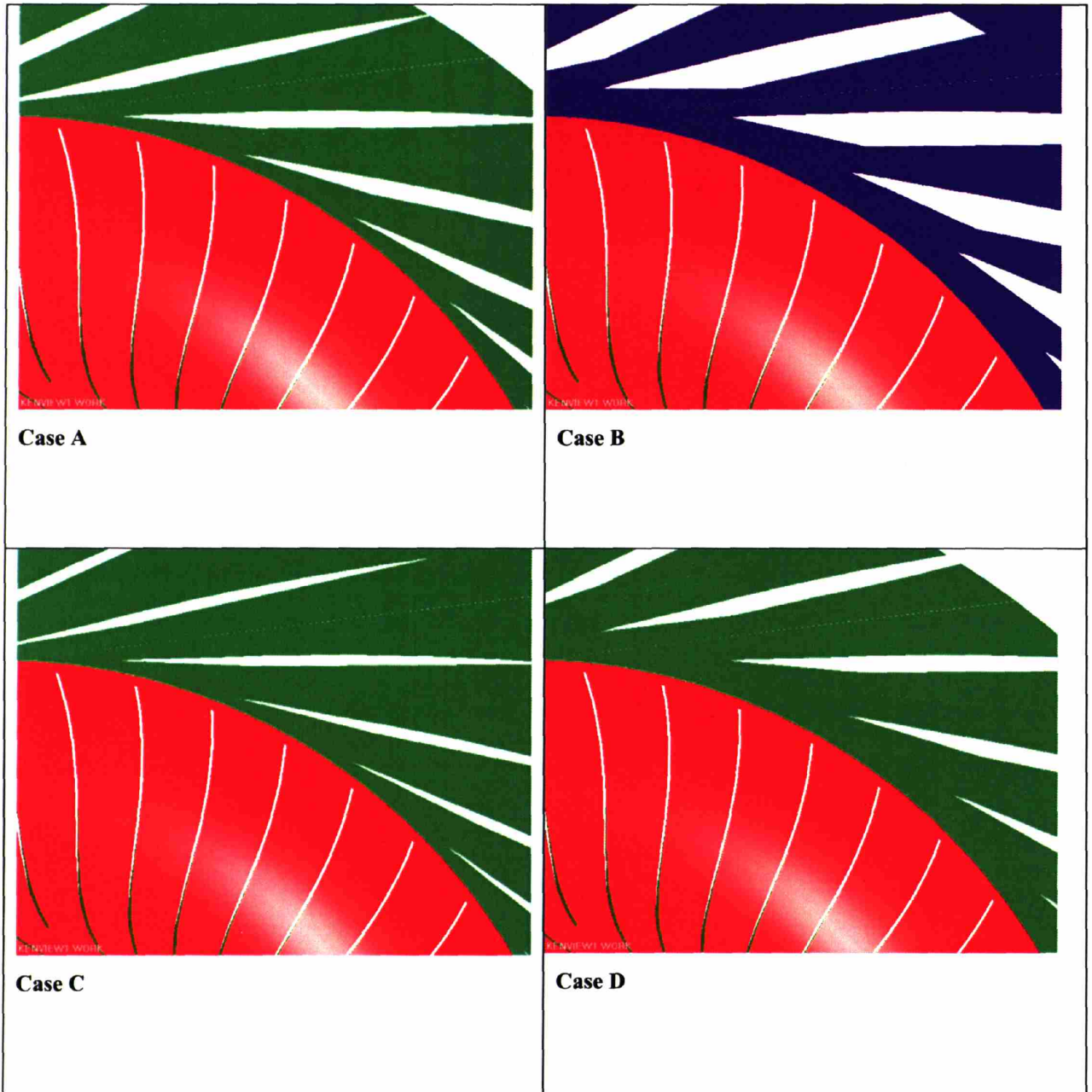
Figure 2-7 Geometry for 2D impeller-diffuser models showing the changes made to the diffuser vane in order to modify the gap and throat
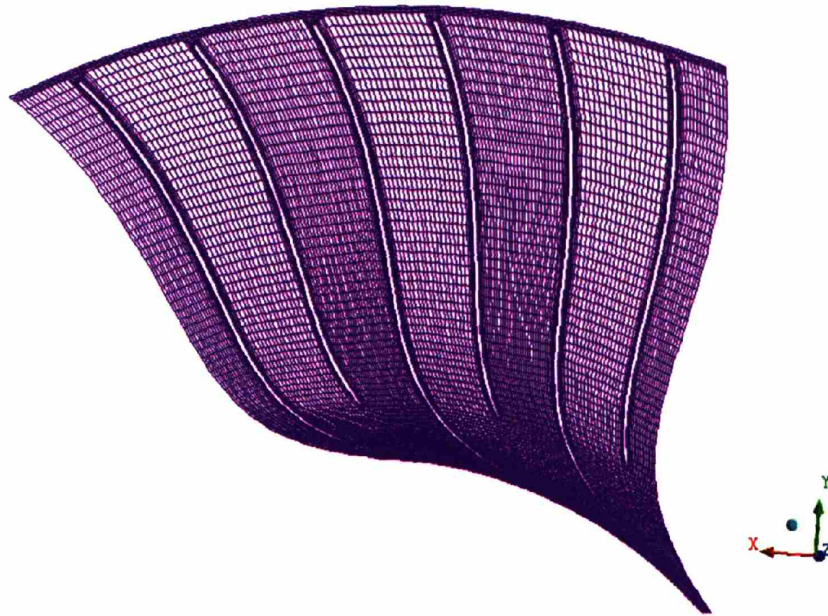
Figure 2-8 Computational grid for Part III does not use the downstream diffuser grid

Rotor-Stator Interface Pressure
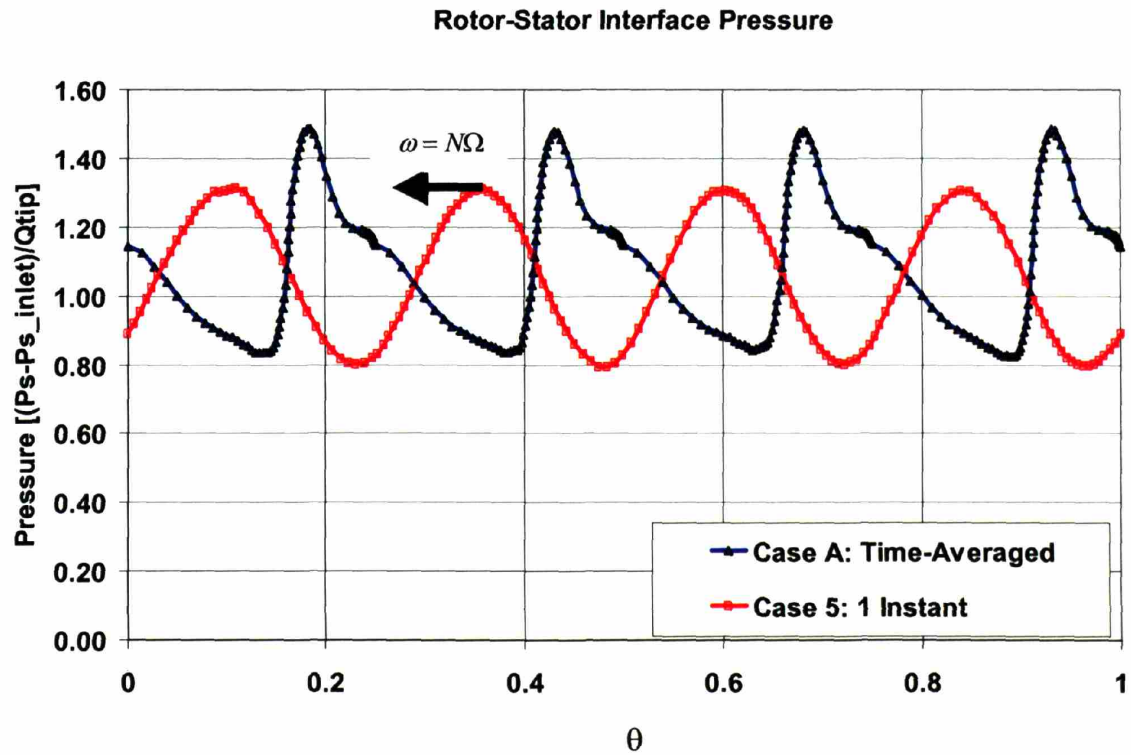
Figure 2-9 Static pressure imposed at exit plane for Part III in order to approximate the presence of the downstream diffuser.

Rotor Inlet Velocity Vector
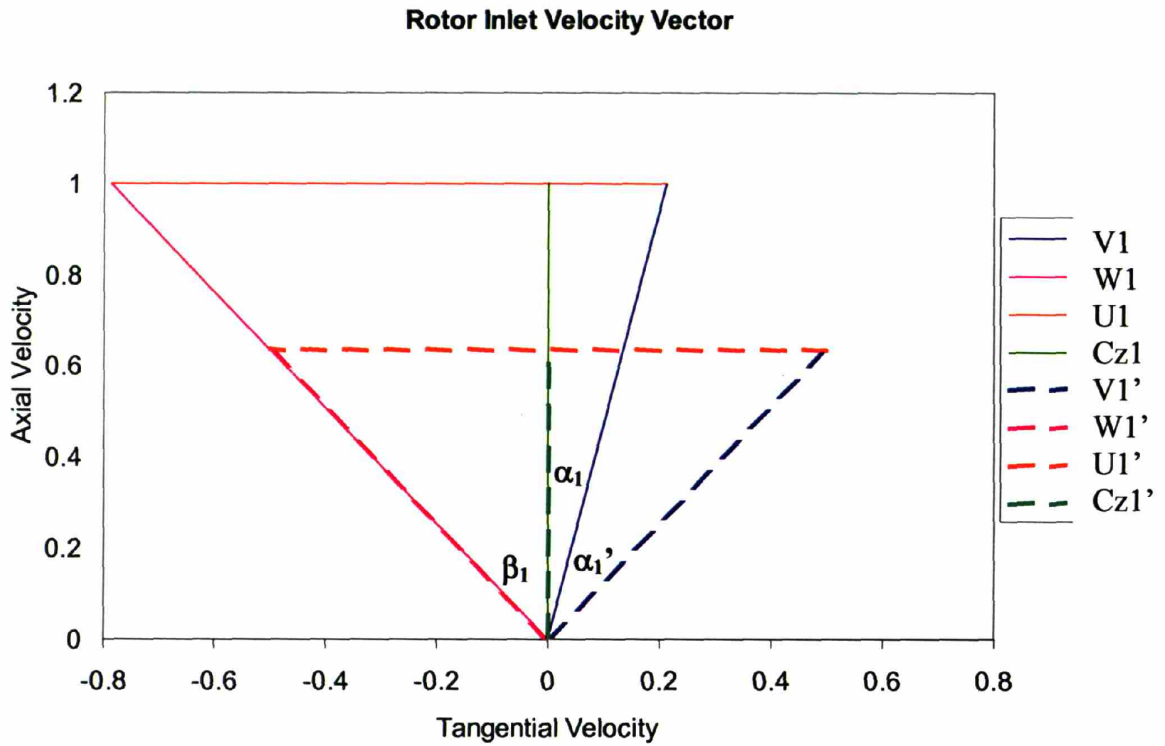
Figure 2-10 Rotor inlet vector diagram showing that β1 is held constant by increasing α1 for the quasi-2D case

Relative Frame Inlet Flow Angle
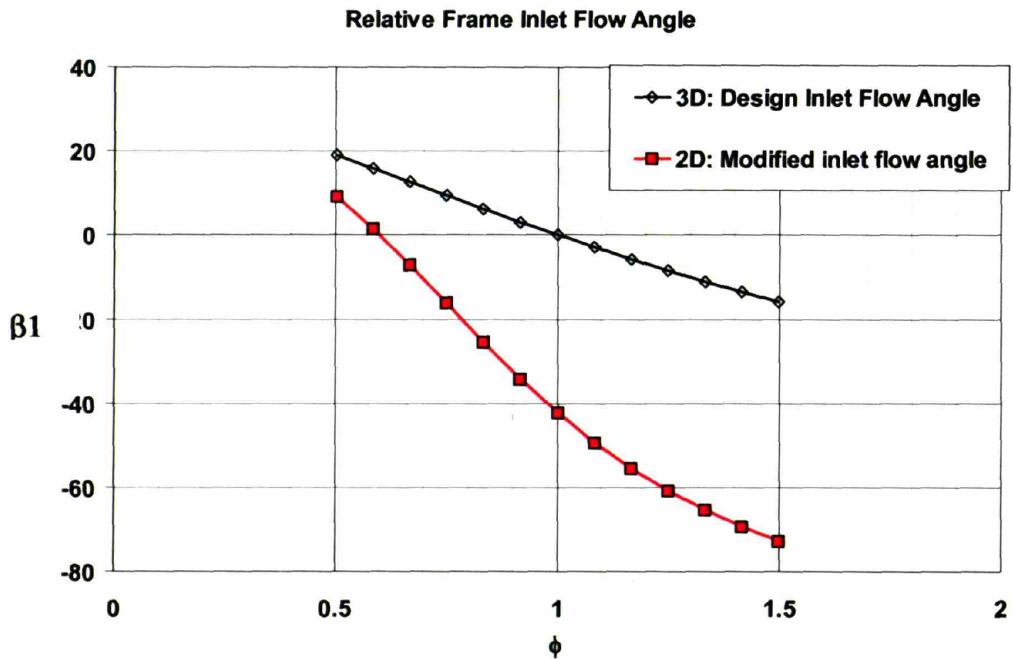
Figure 2-11 Rotor inlet flow angle as a function of flow coefficient showing that the design value of β1 is obtained in the 2D model at a flow coefficient of 0.6

Rotor Exit Velocity Vector
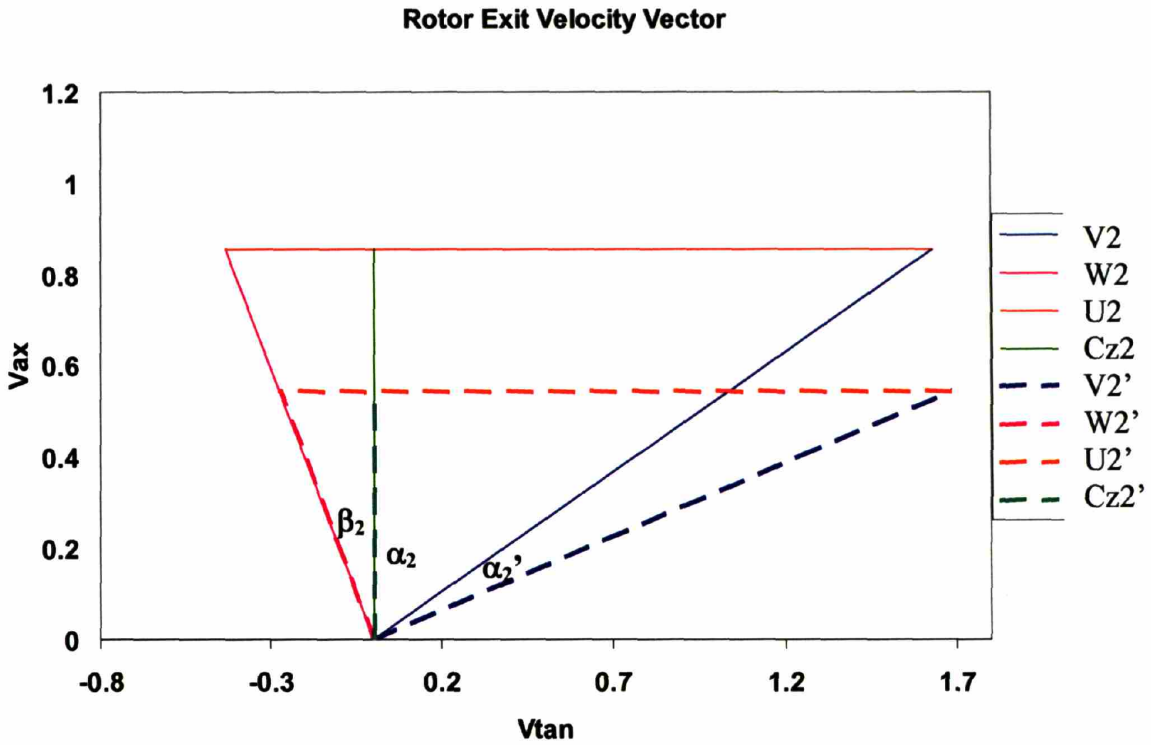
Figure 2-12 Impeller exit velocity diagram for the 3D and 2D cases.

Relative Frame Diffusion
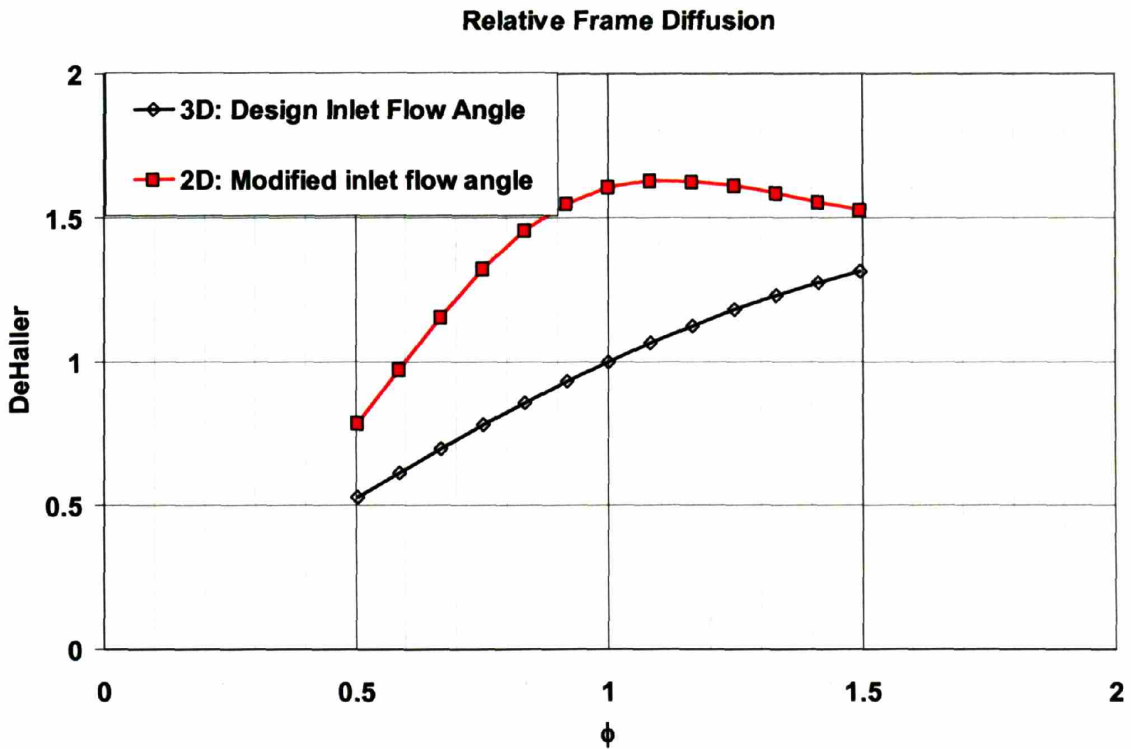
Figure 2-13 DeHaller number for cases the baseline (3D) inlet flow angle and the modified (2D) inlet flow angle showing that the design DeHaller number is maintained in the 2D model which has a flow coefficient of 0.6

51

Static Pressure Fluctuation Strength (Pf): 2D unsteady Grid Study
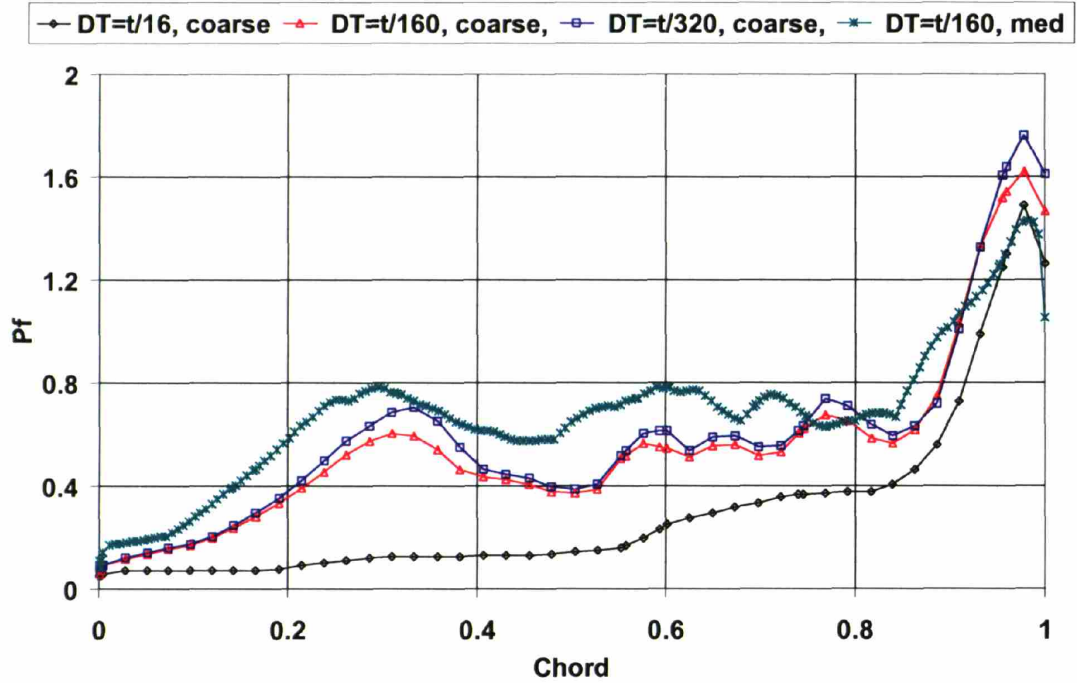
Figure 2-14 *Pf* along splitter chord for 2D grid study cases showing that the coarse and medium grid with 160 timesteps-per-pass results in similar decay of the unsteady disturbance

Static Pressure Fluctuation Strength (Pf): 3D unsteady Grid Study
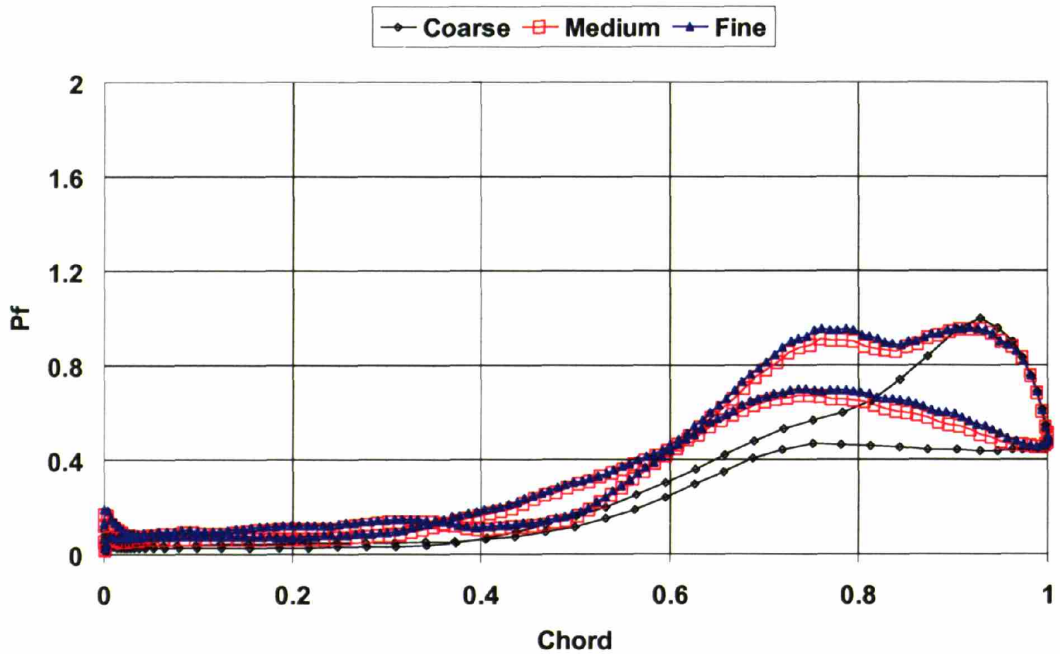
Figure 2-15 P_f along splitter chord for 3D grid study cases shows that nearly identical unsteadiness is observed for both the medium and fine grids
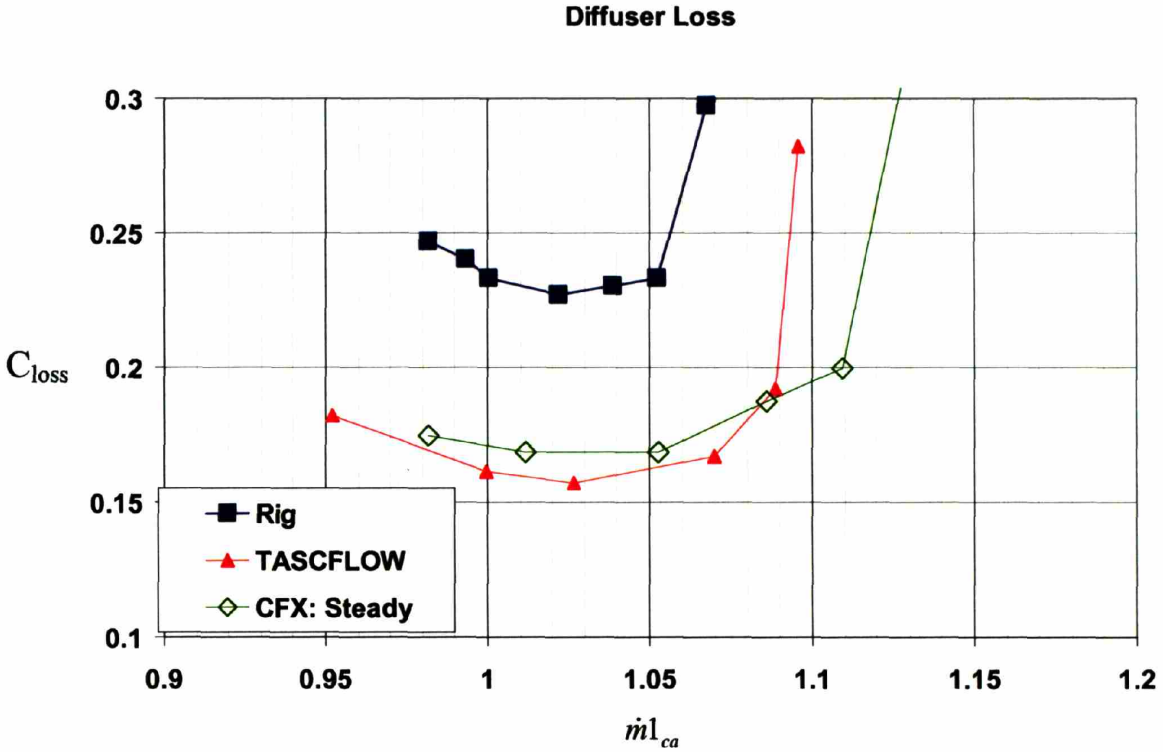
Diffuser Loss

Figure 2-16 CFX computed diffuser loss compared with experimental data and TASCFLOW computations

Diffuser Recovery
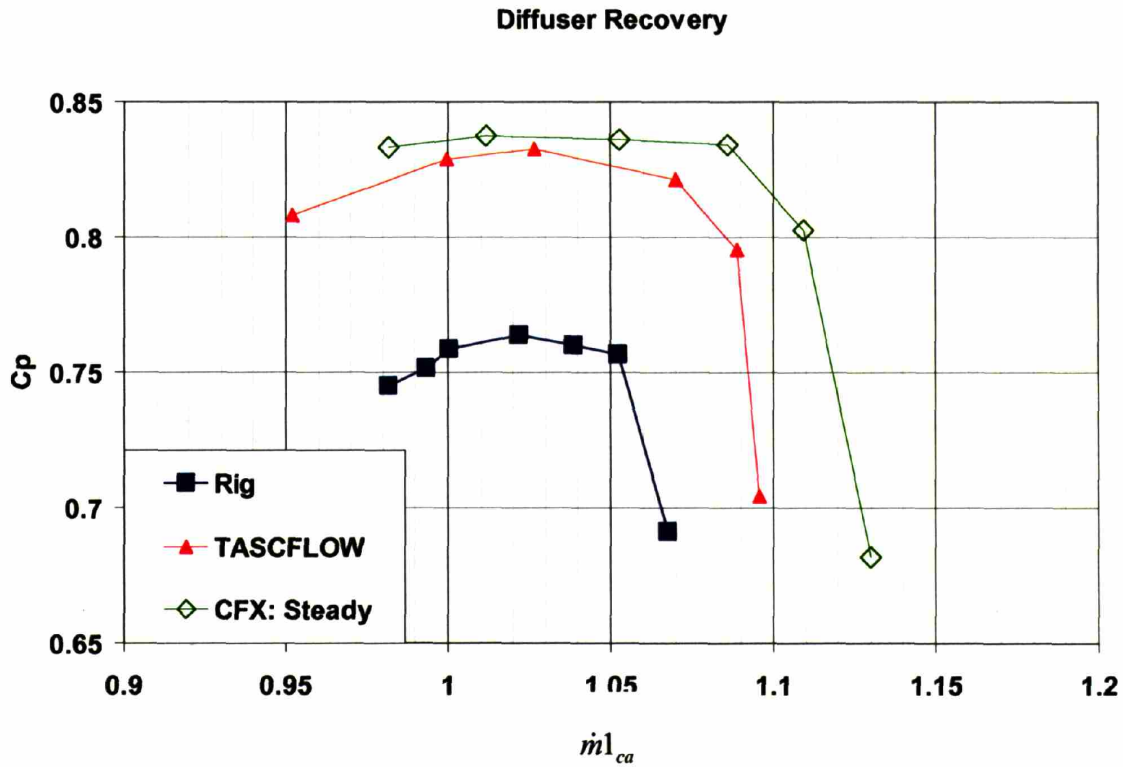
Figure 2-17 CFX computed diffuser loss compared with experimental data and TASCFLOW computations

Stage Pressure Ratio
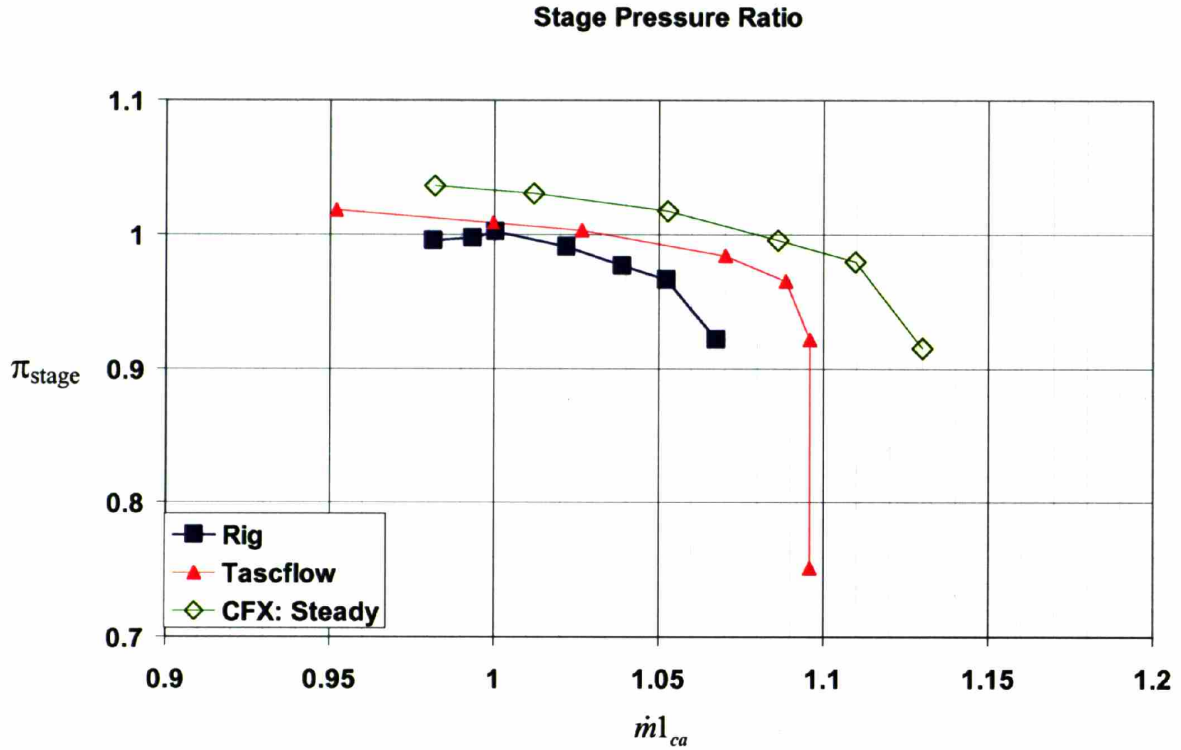
Figure 2-18 CFX computed stage pressure ratio compared with experimental data and TASCFLOW computations
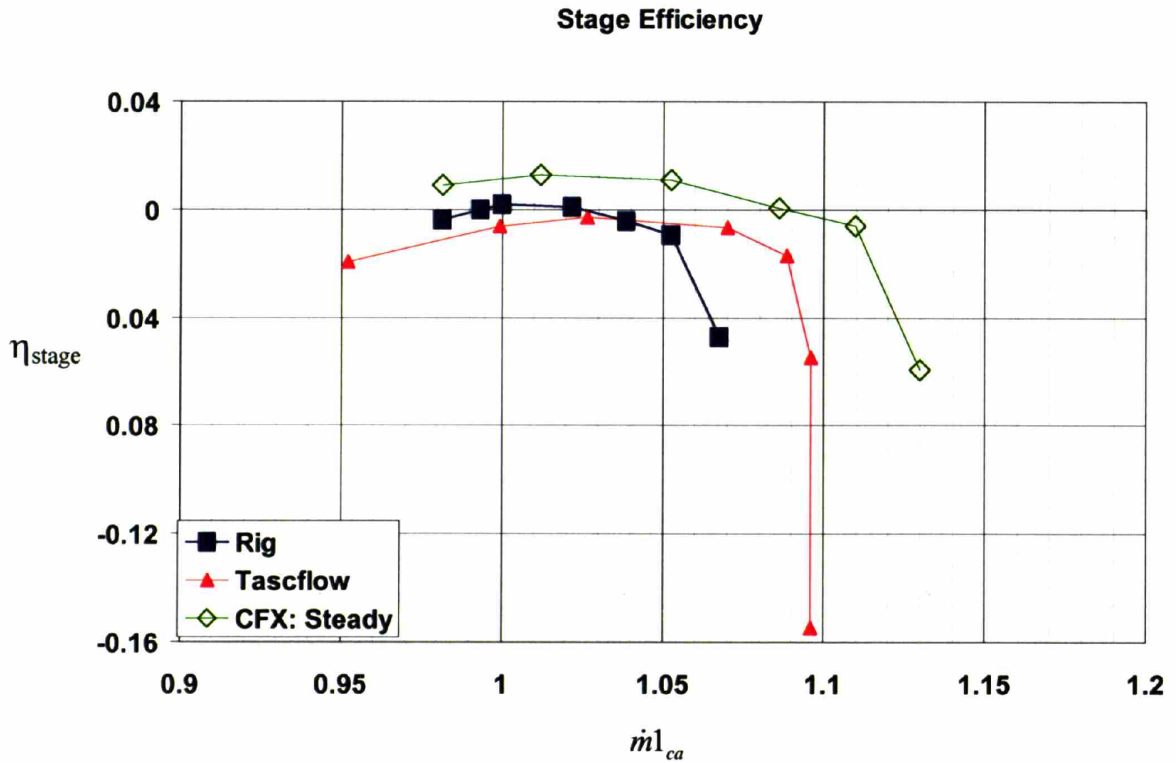
Stage Efficiency

Figure 2-19 CFX computed stage efficiency compared with experimental data and TASCFLOW computations

3. Effect of unsteadiness on time-averaged mass flow

3.1 Introduction and Motivation

Code assessment studies presented in Chapter 2 indicate that a steady-state CFD model of the research compressor provides an adequate prediction of performance at the design point. However, the CFD results over-predict the total flow capacity of the machine by 6%. Previous research efforts have yielded similar results. Srivastava and Roberts have presented results for 2 different centrifugal compressors, and both indicate over predictions in the range of 1-3%. There appears to be a trend where steady state CFD methods currently being used over-predict the maximum flow capacity of compressors.

Compressor flow capacity has a strong effect on aircraft engine performance. Thrust, horsepower and fuel burn are determined by a thermodynamic cycle calculation, which requires accurate representation of the compressor operating characteristic. An over-prediction in compressor flow leads to over-predictions in thrust, power and fuel burn. There is an increasing focus on utilizing analytic predictions during the design phase to reduce cost and improve the probability of meeting thrust and fuel burn requirements on the initial build of new engine design. Thus, there is a need to develop computational models that accurately predict the performance and the operating range of a compressor.

All of the observed over-predictions are from steady-state models. These models require a technique to average flow quantities across the interface between the rotor and stator. In reality the downstream stator sees fluctuating values of flow variables, specifically total pressure and total temperature. Viscous effects in the rotating blade row create a momentum defect, which is seen as an unsteady disturbance in the downstream stator. The effect of averaging this disturbance on the calculated mass flow capacity is not currently known.

3.2 Problem statement

The goal of this chapter is to identify if averaging of the stator inlet conditions is a root cause for over-predicting the level of maximum flow capacity for a centrifugal compressor. In order to assess whether this is the cause, a simple model problem is proposed. This model problem consists of a simple 2-D nozzle with specified inlet total conditions that exhausts to a large plenum. It is representative of the diffuser throat, which is the downstream restriction that sets the flow capacity of a centrifugal machine.

The first step in understanding the problem is to develop an expression for the flow capacity a fluid device such as a nozzle. Mass flow rate through a given area, A, is given by

$$\dot{m} = \rho V A \qquad \text{(eq 3.1)}$$

where V denotes the velocity and ρ denotes the density. Use of the thermodynamic equation of state

$$P_s = \rho R T_s \qquad \text{(eq. 3.2)}$$

allows one to express $\dot{m}$ in terms of static temperature and static pressure as

$$\dot{m} = \frac{P_s}{R T_s} V A \qquad \text{(eq 3.3)}$$

Using the definition of Mach number

$$M = \frac{V}{a_0} \qquad \text{(eq 3.4)}$$

and the expression for the speed of sound

$$a_0 = \sqrt{\gamma R T_s}$$

(eq 3.5)

in equation 3.3 leads to

$$\dot{m} = \frac{P_s}{\sqrt{\gamma T_s}} \sqrt{\frac{\gamma}{R}} M A$$

(eq 3.6)

It is more useful to express mass flow in terms of stagnation quantities because stagnation quantities at the inlet of the downstream restriction are generally known. This can be achieved by employing the isentropic relationship for temperature and pressure [15]

$$\frac{T_t}{T_s} = (1 + \frac{\gamma - 1}{2} M^2)$$

(eq 3.7)

$$\frac{P_t}{P_s} = (1 + \frac{\gamma - 1}{2} M^2)^{\frac{\gamma}{\gamma - 1}}$$

(eq 3.8)

to arrive at

$$\dot{m} = \frac{P_t}{\sqrt{T_t}} \sqrt{\frac{\gamma}{R}} M (1 + \frac{\gamma - 1}{2} M^2)^{-\frac{\gamma + 1}{2(\gamma - 1)}} A$$

(eq 3.9)

However, the flow capacity of a fluid device is measured in terms of the maximum corrected mass flow per unit area, commonly referred to as the flow function. The flow function follows from rearranging equation 3.9 to arrive at

$$\frac{\dot{m}\sqrt{T_t}}{P_t A} = \sqrt{\frac{\gamma}{R}} M (1 + \frac{\gamma - 1}{2} M^2)^{-\frac{\gamma+1}{2(\gamma-1)}}$$

(eq 3.10)

Flow function is plotted against Mach number in Figure 3-1. The most important observation in this figure is that the flow function reaches a maximum at Mach number M=1 [15]. For a simple converging nozzle, the maximum Mach number cannot exceed one, so the flow function is fixed above pressure ratios beyond critical.

As previously mentioned, the momentum defect from the upstream rotor is the main source unsteadiness at the stator inlet. This disturbance is periodic in time. Thus there is a timescale associated with this disturbance that is related to the rotational speed and the number of blades in the upstream row. The radian frequency, ω, is defined by

$$\omega = N\Omega$$

(eq 3.11)

where N is the number of upstream blades and Ω is the rotational speed of the rotor. Thus the "flow-change" timescale, τ, is proportional to $1/\omega$. The convection time through the nozzle is of order L/U, where L is the convective length scale and U is a reference convective velocity. The ratio of the convective timescale to the perturbation timescale is referred to as reduced frequency, β.

The significance of the reduced frequency can be deduced by scaling the 1-D momentum equation.

$$\frac{\partial u}{\partial t} + u\frac{\partial u}{\partial x} = -\frac{1}{\rho}\frac{\partial P}{\partial x}$$

(eq 3.12)

The order of unsteady term, $\dfrac{\partial u}{\partial t}$, is estimated from

$$\frac{\partial u}{\partial t} \alpha \ \omega U$$

(eq 3.13)

and the convective term, $u\dfrac{\partial u}{\partial x}$, is estimated from

$$u\frac{\partial u}{\partial x} \; \alpha \; \frac{U^2}{L}$$ (eq 3.14)

Thus the reduced frequency, which is the ratio of the unsteady term to the convective term, reduces to.

$$\beta = \frac{\omega L}{U}$$ (eq. 3.15)

For cases where $\beta \ll 1$, the unsteady term can be ignored and the flow treated as quasi-steady.

Consider a quasi-steady inlet total pressure at the inlet of a convergent nozzle that exhausts to constant static pressure. The time-varying total pressure can be considered to be a square-wave type, where pressure is above the mean level for ½ of a period and below the mean level for the second ½ period, as shown in Figure 3-2. High and low points A and B on indicate the corrected mass flow level for each point in time. Steady-state analysis would consider the time-averaged inlet total pressure level and calculate a steady state corrected mass flow. This value is shown as point C.

A simple analysis is used to assess any potential difference incurred by averaging the inlet total pressure over time. Because the flow is quasi-steady, time-averaged corrected mass flow per unit area is calculated using equation 3.10 and taking the arithmetic mean between the two flow levels during each time interval. This value is indicated by point D. A non-linear flow-pressure ratio relationship results in an over-prediction of corrected mass flow when a time-average total pressure is used in the steady calculation. This simple example serves to provide a plausible explanation for the observed difference in corrected mass flow shown in .

3.3 Technical Approach

3.3.1   1-D Quasi-steady Analysis

A quasi-steady analysis is chosen to quantify the effect of averaging inlet total pressure disturbances on computed mass flow capacity. Figure 3-4 is a sketch of the nozzle geometry. The geometry has an area ratio of 2:1 and an L/D_{exit} of 4. The flow is assumed to be quasi-steady, inviscid, and adiabatic. Thus, even though inlet flow quantities is fluctuating in time, the total pressure and total temperature can be considered constant throughout the nozzle at any instant in time. Therefore, flow calculations can be performed by considering flow conditions at the exit plane only. The goal is to quantify differences in mass flow between a quasi-steady case with an inlet total pressure disturbance and the mass flow calculated based on the time-averaged inlet total pressure.

Equations 3.8 and 3.10 govern the Mach number and corrected mass flow at the exit of the nozzle. Inspection of these two equations results in five unknown variables (γ and R are assumed to be known, and the analysis will consider flow-per-unit-area). These 5 unknown variables are P_t, T_t, P_s, $\dot{m}$, and M. P_t, T_t, and P_s are chosen as independent variables and must be specified in order to perform the analysis. Ambient pressure and total temperature are specified as 1 atm and 300 K respectively, while total pressure is taken to be

$$P_t(t) = \overline{P_t} + \frac{1}{2} K\overline{q} \sin(\frac{2\pi t}{\tau})$$

(eq 3.16)

where $\overline{P_t}$ is the time-averaged inlet total pressure, K is the peak-to-peak total pressure (per unit dynamic head), and $\overline{q}$ is the time-averaged dynamic head at the nozzle exit. Thus P_t at the inlet varies harmonically in time with period τ. The time-averaged total pressure, $\overline{P_t}$, is taken to be

$$\overline{P_t} = P_{se} * NPR$$

(eq 3.17)

where P_{se} is the exit static pressure and NPR is the time-averaged nozzle pressure ratio.

The constant K is used to specify "peak-to-peak fluctuation per unit dynamic head" because the source of total pressure fluctuations in the momentum defect flow from upstream components. Dynamic head sets the difference in total pressure between the flow in the jet and the flow in the wake. Therefore, it is appropriate to scale the intensity by the dynamic head for this analysis. The time-averaged dynamic head at the nozzle exit is taken to be

$$\overline{q} = \frac{1}{2}\gamma \overline{M}^2 P_{se} \qquad \text{(eq 3.18)}$$

where the time-averaged exit Mach number is defined by

$$\overline{M} = \max(1, \sqrt{(NPR^{\frac{\gamma-1}{\gamma}} - 1)\frac{2}{\gamma - 1}}) \qquad \text{(eq 3.19)}$$

Specification of the three independent variables P_t, T_t, and P_{se} result in two equations and two dependent variables; Mach number, M, and corrected flow per unit area, $\dot{m}_a$. Equations 3.8 and 3.10 can now be re-written as

$$M(t) = \max(1, \sqrt{(P_t(t)^{\frac{\gamma-1}{\gamma}} - 1)\frac{2}{\gamma - 1}}) \qquad \text{(eq. 3.20)}$$

$$\dot{m}_a(t) = \frac{P_t(t)}{T_t}\sqrt{\frac{\gamma}{R}}M(t)(1 + \frac{\gamma-1}{2}M(t)^2)^{-\frac{\gamma+1}{2(\gamma-1)}} \qquad \text{(eq 3.21)}$$

to solve for Mach number and flow-per-unit area as a function of time.

The final step in the analysis is to calculate the flow-per-unit area from the time-mean pressure ratio, $\overline{\dot{m}}_{a,TAP}$,

$$\overline{\dot{m}}_{a,TAP} = \frac{NPR * P_{se}}{T_t} \sqrt{\frac{\gamma}{R}} \overline{M} (1 + \frac{\gamma-1}{2} \overline{M}^2)^{-\frac{\gamma+1}{2(\gamma-1)}} \qquad \text{(eq. 3.22)}$$

and compare with the time-averaged flow per unit area based on the quasi-steady inlet total pressure fluctuation, $\overline{\dot{m}}_a$,

$$\overline{\dot{m}}_a = \frac{\sum_{i=0}^{i=n} \dot{m}_a(t)}{n} \qquad \text{(eq. 3.23)}$$

where n is the total number of time-steps used in the calculation.

The difference between corrected mass flow based on the time-averaged inlet total pressure and the time-averaged corrected mass flow, Δm_a, is defined as

$$\Delta m_a = (\frac{\overline{\dot{m}}_{a,TAP} - \overline{\dot{m}}_a}{\overline{\dot{m}}_a}) X 100\% \qquad \text{(eq 3.24)}$$

3.3.2 2-D Unsteady Computational Analysis

Time-accurate CFD is used to extend the analysis performed in the previous section to cases where reduced frequency is greater than 0.1 and the flow cannot be considered quasi-steady. CFX is implemented to solve the governing equations as described in chapter 2. The computational grid for the analysis is shown in Figure 3-5. An 80x40 two-dimensional structured grid is used for the nozzle. The nozzle exit is connected to a downstream plenum in order to simulate the downstream condition for a choked or unchoked nozzle. A total number of 5340 elements are used.

The boundary conditions for the nozzle are straightforward. The static pressure at the exit of the plenum is set to standard reference conditions (P_s=1.0 atm), and total pressure and temperature are specified at the inlet. Total temperature is set constant for all simulations, and equal to standard reference temperature (T_{t1}=300.0 K). The nozzle

and plenum walls are treated as free-slip boundaries that force surface velocity to be parallel to the wall.

As in equation 3.16, inlet total pressure is specified via an equation that contains both the time-averaged and fluctuating terms.

$$P_{t1} = NPR * P_{se} + \frac{1}{2} K\bar{q} \sin(\beta \frac{U_{ref}}{L_{ref}} t)$$ (eq 3.25)

where the reduced frequency, β, is introduced as an independent variable. The reference length is the axial length of the nozzle which is set as 0.017 m and the reference velocity

$$U_{ref} = \overline{M} * a_0$$ (eq 3.26)

is based on the time-averaged exit Mach number and the speed of sound at the nozzle exit, which is calculated from

$$a_0 = \sqrt{\frac{\gamma R T_t}{1 + \frac{\gamma - 1}{2} \overline{M}^2}}$$ (eq 3.27)

Time-accurate simulations are performed using 100 timesteps per oscillation period T, given by.

$$T = \frac{2\pi L_{ref}}{\beta U_{ref}}$$ (eq 3.28)

This time-step size was proven to be adequate for this study by performing a time-step refinement study. Convergence is achieved when the maximum residual for each

governing equation is below 1E-3 and the inlet and exit mass flow achieve periodic behavior. Typically, this requires running 2000 timesteps.

The adequacy of CFX is assessed by reproducing a flow-pressure ratio relationship in accord with the known basic relationship. The assessment is show in Figure 3-6. It demonstrates that the CFX code indeed reproduces the expected trend.

In what follows, results from these unsteady simulations are discussed and presented in order to elucidate the time-averaged effect of unsteadiness on flow capacity.

3.4 Results

3.4.1   1-D Quasi-steady analysis

Figure 3-7 shows the results of the quasi-steady analysis. Time-average inlet total pressure ratio is varied between 1.1 through 2.5. Three levels of K are chosen to obtain peak-to-peak inlet fluctuations of 27%, 54%, and 110% of the time-averaged exit dynamic head. Figure 3-7 reveals two important features of the unsteady flow problem. First, large differences in corrected flow are incurred at the lowest pressure ratio. This can be explained by considering the second derivative of corrected flow with respect to pressure ratio. The second derivative of flow with respect to pressure ratio curve sets the level of difference incurred when using time-averaged inlet total pressure to calculate mass flow. Consider first the case where the relationship between flow and pressure ratio is linear (2nd derivative is zero). When the total pressure increases above the mean value, corrected flow will increase linearly. This positive increase in flow relative to the mean value is exactly offset by the decrease in flow relative to the mean value when total pressure drops below the mean level. Now consider the flow vs. pressure ratio curve shown in Figure 3-3. Because the first derivative of flow with respect to pressure ratio decreases with increasing pressure ratio (a negative second derivative), the increase in flow relative to the mean level is of lower magnitude than the decrease in flow relative to the mean level. This results in a net decrease in mass flow relative to the mean level.

Figure 3-8 demonstrates that the magnitude of the second derivative of corrected flow vs. pressure ratio is stronger at lower pressure ratios, and the sign of this value is

negative. Therefore, the steady approximation based on the time-averaged inlet total pressure will result in an over-prediction of flow, and yield stronger differences atlower pressure ratios. The interrogation of this second derivative explains the observed trends.

A second observation is that there is no difference incurred in the maximum (choked) flow level due to the steady approximation. This can be explained by a similar argument. At pressure ratios at or above choke, flow is constant and therefore first and second derivatives of flow with respect to pressure ratio are zero. In other words, when the lowest pressure ratio in the total pressure disturbance exceeds the critical pressure ratio (1.89 for a perfect gas with γ=1.4), calculated values of corrected flow are identical at all time instances and there are no differences incurred. The two important observations are summarized below:

1) Use of a time-averaged pressure ratio can lead to over-predictions in mass flow for pressure ratios below that for choked flow

2) No error in choked mass flow capacity is incurred by using a time-averaged total pressure ratio.

3.4.2 Unsteady CFD analysis

Unsteady computations are performed at three different mean nozzle pressure ratios and three different values of the reduced frequency, β. Nozzle pressure ratio levels of 1.1, 1.6, and 2.2 are chosen. These levels represent cases of low Mach number flow, high subsonic Mach number flow, and choked flow (sonic at throat). Mach numbers for the steady case are shown in Figure 3-9, Figure 3-10 and Figure 3-11 to demonstrate the 3 different flow regimes of the 3 cases. Reduced frequency values of 0.1, 1.0, and 10.0 are selected, corresponding to situations where unsteady effects are negligible, unsteady and steady effects are of equal importance, and where unsteady effects dominate respectively. All cases are calculated with K equal to 110% of dynamic head so that fluctuations are strong and differences can be observed.

Figure 3-12 and Figure 3-13 show the inlet total pressure boundary condition and inlet mass flow for the case where NPR=1.1. For the low-frequency case, inlet total pressure and inlet mass flow are in-phase, leading to the steady state over prediction in mass flow. For the higher frequency cases, there is a marked difference in phase and a reduction in magnitude. By comparing peaks of the mass flow function, it is clear that mass flow fluctuations are lagging the total pressure fluctuations.

Figure 3-14 and Figure 3-15 show the magnitude and phase relationship based on a 1D incompressible nozzle compared with the CFD results [16]. The results for magnitude and phase are in good agreement at low reduced frequency. At a reduced frequency of 1, the magnitude and phase change as calculated by the CFD results is much stronger than that which has been predicted by the 1D model. At a reduced frequency of 10, the magnitude is in agreement, but the phase is somewhat over predicted. One potential explanation for the difference is that the analytic model is based on incompressible flow. The CFD model has an average Mach number of 0.3, but the requirement for incompressible unsteady flow is that $(\beta M)^2$ is much less than one. This condition is not satisfied for the cases where reduced frequency is 1 or greater.

Quantitative results of the difference, Δm_a, for the unsteady computations are delineated in Table 3-1 below. At low reduced frequency, there is measurable difference when comparing the mass flow based on the steady calculation to the time-averaged mass flow of the unsteady calculation. For the case with mean pressure ratio at 1.1, there is a 1.8% difference incurred with the steady state assumption. For many applications, a 1.8% over-prediction in flow could have a significant impact on the final design.

	$\beta=.1$	$\beta=1.0$	$\beta=10.0$
NPR=1.1	1.8%	0.5%	0.0%
NPR=1.6	1.4%	0.4%	0.1%
NPR=2.2	0.0%	-0.4%	-0.8%

Table 3-1 Error in mass-flow-per-unit-area between

Figure 3-16 shows the CFD results plotted against the result from the quasi-steady analysis. For the low reduced frequency cases (β=.1), there is good agreement between the 1D analysis and the unsteady CFD. This provides confirmation of the conclusions stated in section 3.3. Most importantly there is no error in the mass flow capacity of the device for the quasi-steady case.

Comparison of the higher frequency situation yields a different behavior than the low-frequency case. Figure 3-16 shows for the low pressure ratio case (low Mach number), the difference is reduced at higher frequencies. The difference is reduced because the level of velocity fluctuations are lower at high frequencies, as seen in Figure 3-14.

Results for the high pressure ratio case show a negative difference, indicating that the steady approximation under predicts the choked flow. Wennerstrom has observed this phenomenon in previous research [17], where actual mass flow through a transonic compressor has been observed to be 6% higher than that predicted by steady-state codes.

This phenomenon can be addressed by considering a disturbance description of the velocity and density at the exit of the nozzle.

$$u = \bar{u} + u'$$

(eq 3.29)

$$\rho = \bar{\rho} + \rho'$$

(eq 3.30)

Time-averaged mass-flow-per-unit-area can be calculated by averaging the product of velocity and density,

$$\bar{m} = \overline{\bar{u}\bar{\rho}} + \overline{u'\rho'}$$

(eq 3.31)

where products of mean and fluctuating terms are zero because the time-average value of the fluctuating terms are zero by definition.

The time-average of the product of the fluctuating terms are not necessarily zero. Figure 3-17 contains a time-accurate plot of the term

$$\frac{\overline{u'\rho'}}{\overline{\overline{u}\rho}}$$
<div align="right">(eq 3.32)</div>

which represents the fraction of the time-averaged mass flow due to the product of the velocity and density perturbations. The figure clearly shows that at higher frequencies the product of the fluctuation terms are larger in magnitude. Time-averaged values are shown with solid horizontal lines, again showing a significant increase in this time-averaged unsteady mass flow term for higher frequencies (.75 % for β=10).

The physical explanation for the increase in mass flow with increasing frequency is the phase change in velocity that occurs when frequency changes. Figure 3-18 shows the normalized density and velocity fluctuations for the case where β=.1 and NPR=2.2. The figure shows because of the phase difference, the product of velocity and density fluctuates between and positive and negative, and the net time-average value is small.

Figure 3-19 contains normalized density and velocity for the case where β=10 and NPR=2.2. High reduced frequency reduces the phase difference and results in a product that is almost always positive. In this case, the time-average mass flow is higher than the low frequency case.

The results of the unsteady analysis provide insight into the research question. Differences in mass flow for low Mach number flows are dominated by the strong non-linearity in the mass flow to pressure ratio relationship. This leads to an over-prediction in mass flow for low reduced frequency, low Mach number situations when steady-state methods are used. As reduced frequency increases, the magnitude of velocity fluctuations are reduced and the error due to the steady approximation decreases.

Differences in mass flow for high Mach number flows are dominated by the product of density and velocity perturbations. This mechanism is not present in low Mach number flows because density fluctuations are small. The error incurred at low reduced frequency is small for high Mach number flows because density and velocity fluctuations are out-of-phase. Increasing reduced frequency causes a phase shift that leads to an overall increase in the time-averaged mass flow through the stage. This leads to an under-prediction in mass flow for high reduced frequency, high Mach number situations when steady-state methods are used.

3.5 Summary and Conclusions

Analysis and computations of unsteady flow in a convergent nozzle are presented in order to determine the whether time-averaging of the diffuser inlet conditions is a root cause for the over-prediction of the maximum flow capacity of the compressor stage. The key results obtained from these analyses are as follows:

- Time averaging of low reduced frequency ($\beta \ll 1$) inlet conditions for the purpose of steady calculations does not lead to differences in mass flow capacity (choked flow) relative to a time-accurate calculation.

- Time-averaging of low reduced frequency ($\beta \ll 1$) inlet conditions for low Mach number flows can lead to over-predictions in mass flow relative to a time-accurate calculation.

- Time-averaging of high-frequency inlet conditions for high Mach number (choked) flows can lead to under-predictions in mass flow relative to a time-accurate calculation.

The implications of these results are as follows:

- Time averaging of the inlet conditions is eliminated as a potential explanation for the over-prediction in flow capacity in observed in chapter 2.

- The effect of time-averaged inlet conditions should be considered when performing steady calculations for low Mach number, low reduced frequency flows.

Corrected Flow/Area vs. Mach Number
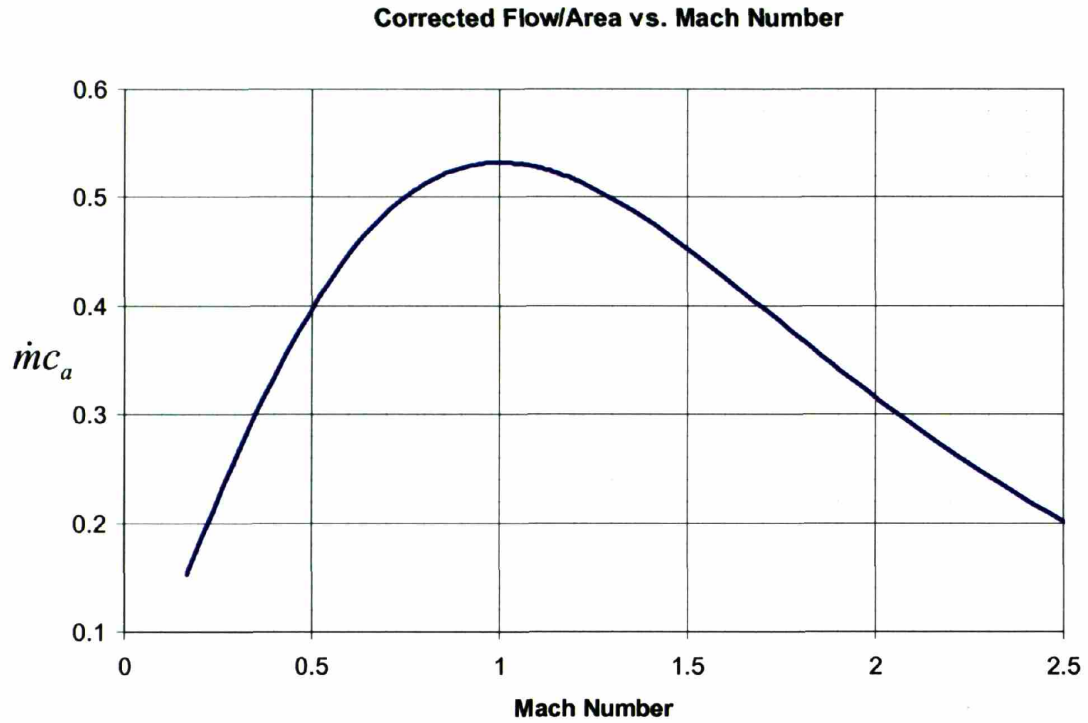
Figure 3-1 Corrected flow per unit area plotted against Mach number showing a peak value of approximately 0.54 at a Mach number of 1

Inlet Total Pressure Perterbation
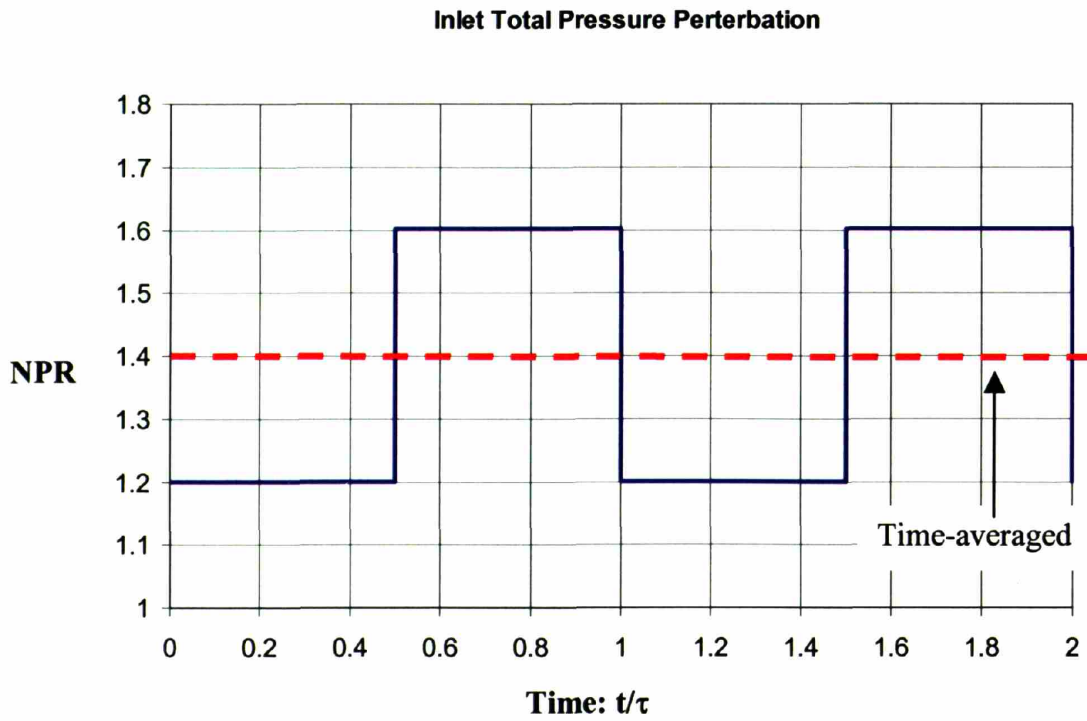
Figure 3-2 Sample inlet total pressure disturbance showing differences between unsteady and time-averaged nozzle pressure ratio (NPR)

Corrected Flow/Area vs. NPR
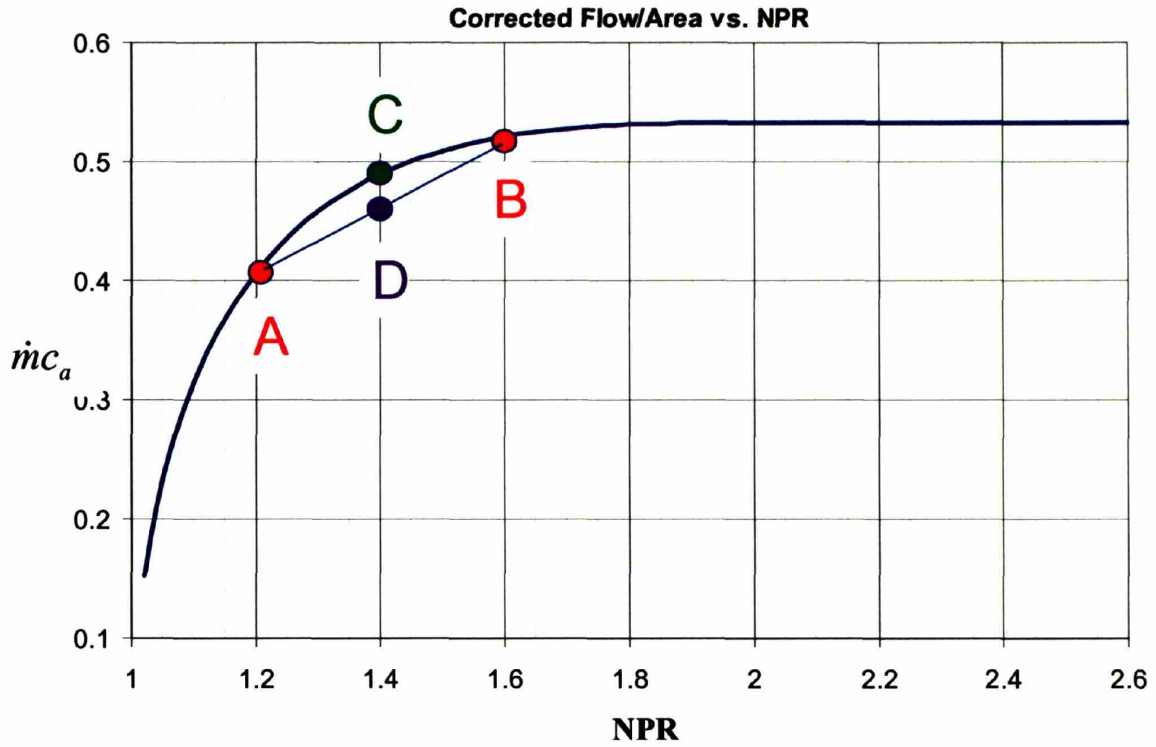
Figure 3-3Corrected flow-per-unit area plotted against NPR (nozzle pressure ratio). Case C indicates the flow based on the time-averaged NPR, while D indicated the time-averaged flow for a quasi-steady disturbance
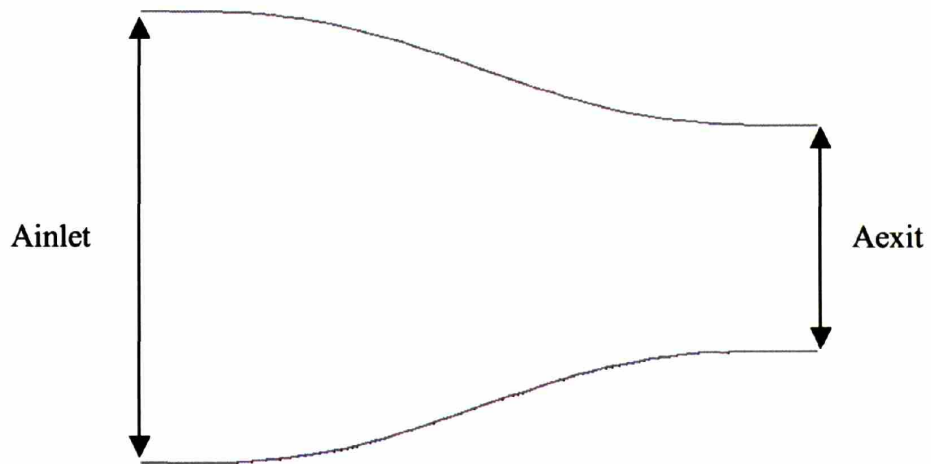
Figure 3-4 Sketch of the simple nozzle used for the quasi-steady analysis
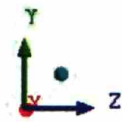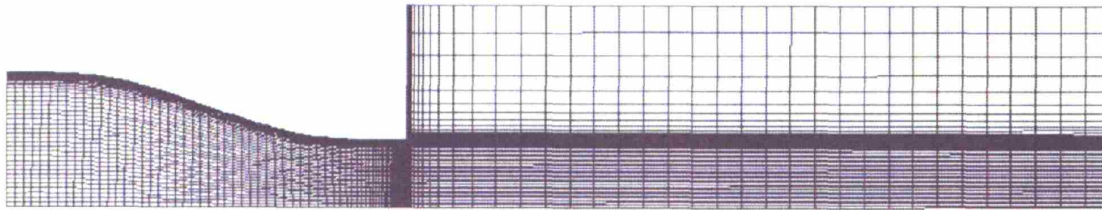
Figure 3-5 Computational grid used for the unsteady CFD computations
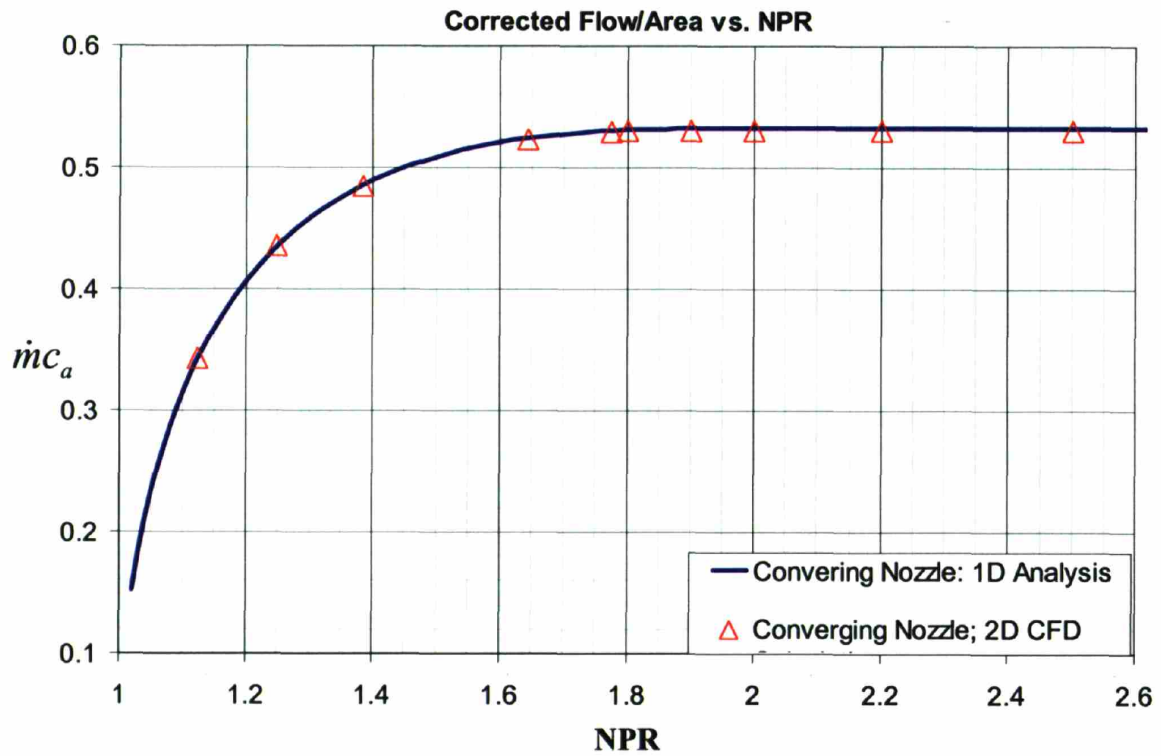
Figure 3-6 CFX computed corrected flow against NPR, compared with a 1D analysis
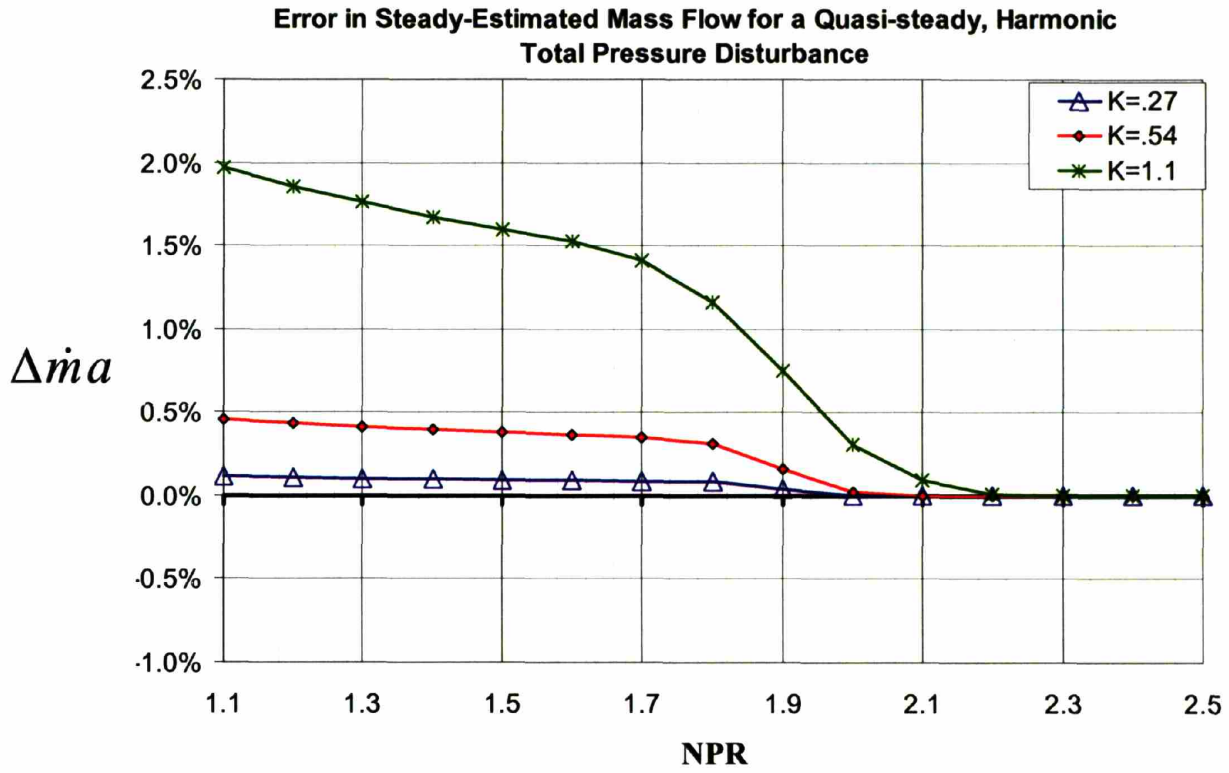
Figure 3-7 Error in steady-estimated mass flow as predicted by the quasi-steady analysis, showing large difference are incurred at low pressure ratios
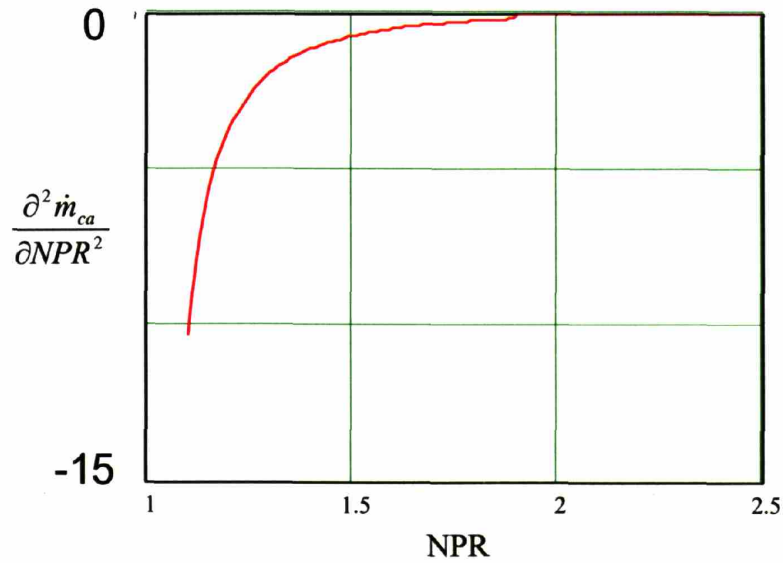
Figure 3-8 Second derivative of corrected flow with respect to nozzle pressure ratio
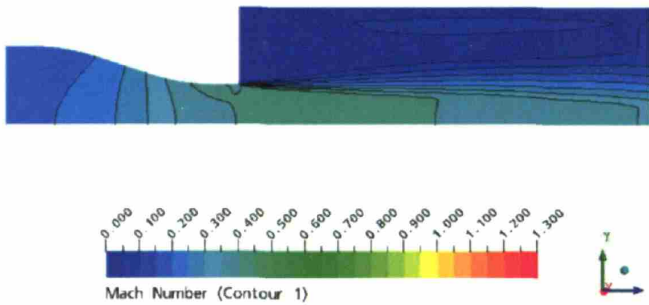
Figure 3-9 Mach Number Distribution: Pr=1.1 showing approximately incompressible flow
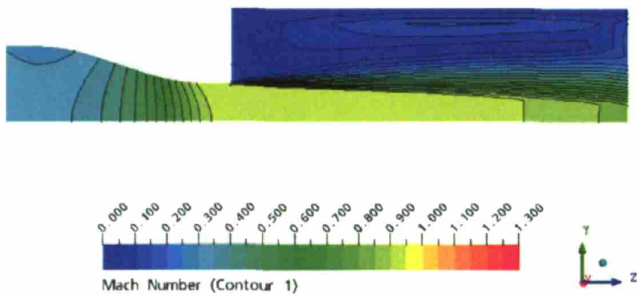
Figure 3-10 Mach number Distribution: Pr=1.6 showing high Mach number subsonic flow
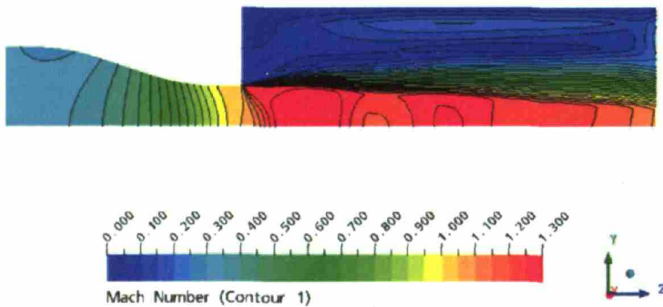
Figure 3-11 Mach number distribution: Pr=2.2 showing the choked conditions at the nozzle exit

Inlet Total Pressure: Pr=1.1 Case

☐ B=.1 △ B=1 • B=10
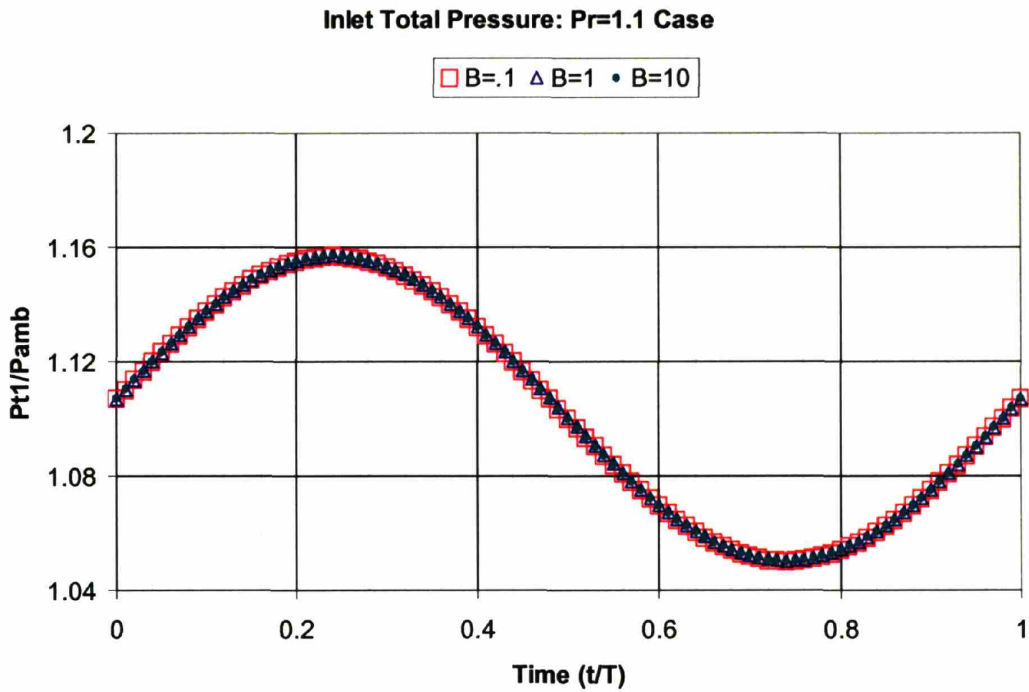
Figure 3-12 Inlet total pressure boundary conditions for the NPR=1.1 cases

Inlet Mass Flow per Unit Area: Pr=1.1 Case

☐ B=.1 △ B=1 • B=10
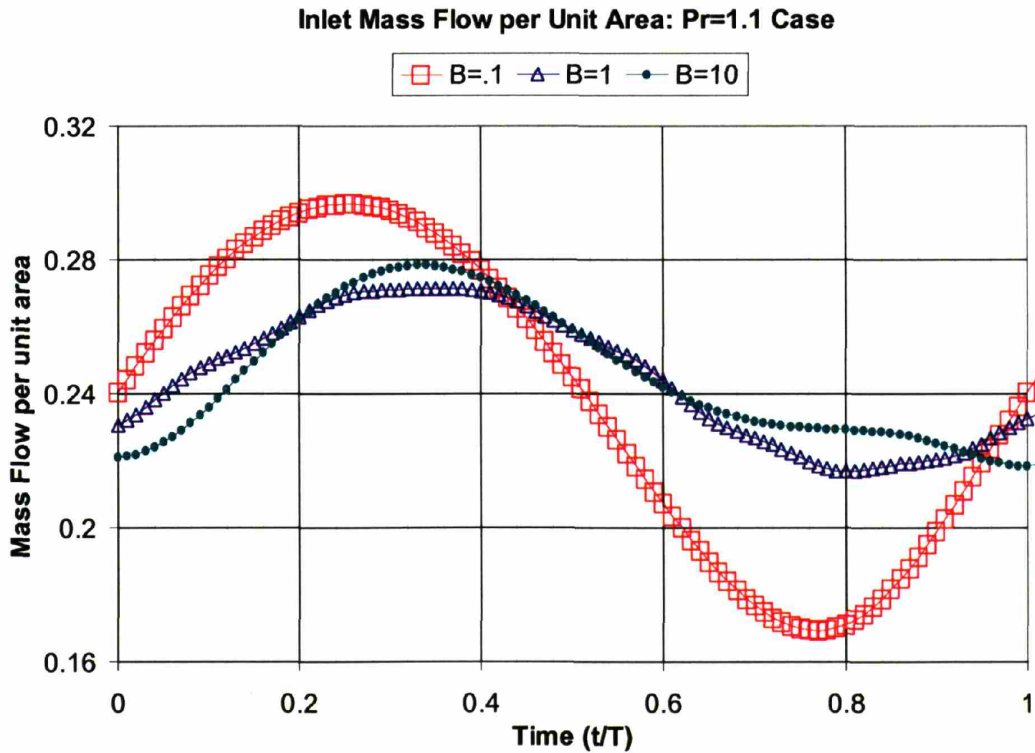
Figure 3-13 Inlet mass-flow-per-unit-area for the NPR=1 cases, showing a phase shift for the higher frequency cases

Magnitude of Velocity Fluctuations vs. Beta
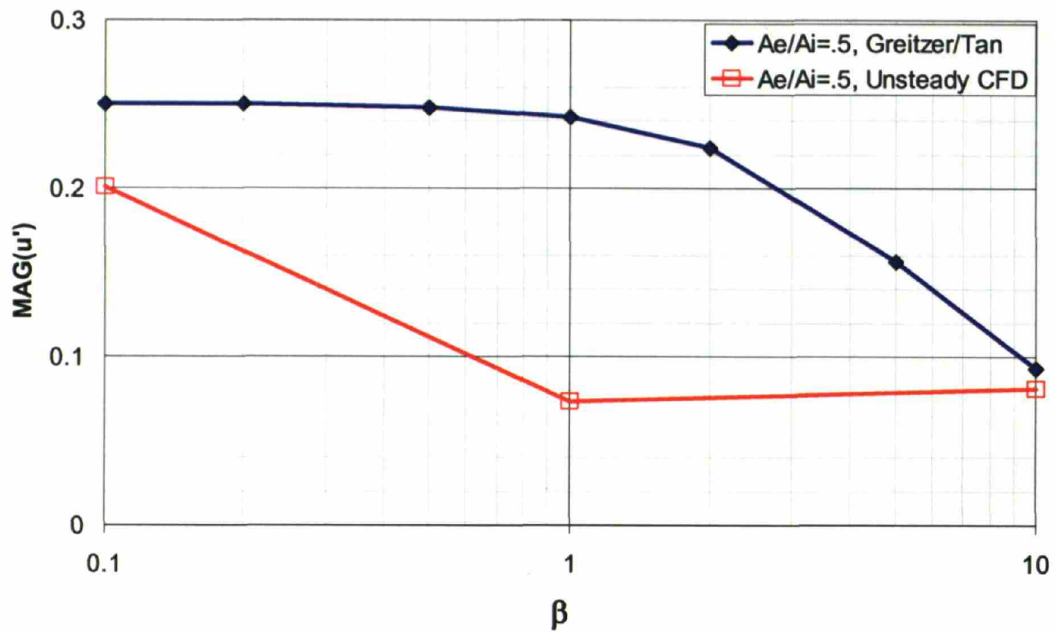
Figure 3-14 CFX computed velocity magnitude compared with a 1D analysis, which shows good agreement at low (β=.1) and high (β=10)

Phase of Velocity Fluctuations vs. Beta
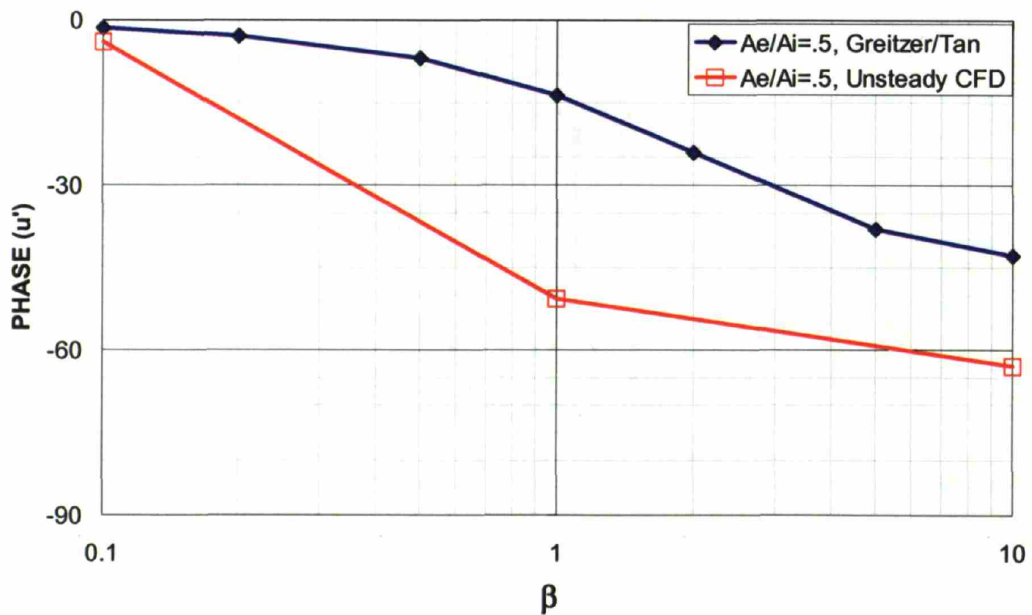
Figure 3-15 CFX computed velocity phase compared with a 1D analysis, which shows that CFX agrees well at low frequency

Error in Steady-Estimated Flow per Unit Area
Comparison with CFD Results
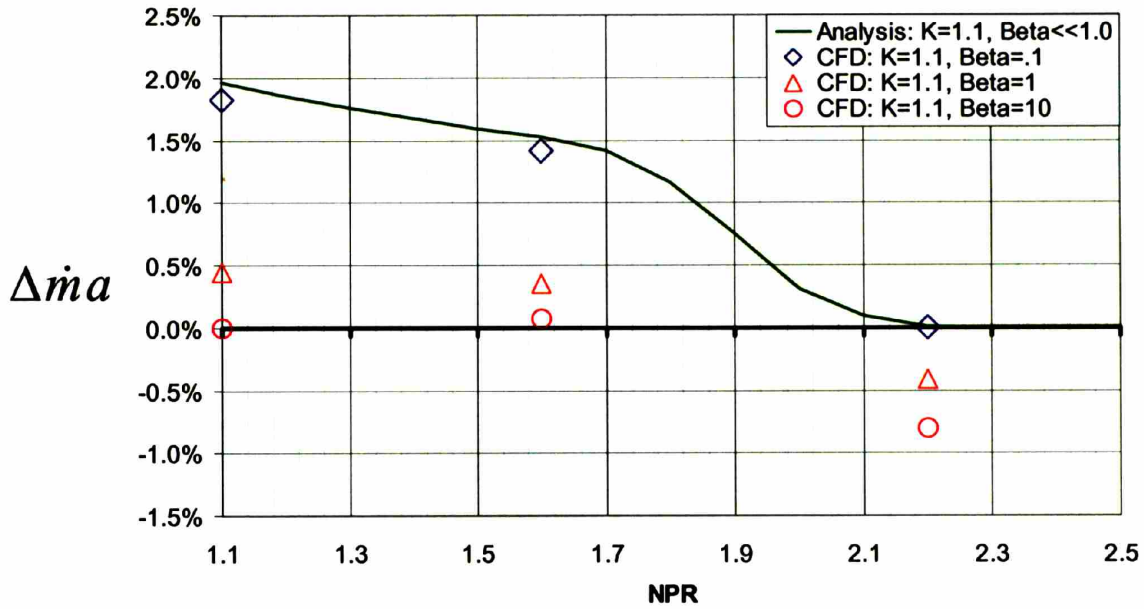
Figure 3-16 CFX computed difference in mass flow. The low-frequency CFD calculations are in accord with the quasi-steady analysis

Quadratic Mass Flow Term, u'ρ': NPR=2.2
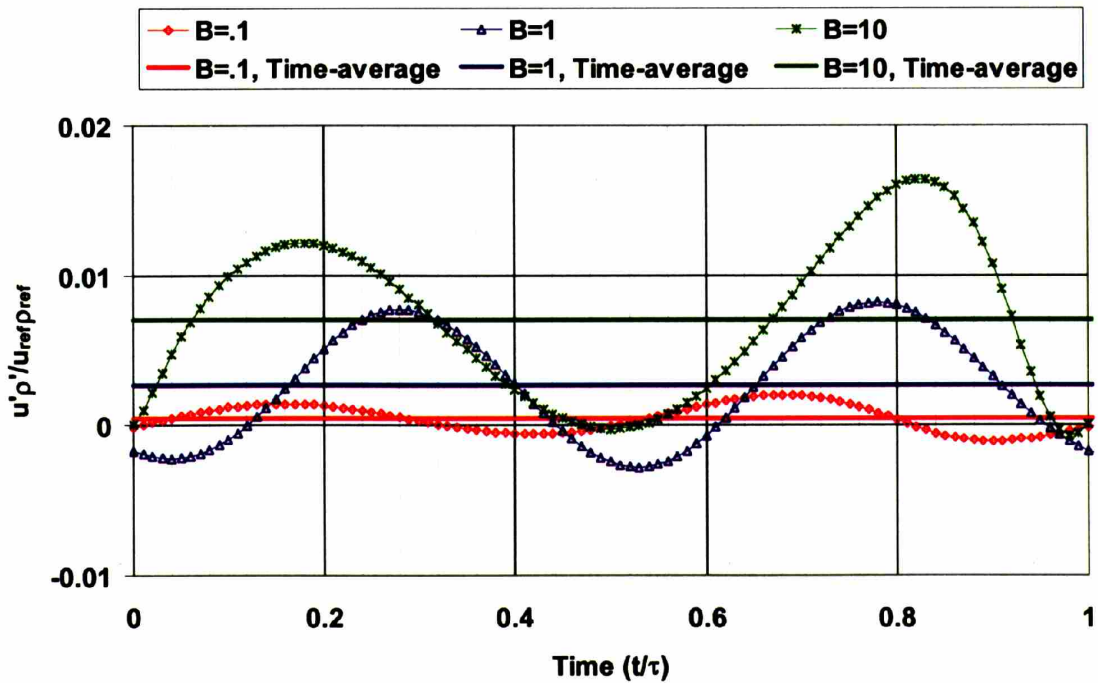
Figure 3-17: Product of density and velocity perturbation showing increased magnitude for higher-frequency cases
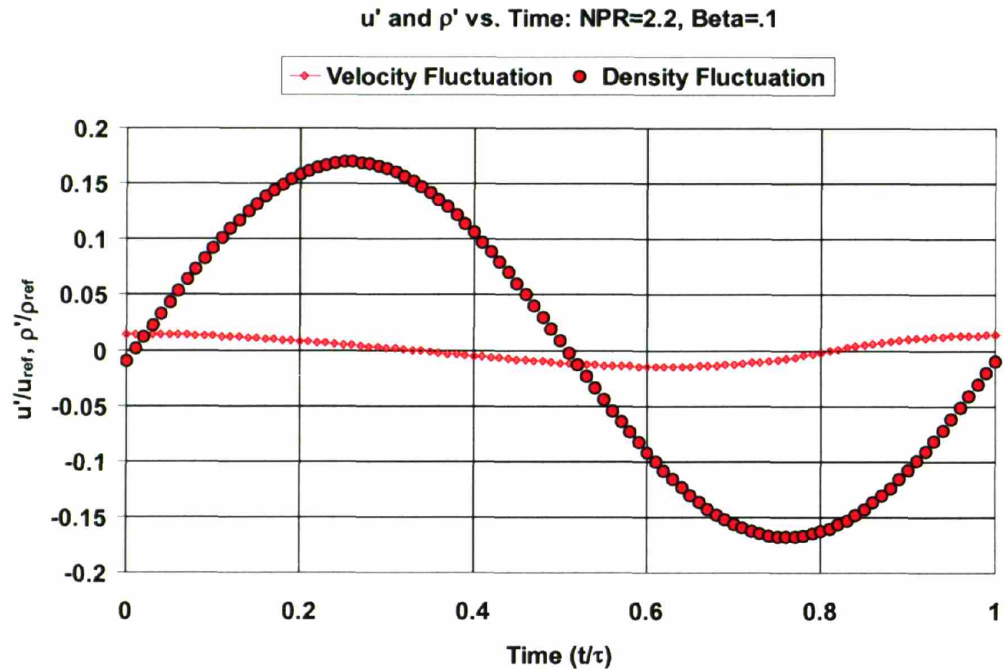
Figure 3-18 Velocity and density perturbation for β =.1 show that velocity and density fluctuations are out of phase
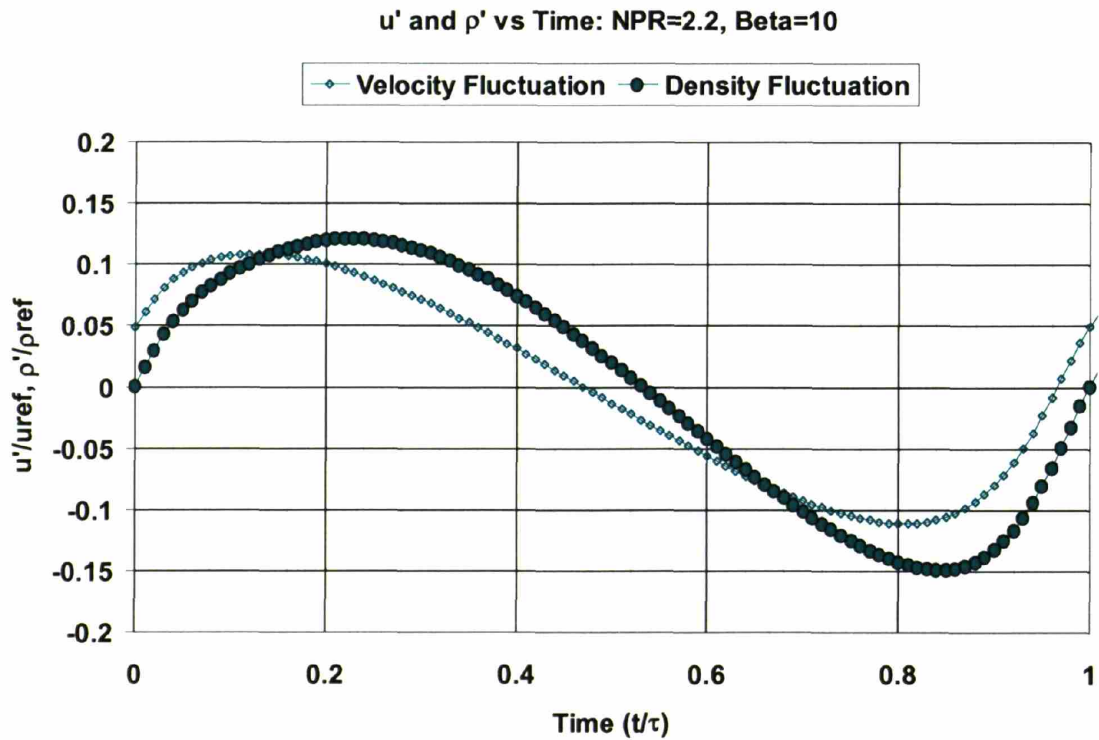
Figure 3-19 Velocity and density perturbation for β =10 show that velocity and density fluctuations are in- phase, which leads to a higher time-averaged mass flow

4. Results for the 2D Unsteady Impeller-Diffuser Model

4.1 Introduction

Chapter 1 poses the following research issue; identifying the design parameters that control the level of unsteady loading in a centrifugal compressor stage. A quasi-2D model is used to analyze the time-accurate flow field in the research compressor. This approach is selected to isolate only the potential-flow interaction of the downstream static pressure disturbance with the upstream impeller. By this means, the role of potential flow interaction on impeller loading can be directly quantified.

Four specific diffuser designs are developed to aid in identifying the controlling parameter that sets the upstream extent of the unsteady impeller loading. The results of these four calculations are presented in this chapter. The results indicate clear differences in unsteady loading as the impeller-diffuser gap and the diffuser throat area is varied. The static pressure field in the impeller/diffuser gap is analyzed, and it is shown that increased gap leads to increased decay of the static pressure disturbance and thus a reduced level of unsteady loading on the impeller blade. Upstream influence of the diffuser vane is identified as the driver for the observed effect of impeller-diffuser gap.

The effect of throat change cannot be isolated because the stable operating range of the compressor changes with throat area. Therefore, the cases with increased throat are are analyzed at higher mass flows than that of the baseline design. Cases with increased throat show a significant improvement in the upstream attenuation of the static pressure disturbance. A hypothesis is formulated: Increased mass flow leads to decreased diffusion in the impeller relative frame and thus increased attenuation of the static pressure disturbances upstream of the impeller trailing edge. This motivates additional studies in chapter 5 on an isolated impeller subjected to an unsteady pressure disturbance to assess the hypothesis.

4.2 Results

4.2.1 Time-averaged Operating Conditions

Changes in throat geometry cause a shift in the computed stable operating range of the 2D compressor. Increased throat area leads to an increase in the choked flow capacity of the machine. With reference to equation 3.10, it is clear that an increase in area results in an increase in corrected mass flow capacity. However, the minimum mass flow for numerical stall-free operation also increases. Therefore, the operating range of the configurations with increased throat area is shifted to higher mass flows.

Figure 4-1 is the compressor map corresponding to the approximation of the centrifugal compressor on a quasi-2D basis as described in Chapter 2. Solid lines represent the steady-state mixing plane calculation and the large symbols are the time-averaged values from the unsteady simulation. Case A and B are computed at similar corrected mass flows of approximately 0.65. The mass flow (per unit area) is lower than the 3D model, but the midspan inlet flow angle (α_1) is modified to match the impeller relative flow angle (β_1), as described in chapter 2. Case C, at a corrected mass flow of 0.78, is at an operating point away from the numerical stall point. Case D is run to a corrected mass flow of 0.89. Case D has a limited range because the diffuser is not well matched to the impeller.

4.2.2 Source of Unsteadiness in the Impeller

Before comparing the results of different designs, it is important to illustrate the source of unsteadiness in the impeller, namely the upstream influence of the diffuser static pressure disturbance. Figure 4-2 shows time-accurate normalized static pressure contours for 6 instances in time for case A, the baseline model. The letter S in these plots denotes the splitter blade. The effect of the diffuser vane on the static pressure distribution can be described as follows. Static pressure is higher in the region directly upstream of the vane than in the mid passage region. This is reflected in the streamline

adjustment that occurs in the vaneless space. Circumferential static pressure gradients are a direct consequence of the flow stagnation that occurs upstream of the diffuser vanes.

At time t=1/12 τ, the splitter pressure surface is just in front of the zone of high static pressure, while the suction surface is exposed to lower static pressure. At the next instant, 2/12 τ, the splitter has penetrated this region, and there is a strong increase in static pressure on the splitter pressure surface with peak values of 2.1. The mid-passage is approximately 0.9. No such increase is observed on the suction surface at this instant. There is thus a significant net pressure difference across the blade. At time 3/12 τ, the zone of high static pressure has weakened to 1.8 and the disturbance has propagated in the upstream direction. A downstream reflection of this disturbance is also present, which is illustrated by the high static pressure extending further downstream than in the previous timestep. At time 4/12 τ, the region of high static pressure continues to propagate both upstream and downstream, and the strength of the disturbance is weakened to 1.5. The next two instances in time further illustrate the propagation and decay of the static pressure disturbance as the impeller continues to rotate in time. Note that at time 6/12 τ, the pressure surface is exposed to a lower static pressure than the suction surface, leading to a reversal of the loading.

Inspection of the time-accurate pressure field illustrates the source of unsteadiness. The impeller sees a periodic static pressure disturbance as it rotates through the static pressure field set up by the diffuser vane. This disturbance interacts with the impeller blades and results in a backward and forward traveling static pressure disturbance. As the blade rotates through the disturbance, the static pressure increase on the pressure surface occurs prior to the increase on the suction surface. Figure 4-3 shows the unsteady splitter blade static pressure along the chord at time instant 2/12 τ. At this instant, pressure side static pressure peaks at 97% chord while suction side static pressure peaks at 83% chord. In addition, the static pressure increase is stronger on the pressure surface than the suction surface. The implication is that there is a strong static pressure difference across the blade, and thus substantial changes in loading, which varies periodically in time.

4.2.3 An assessment on the upstream extent of pressure fluctuations

Equation 2.10 in chapter 2 defines the variable P_f as a metric of unsteadiness. P_f represents the peak-to-peak static pressure fluctuation during 1 characteristic period of motion. This period represents the time required for the splitter blade to proceed from a diffuser vane leading edge to the next. High levels of P_f indicate regions of strong unsteadiness. Figure 4-4 shows contours of P_f plotted on the meridional plane of the impeller for all four cases, while Figure 4-5 shows the same results but a close-up view of the impeller trailing edge.

Comparison of case A and case B are useful for assessing the effect of gap on unsteadiness. Both cases show P_f values near 1.0 across the exit plane of the impeller as seen in figure 4-4. Peak values of 1.7 are seen at the trailing edge pressure surface, which indicates strong interaction when the blade surface passes through regions of high static pressure. Toward the leading edge of the splitter, contour of 0.5 can be observed near the in both cases (Figure 4-4). This indicates strong unsteadiness in the leading edge region of the impeller. The two significant observations from this comparison are:

1) Levels of unsteadiness are similar for the baseline and increased gap calculation

2) Strong unsteadiness is present in the splitter leading edge region for both cases

Comparison of case A and case C are useful for assessing the effect of throat and corrected mass flow on the level and upstream extent of pressure unsteadiness. Similarly to case A, P_f levels of 1.0 are observed across the impeller exit plane in figure 4-4. Significant differences are apparent in the upstream propagation of the disturbance. Case C shows significantly reduced P_f levels of 0.2 at the mid-chord and forward, while Case A had levels of 0.5 (Figure 4-4). The significant observation from this comparison is:

1) Increased throat area and corrected mass flow lead to significant improvements in the attenuation of the pressure disturbance in the impeller

Comparison of case A and D show the combined effect of increased gap and increased throat/mass flow. Case D shows even further reduction in the level of unsteadiness in the impeller. Levels are reduced to 0.1 from approximately 80% chord and forward. The results from case A, C, and D imply a trend that as corrected mass flow and throat area are increased, the upstream attenuation of the pressure disturbance continues to improve.

4.2.4 Comparison of splitter loading

The results presented in section 4.2.3 show a strong difference in unsteadiness for the four cases examined. In order to assess the impact of this unsteadiness has on aeromechanics response, it is necessary to examine the fluctuations in dynamic load on the splitter.

Figure 4-6 shows the loading across the splitter plotted along the chord for case A. Each line represents one instant in time during one characteristic period. Strong peak loading up to one dynamic head is observed at the trailing edge. Levels are reduced to 0.6 and below toward the leading edge, but there is significant unsteadiness present up through 0.3 chord. Comparison with case B in Figure 4-7 shows some reduction in the peak-to-peak loading at the trailing edge, but there is no significant difference in the upstream extent of the unsteady loading on the splitter blade.

Figure 4-8 shows the unsteady loading for case C. Peak levels at the trailing edge are similar to case A. However, the attenuation of the unsteady loading disturbances in case C is distinctly different. While case A shows little attenuation until leading edge, case C shows strong decay beginning at the trailing edge which vanishes at 0.25 chord. Peak loading was shown as 0.6 for case A (in the 0.2-0.4 chord range), but was reduced to 0.1 for case C (at the same location). This observation is consistent with the trend implied in the P_f contours, which shows a strong decrease in the level of unsteadiness for case C. Figure 4-9 shows the loading for case D. The magnitude of peak loading is 0.5 at the trailing edge, which is a 50% reduction in magnitude relative to case A. The attenuation also shows an additional improvement from case C levels.

4.2.5 Summary of Results

Figure 4-10 shows the difference in maximum and minimum loading, ΔL_s on a semi-log plot during one characteristic period for all the 4 cases. This parameter, ΔL_s, is a metric that quantifies the level of load fluctuations. ΔL_s is plotted on a semi-log scale, so the solid grades on the y-axis represent an order of magnitude change in ΔL_s. Comparison of case A and B show that while case B (with increased gap) has lower load fluctuations than case A at the trailing edge, is has a significant value of ΔL_s in the leading edge region, similar to case A. Comparison of case A and C show that case C (increased throat and corrected mass flow) has similar peak loadings, but significantly better upstream attenuation. Case D, with increased gap and increased throat/mass flow, shows the lowest peak loading with the most rapid decay of ΔL_s to vanishing levels at an upstream location of 0.4 chord.

Based on these observations, two design variables are identified as significant contributors to the unsteady loading in the centrifugal compressor. These two variables are impeller-diffuser gap and corrected mass flow.

First, increasing the **impeller-diffuser gap** reduces the level of peak dynamic loading in the stage (for fixed pitch). Case A and B (increased gap) at similar values of mass flow show a reduction in peak loading, while case A and C (baseline gap) at different values of mass flow show nearly identical peak loading. **Upstream influence** is the mechanism responsible for this change, and increased vaneless space causes the increased decay of the disturbance prior to reaching the impeller vane.

Second, increasing the **corrected mass flow** decreases the **stage loading** which **improves the upstream attenuation** of the unsteady load imposed on the splitter. Stage loading refers to the total amount of work done on the fluid in the impeller. Figure 4-10 clearly shows similar attenuation for case A and B (same flow) and increasing attenuation for case C and D respectively. Thus it may be inferred that the throat geometry is not a direct controlling parameter and that **flows with decreased diffusion are less sensitive** to changes in the unsteady static pressure associated with the downstream diffuser. Thus an

improvement in the splitter blade unsteady loading is to be anticipated. In the next section, the computed flowfields are further interrogated to support these hypotheses.

4.3 Interrogation of local flow quantities

4.3.1 Effect of Gap

We begin by interrogating the flow behavior in the vaneless space.

Figure 4-11 is a plot of the magnitude of the static pressure disturbance verses the distance from the diffuser leading edge. The magnitude is the peak-to-peak strength of the static pressure disturbance at a specific instant in time. Values of r/λ represent a non-dimensional distance, where r is the radial distance outward from the impeller trailing edge and λ is the diffuser pitch.

It can be inferred from the figure that the upstream decay of the disturbance is larger for Case B. The upstream effect can be quantified by solving Laplace's equation in a background flow with a periodic non-uniformity [16]. The result of the analysis shows that the magnitude of a periodic disturbance will propagate forward and decay exponentially in accordance with

$$P'(x) \alpha \ P'_0 \ e^{2\pi k \frac{r - r_{le}}{\lambda}} \qquad \text{(eq 4.1)}$$

where k is an integer referred to as the harmonic number, λ is the disturbance wavelength, r is the distance upstream (the radial distance upstream from the diffuser leading edge), r_{le} denoted the value of r at the diffuser leading edge and P'_0 the initial disturbance strength. A k value of one represents the fundamental harmonic of the disturbance. Although the assumption of incompressible flow and zero streamwise pressure gradients do not apply to this vaneless space, the description of upstream influence can be viewed as an approximation.

Upstream influence is further elucidated in Figure 4-12, which shows contours of time-averaged static pressure for each of the four cases. Case A shows a strong region of

high static pressure in front of diffuser vane, and the disturbance strength is still large at the upstream boundary of the diffuser domain. In contrast, case B shows that the disturbance present at the diffuser leading edge decays in the vaneless space. Case C, similar to Case A, shows a strong circumferential gradient at the leading edge, but has a minimal decay prior to reaching the upstream boundary of the diffuser domain. Case D shows a much weaker initial gradient and strong decay in the vaneless space. The weaker initial gradient for case D is due to the fact that higher mass flow results in lower inlet swirl, and therefore less streamline curvature is needed for flow adjustments.

The observation that impeller-diffuser gap affects the level of unsteady loading is supported by the interrogation of the flow in the vaneless space. Magnitude of the static pressure disturbance imposed on the impeller is reduced as the impeller-diffuser gap is increased. Upstream influence is identified as the responsible flow process.

4.3.1   Effect of stage loading changes

It was hypothesized in section 4.2 that stage loading is a controlling parameter on the level of unsteadiness. This hypothesis is to be examined by interrogation of local flow quantities related to stage loading. Figure 4-13 shows the normalized time-averaged static pressure rise plotted along streamwise position for all four cases. Cases A and B, at a corrected mass flow of approximately 0.65, have nearly identical static pressure rise. Case C, with a corrected mass flow of 0.78, has a slightly less static pressure rise, and case D the lowest. Figure 4-14 shows the time-averaged relative Mach number for all four cases. Cases C and D have higher exit Mach numbers, and thus lower relative frame diffusion. Interrogation of static pressure rise and relative frame Mach numbers demonstrate that there is decreased diffusion associated with increased corrected mass flow.

Stage loading can be quantified by the ratio of exit to inlet relative velocities. This ratio is the DeHaller number, and is a metric for quantifying stage loading [3]. Figure 4-15 shows the DeHaller number for each of the four cases. It shows that case A and B, which have similar attenuation, have nearly identical values of DeHaller number

(approximately 0.8). Case C, which shows improved attenuation, has a value of .95. Case D, which shows even further attenuation over Case C, has a value of 1.2. This suggests that decreased stage loading is responsible for the observed improvement in attenuation with increased corrected mass flow.

The preliminary conclusion is that increases in corrected mass flow lead to decreased diffusion and thus stronger attenuation of the static pressure disturbance. However, the effect of corrected mass flow cannot be de-coupled from the geometric change in the throat. In order to substantiate the suggestion that stage loading is the controlling parameter, chapter 5 addresses the attenuation of a disturbance in an isolated impeller where the presence of the diffuser is approximated via an imposed unsteady static pressure field. By removing the effect of the downstream geometry, the effect of mass flow can be isolated.

4.4 Summary

Results from an unsteady simulation of flow in a quasi-2D representation of the research compressor stage are interrogated to arrive at the following key results:

- Increased impeller-diffuser gap reduces the level of peak dynamic loading on the splitter blade
- Increased corrected mass flow leads to improved upstream attenuation of the static pressure disturbance.

The implication of these results is that the following hypothesis can be put forward:

- Upstream influence associated with the downstream diffuser is the cause for the observed decrease in the peak dynamic loading as the impeller-diffuser gap is increased

- Decreased diffusion in the impeller passage results in the observed improvement in upstream attenuation with increased corrected mass flow.
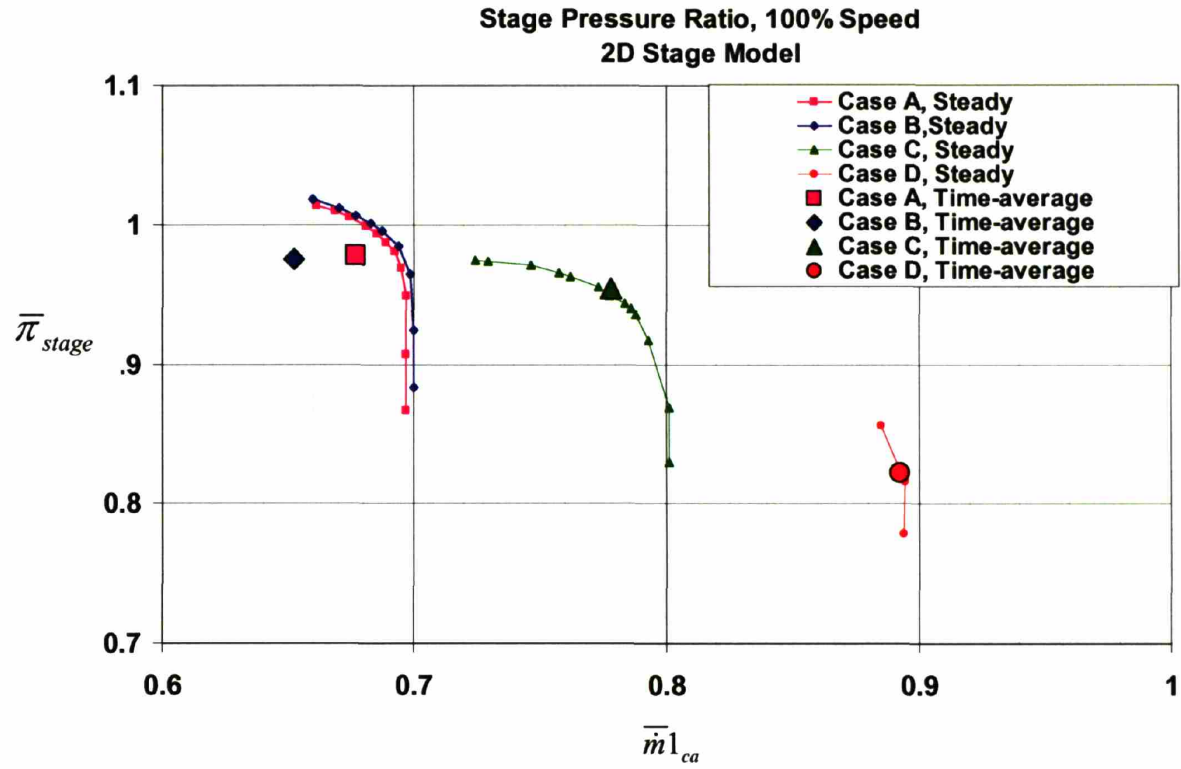
Figure 4-1 Compressor map computed based on the quasi-2D approximation of the centrifugal compressor stage

Figure 4-2 Normalized static pressure distribution (P_n) for 6 instants during ½ diffuser passing period

Splitter Surface Static Pressure
t=2/12 T
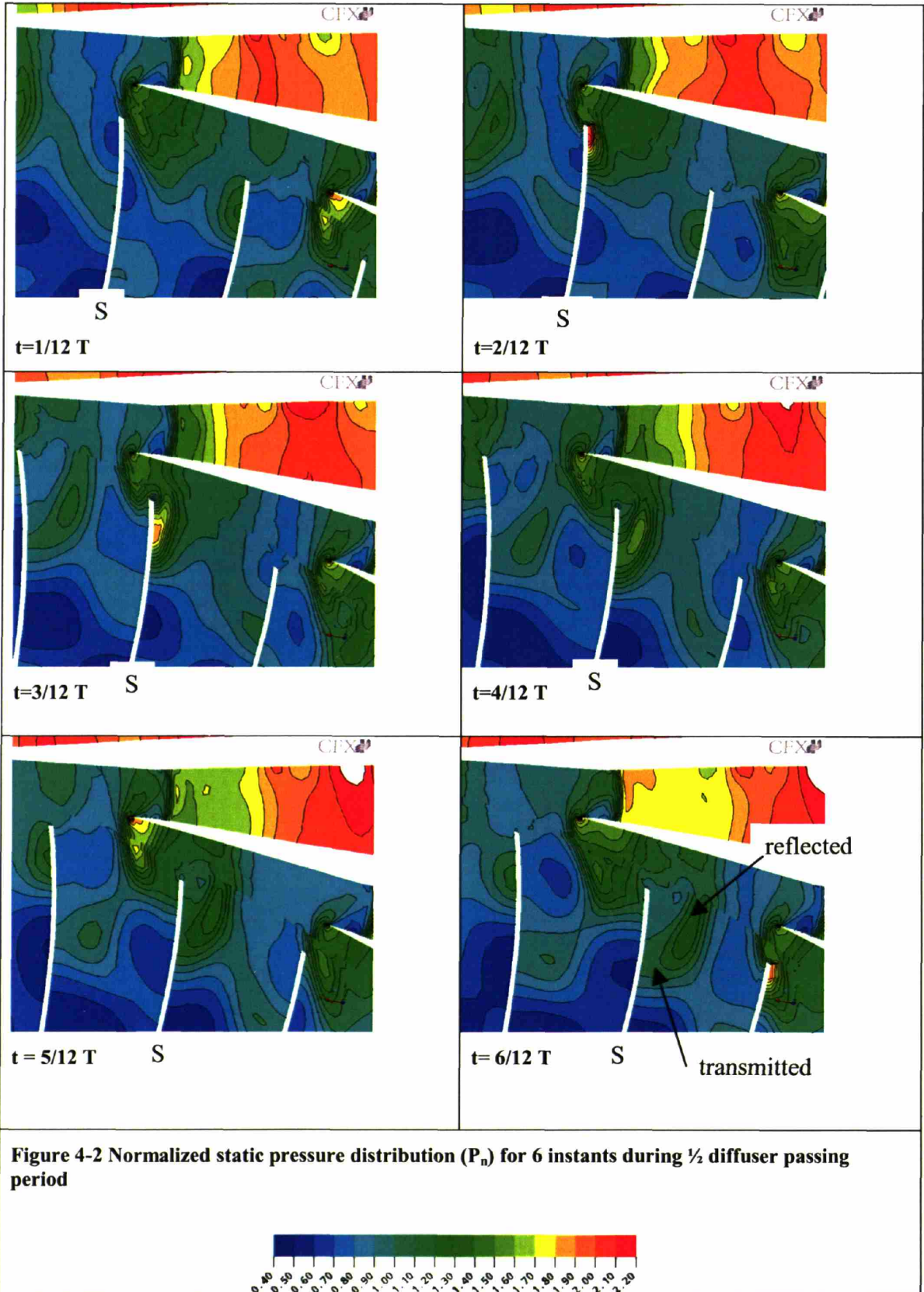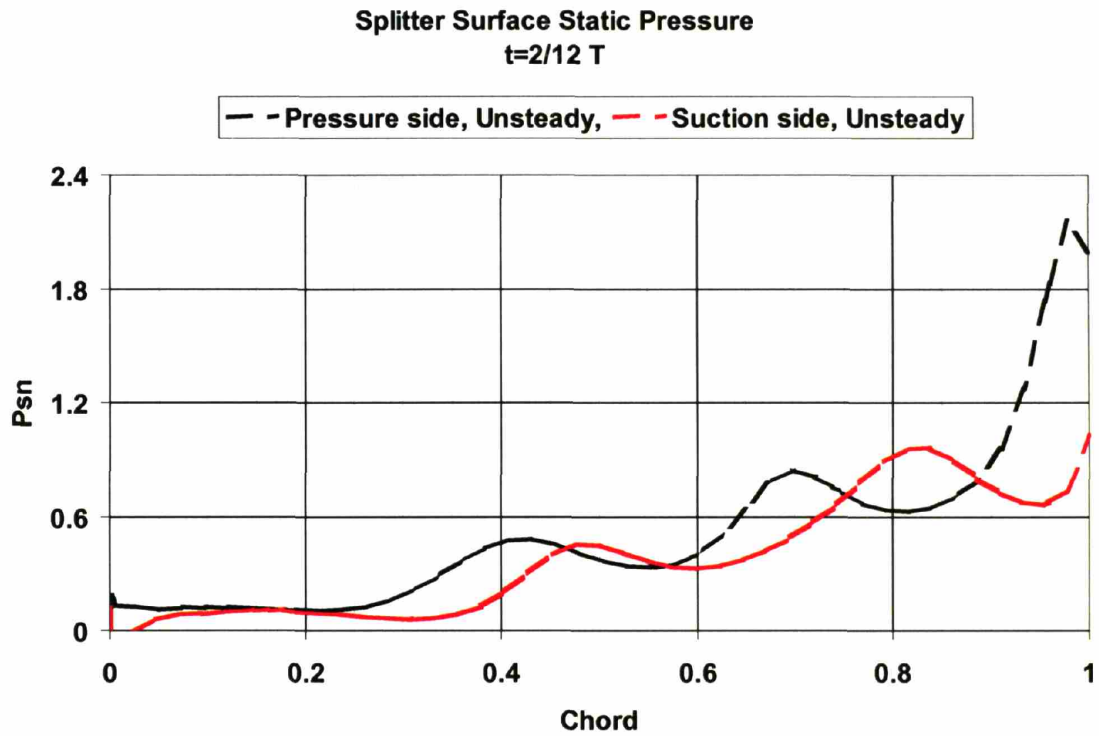
Figure 4-3 Splitter blade static pressure at time instant t=2/12 T, indicating sharp increase in static pressure on pressure side near the trailing edge
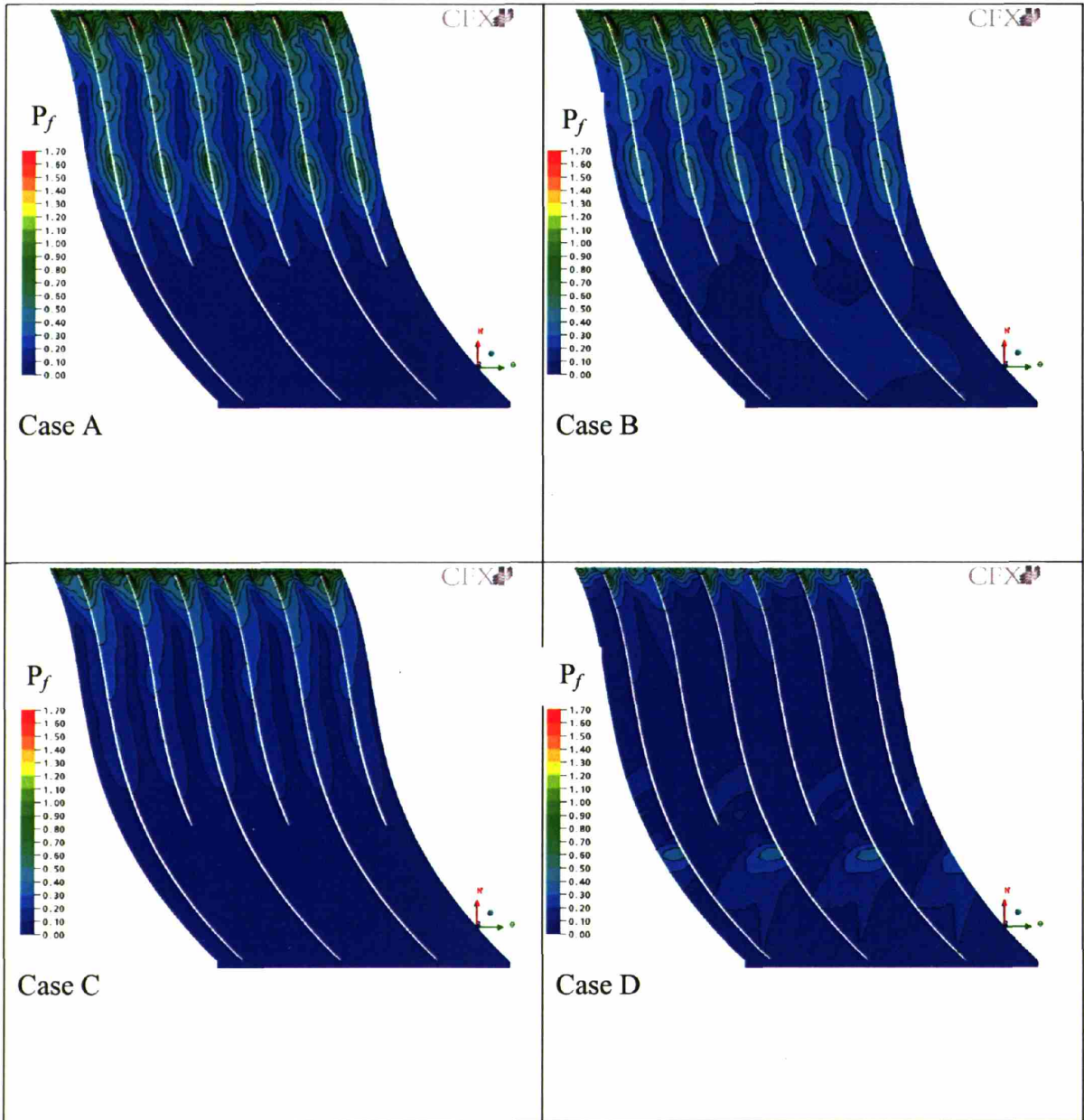
Figure 4-4 Contours of Pf for 4 cases to elucidate regions of significant unsteadiness
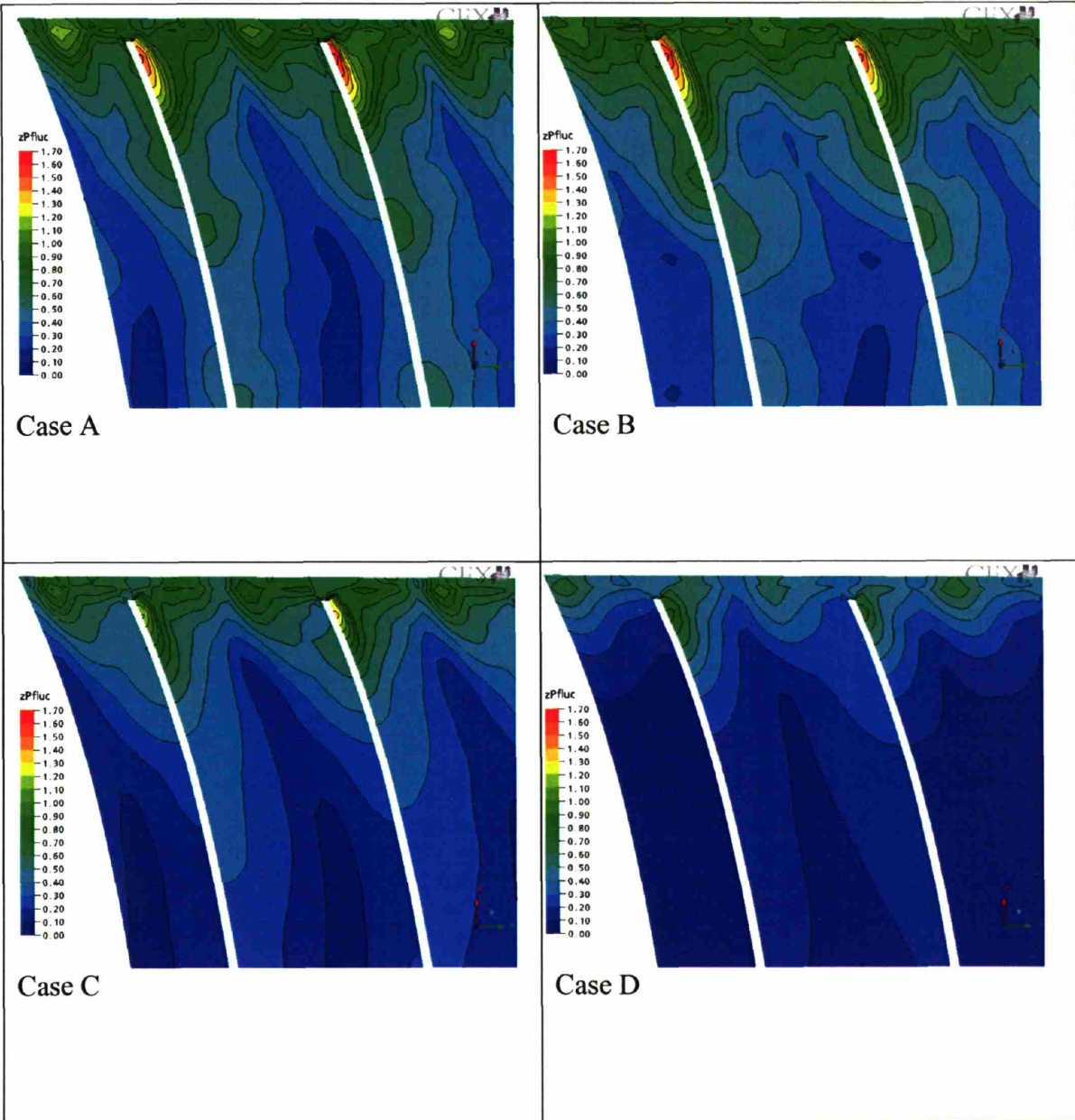
Figure 4-5 Contours of Pf for 4 cases showing a close-up at the impeller trailing edge to elucidate the high levels of unsteadiness on the pressure surface trailing edge A and B

Unsteady Splitter Load
Case A: Mdot=.68
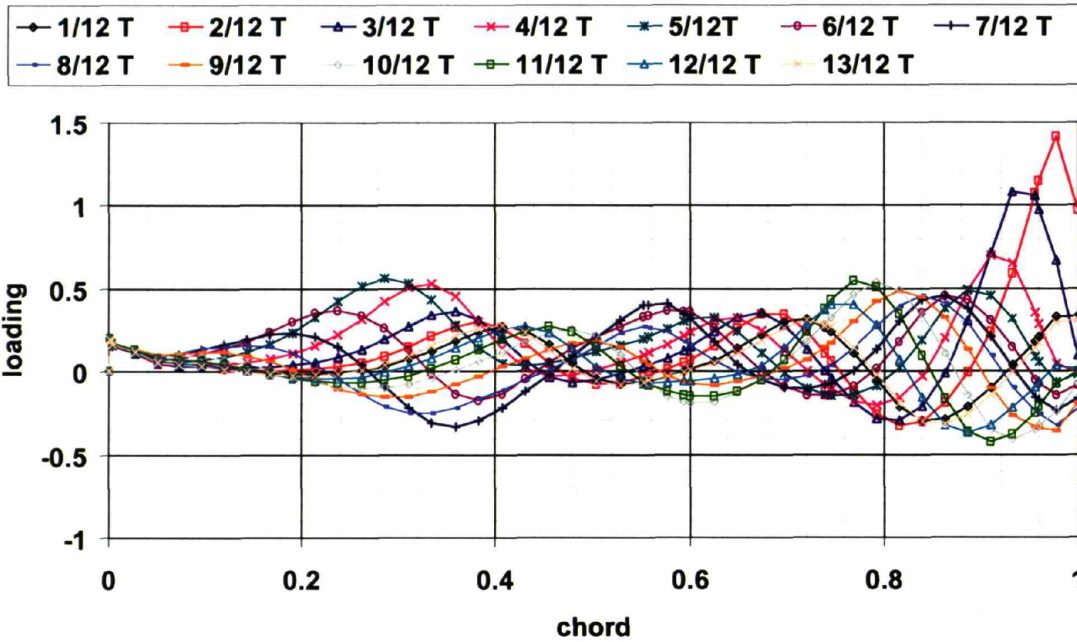
Figure 4-6 Unsteady splitter chordwise loading distribution for case A indicating significant blade loading variation at the leading edge region

Unsteady Splitter Load
Case B: Mdot=.68
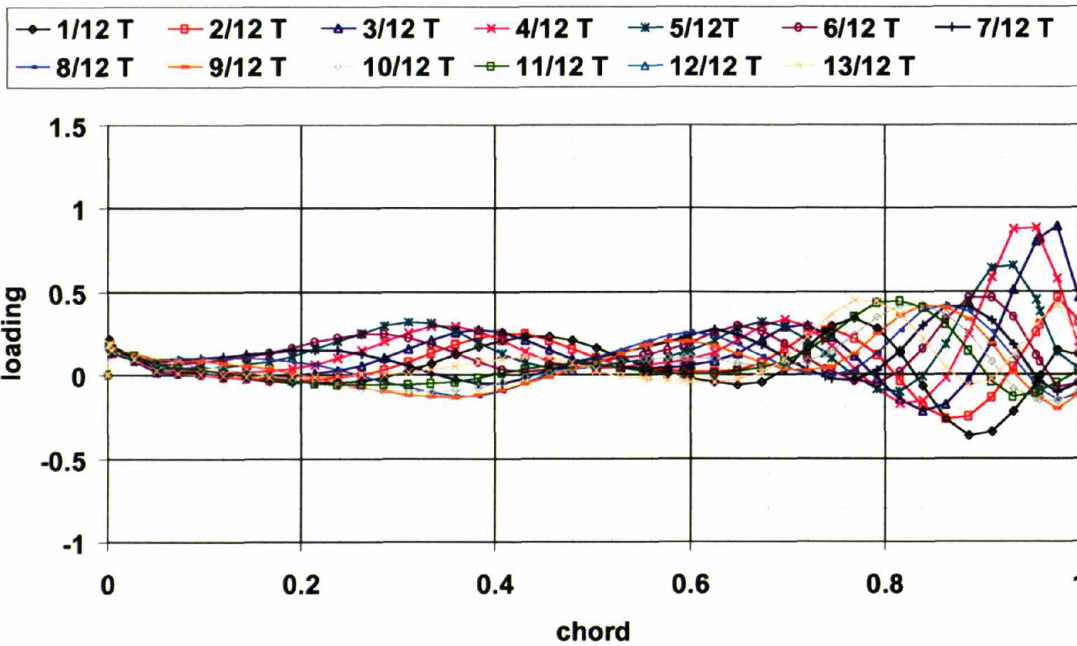
Figure 4-7 Unsteady splitter chordwise loading distribution for case B indicating reduced trailing edge loading relative to case A, but significant loading variation at the leading edge region

**Unsteady Splitter Load
Case C: Mdot=.78**
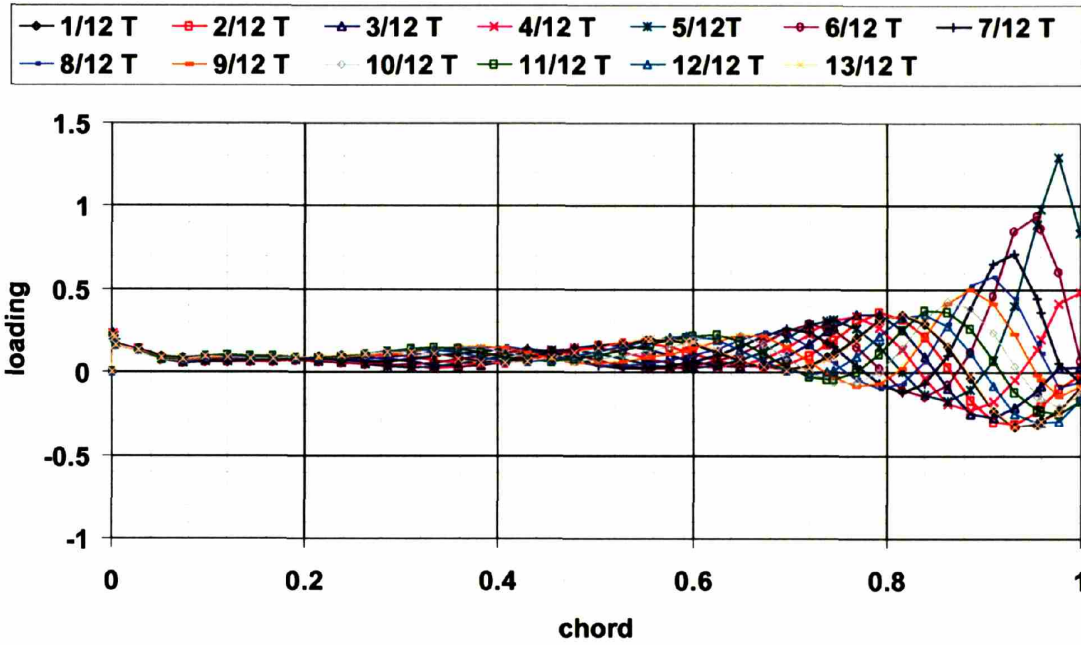
Figure 4-8 Unsteady splitter chordwise loading distribution for case C showing a significant reduction in loading near leading edge relative to case A

**Unsteady Splitter Load
Case D: Mdot=.89**
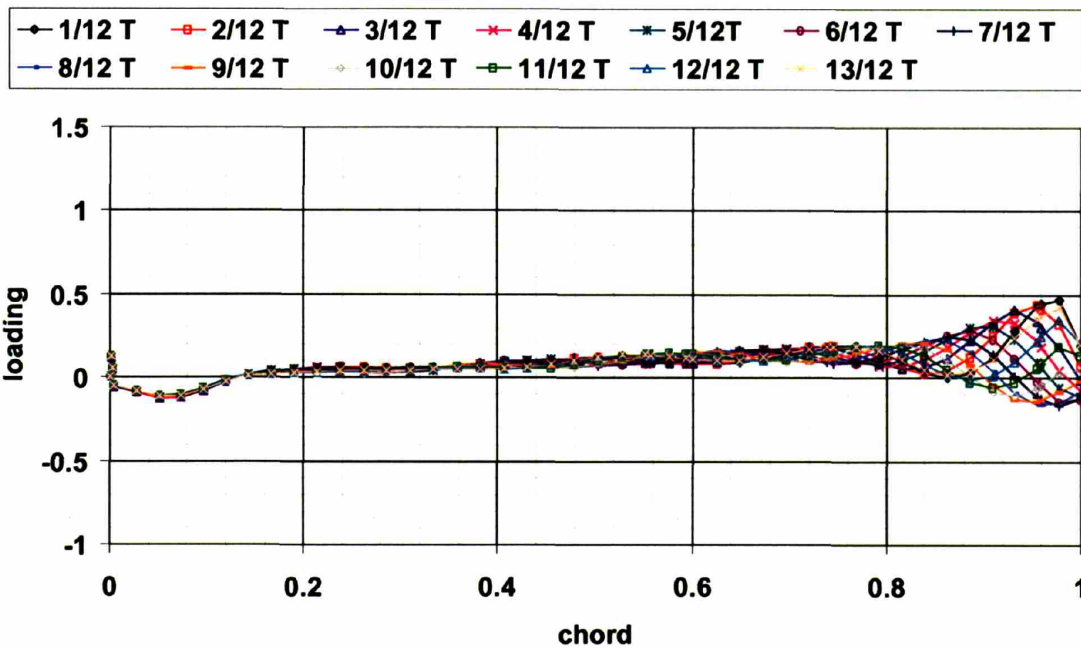
Figure 4-9 Unsteady splitter chordwise loading distribution for case D showing a significant reduction in loading near the leading edge

95

Peak-to-Peak Load Fluctuation
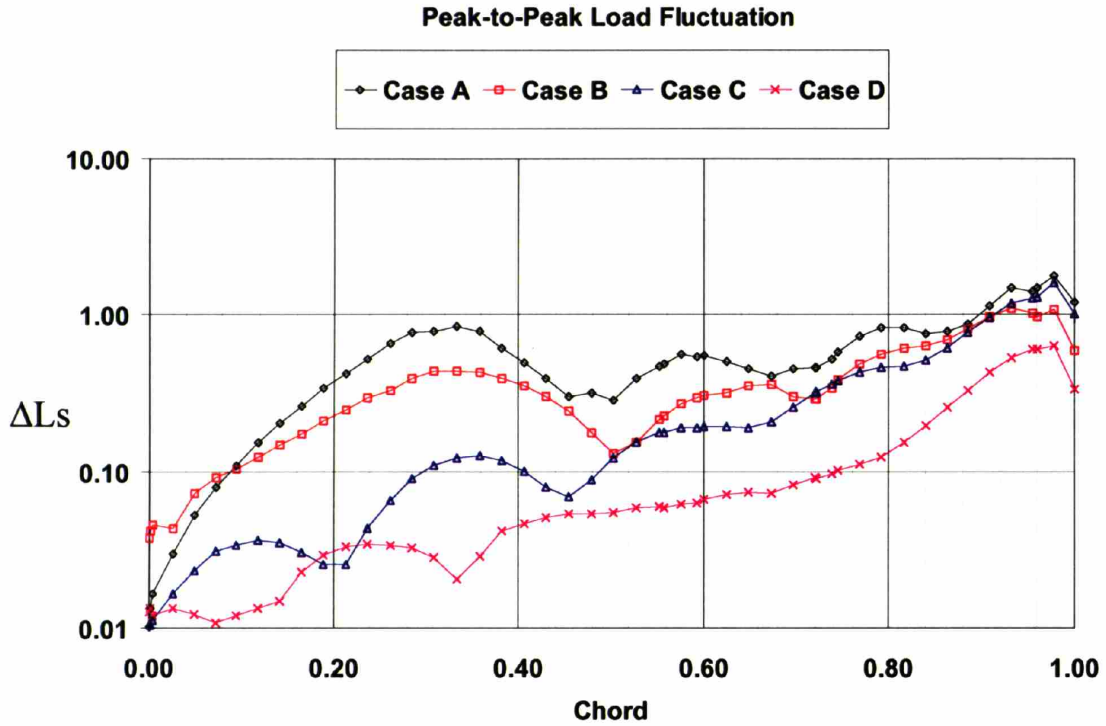
Figure 4-10 Strength of loading fluctuation vs. distance along splitter chord, showing differences in disturbance strength between cases A-D

Decay of Static Pressure Disturbance in Vaneless Space
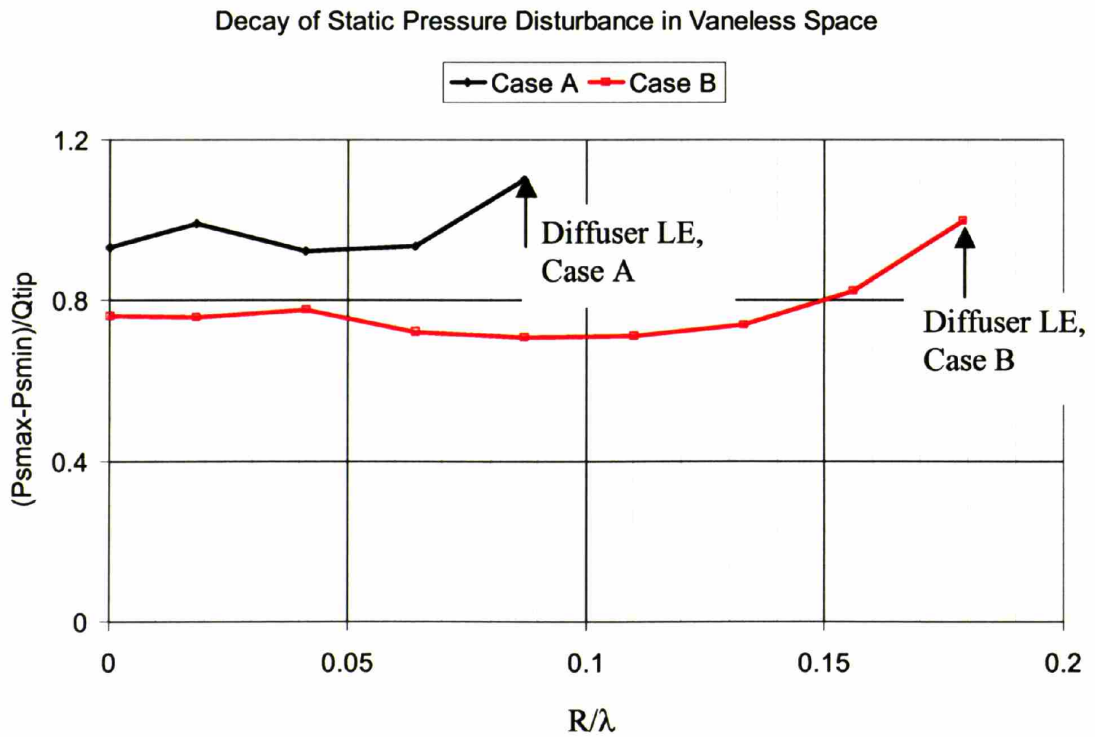
Figure 4-11 Decay of static pressure disturbance in vaneless space showing the effect of increased gap on the strength of the disturbance imposed at the impeller trailing edge
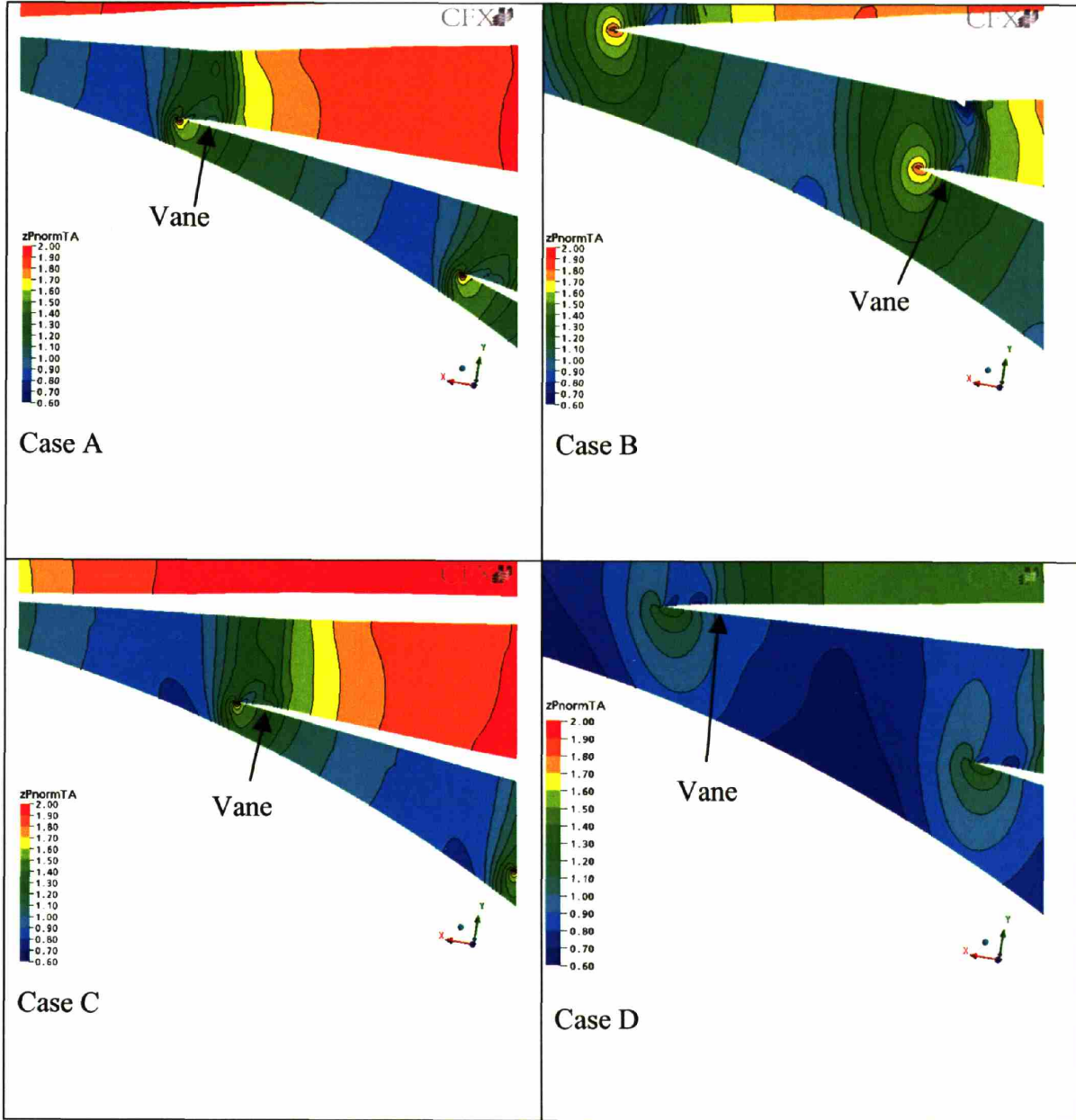
Figure 4-12 Time-Averaged normalized static pressure near diffuser leading edge shown to elucidate the decay of the static pressure disturbance in the vaneless space

Time Averaged Static Pressure Rise
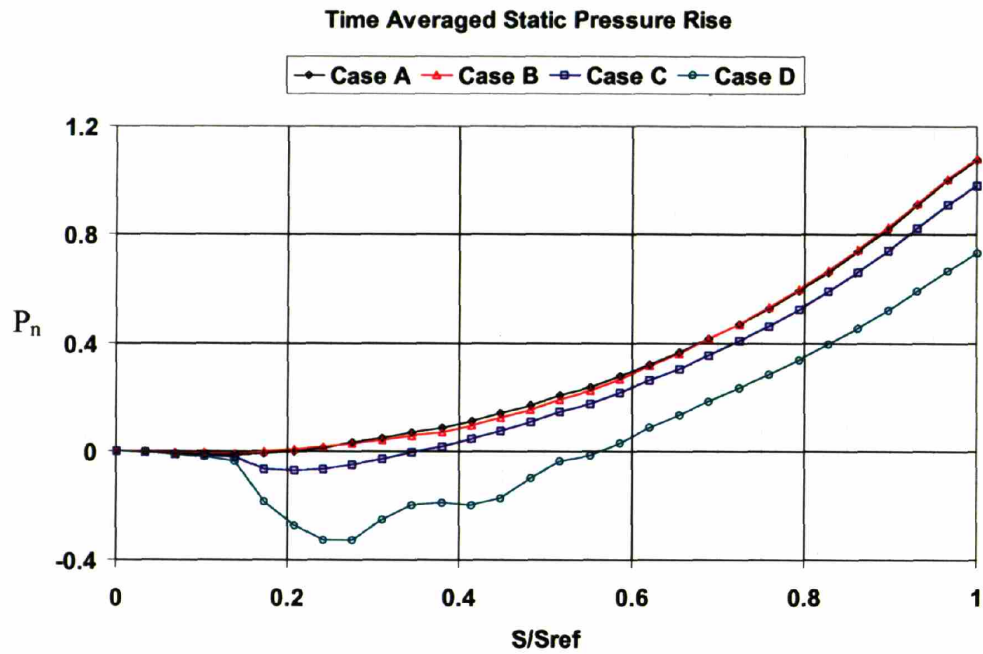
Figure 4-13 Time-averaged normalized static pressure rise showing increased pressure rise for cases A and B

Time-Averaged Relative Mach Number
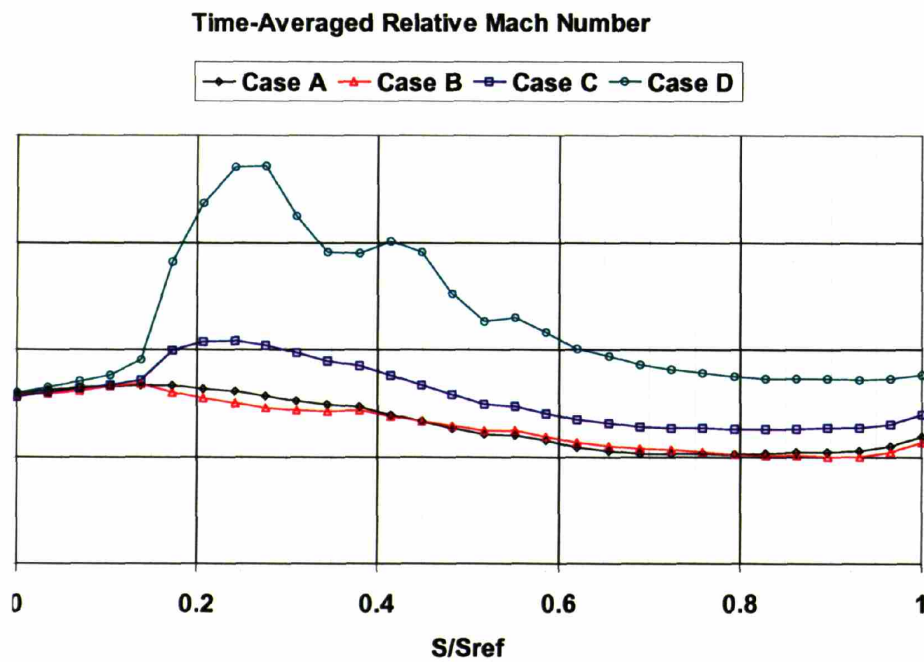
Figure 4-14 Time-Averaged and mass averaged relative Mach number in the impeller passage, showing lower exit Mach numbers for cases A and B

De Haller Numbers in Quasi-2D Calculations
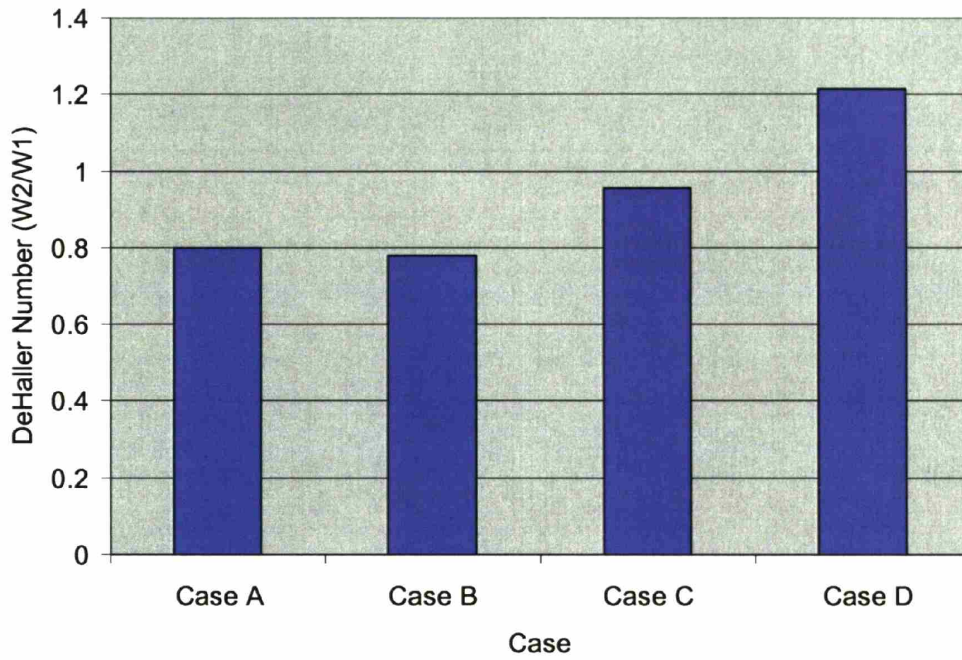
Figure 4-15 DeHaller number in quasi-2D calculations showing strongest diffusion for cases A and B

5. Results for the 2D Unsteady Impeller Model

5.1 Introduction

Results presented in chapter 4 indicated that increased throat and increased corrected mass flow lead to significant improvements in the attenuation of unsteady loading imposed on the impeller blade. A hypothesis is put forward that decreased diffusion associated with increase corrected mass flow is responsible for the improved attenuation. However, the effect of corrected mass flow and the effect of throat geometry cannot be de-coupled in the impeller-diffuser stage. As such, further assessment of the hypothesis is needed.

Therefore, a simplified model of the stage is developed. This model uses only the impeller geometry and simulates the diffuser via an unsteady static pressure boundary condition, as described in Chapter 2. The model is analyzed at five different corrected mass flows, three of which replicate the operating points of the impeller-diffuser stage that have been presented in chapter 4.

Results of the isolated impeller analysis show similar trends to the coupled model when corrected mass flow is varied. Because these trends are replicated with and without the presence of the downstream diffuser, the change in unsteady behavior must be attributed to the change in corrected mass flow. Thus this analysis would serve to support the hypothesis that decreased diffusion associated with increased mass flow is the driver for the improved attenuation of the unsteady load on the impeller blade.

5.2 Results

5.2.1 Time-Averaged Operating Conditions

Figure 5-1 and Figure 5-2 show the computed compressor pressure ratio and efficiency for a range of corrected mass flows. The solid line represents the steady-state

calculation and the four large diamond symbols represent the time-averaged results from calculation 5-8, as defined in chapter 2.

Figure 5-1 shows that the time-averaged operating condition for three of the isolated impeller calculations (denoted by red diamond symbols) is similar to the operating conditions from the previous coupled calculations (denoted by green triangle symbols). Corrected mass flow is deliberately matched to the coupled mass flow values so that flowfield comparisons can be made on a consistent basis. An additional calculation has been performed on the isolated impeller at a normalized mass flow of 0.55 in order to examine the trend at mass flows lower than that which have already been analyzed. Case 9, has been performed at the design flowrate. Note that this point does not fall on the characteristic line because the inlet flow angle is adjusted as defined in Table 2-1.

Examination of this set of time-averaged unsteady results indicate a reduction in stage pressure ratio relative to that which has been calculated in the steady model. At lower flow rates, the stage pressure ratio is reduced by 2-3%. However, at high flowrate, there is essentially no difference between the steady-state and time-averaged value. Figure 5-2 shows some reduction in stage efficiency as well. Time-averaged unsteady results are approximately 0.5 points lower in efficiency relative to the steady result for lower mass-flow cases. At high flow rates, there is no observed difference between the steady-state and unsteady time-averaged value. Although the mechanism behind this performance change has not been investigated as part of this research, further investigation could provide insight into this observation. A potential explanation of this change is the additional viscous dissipation that occurs in the unsteady situations.

5.2.2 Impeller Unsteadiness levels

Each of the three specific cases described in Section 5.2.2 has a similar mass flow as the corresponding coupled stage calculation. Thus a direct comparison of the computed flow fields can be made between the coupled model and the isolated impeller model. The goal of the comparison is to identify whether diffuser throat geometry changes or corrected mass flow changes are responsible for the observed changes in

attenuation of the unsteady load on the impeller blade. If the observed trends are replicated in the isolated model, it supports the conclusion that changes in corrected mass flow are directly responsible.

Figure 5-3 shows contours of P_f for the coupled and the isolated impeller cases at similar corrected mass flows. Comparison of Case A and Case 5 show similar attenuation of the unsteady static pressure disturbance. P_f levels of 0.5 can be observed on the blade surface through a substantial distance along the chord. In both cases, a contour of 0.1 near the leading edge indicates that pressure fluctuations of 10% of the dynamic head are still present at the splitter leading edge. Comparison of Case C and Case 6 also show similar levels of unsteadiness, again a contour of 0.1 is present near the splitter leading edge in both cases. The overall levels show some differences. Blade surface values through most of the passage peak at 0.2 for the coupled case, while values peak around 0.4 for the isolated impeller case.

Likewise, case 7 is similar to case D in trend. In general, the decay of the initial disturbance is similar. P_f levels of 0.5 and above are confined to approximately the last 10% of the splitter chord. There are some marked differences as well. The overall level of unsteadiness is stronger in case 7, the isolated impeller. One potential explanation for this difference is that the strength of the static pressure disturbance imposed on the impeller is weaker for case D than case 7.

Two additional calculations are performed in order to further investigate the trend in unsteadiness variation with stage loading. Figure 5-4 shows P_f contours for cases 8 and 9, respectively. Case 8 is at a corrected mass flow of 0.57, near the numerical stall point. Levels of unsteadiness are significantly higher than Case 5; P_f levels are in excess of 1.0 along most of the blade chord, which is approximately twice as strong as that in case 5. This provides additional support for the hypothesis that higher stage loading results in an increase in the level of unsteadiness.

Case 9 is designed to match the operating conditions of the research compressor. Mass flow is increased to 1.0, but inlet flow angle is adjusted to meet the original design. Thus the stage loading is similar to case 5. Results show much stronger attenuation relative to Case 5 and case A, despite the fact that the stage loading is similar between all

three cases. This suggests that stage loading may not be the only parameter that sets the level of upstream attenuation.

5.2.3 Splitter Loading

As was noted in chapter 4, it is necessary to compare fluctuations in dynamic loading on the splitter to understand the implications on aeromechanics response. Figure 5-5 shows the unsteady loading for Case 5. Strong unsteady loading extends up to 0.3 chord. Similar to cases A and B, there is very little attenuation until the leading edge of the splitter. Figure 5-6 shows the unsteady loading for Case 6, which is computed at a corrected mass flow similar to case C (but 15% higher than case A). There is a significant improvement in the upstream attenuation. Case 6 levels fluctuate between –0.1 and 0.2 at the mid-chord, while Case 5 shows load fluctuations between –0.5 and 0.5.

Figure 5-7 shows the unsteady loading for case 7. Case 7 is computed at a corrected mass flow similar to case D (30% higher than Case A). Attenuation is further improved over Case 6 levels, demonstrating the trend that increased diffusion leads to improved attenuation in the impeller. Load fluctuates between 0.0 and 0.1 at mid chord, which is a 90% reduction over case 5 levels. The general trend that increased diffusion leads to improved attenuation is replicated with the isolated impeller calculation

The trend is further investigated by reducing the corrected mass flow from the case 5 level. Figure 5-8 shows the unsteady loading for case 8, which is computed at a corrected mass flow of 0.57, which is approximately 15% lower than case 5. This case shows a significant increase in unsteady loading over case 5. The strength of the disturbance increases in magnitude towards the leading edge. Dynamic loading in the forward 0.2-0.4 chord peaks at 1.5 dynamic heads, which is approximately twice that of case 5. This observation further supports the hypothesis that increased diffusion leads to stronger unsteadiness.

An additional calculation is performed to assess the effect of stage loading on the upstream attenuation of the pressure disturbance. Case 9 is computed at a mass flow of 1.0, which is approximately 12% higher than case 7. However, the inlet flow angle has

been decreased from 25° to 0°. Decreased inlet flow angle leads to increased relative velocity and thus similar diffusion to case 5.

Case 9 provides an additional check on the hypothesis by changing both corrected mass flow and loading. Figure 5-9 shows the unsteady loading for case 9. Note that the unsteadiness is stronger than case 7, despite the fact the corrected mass flow is higher. Mid-chord load fluctuates between 0.0 and 0.3, which is 3 times stronger than the loading of case 7. This calculation further demonstrates that stage loading is a controlling parameter that is responsible for changes in attenuation. In the next chapter, differences in loading are quantified in order to further support this inference.

5.2.4   Summary of Results

Figure 5-10 shows the variation of ΔLs with chordwise distance during one characteristic diffuser-passing period. This difference represents the strength of load fluctuations at a given location on the splitter blade. Comparison of cases 5, 6, and 7 demonstrate the observed trend that increasing corrected mass flow leads to increased attenuation. Results in this figure clearly show higher decay rate for case 7, which is at the highest corrected mass flow of the three. Inspection of case 8 shows an increase in load fluctuations as mass flow is reduced from the case 5 value of 0.69 to 0.57. Strong load fluctuations in excess of two dynamic heads can be seen near 40% chord.

The results of these five unsteady isolated impeller calculations support the hypothesis that increased corrected mass flow decreases the stage diffusion and leads to improved upstream attenuation of the loading disturbance. Comparisons of P_f contours between the 2D stage model and the isolated impeller model show that the levels of unsteadiness are similar when compared at similar mass flows. This supports the conclusion that throat geometry is not the controlling parameter, and in fact the change in corrected mass flow is responsible for the observed changes in attenuation. Comparison of the splitter blade loading also showed similar trends for attenuation when mass flow is varied.

Observations from this study show that the general trends from the coupled quasi-2D stage model are replicated with the isolated impeller model. In the next section, the

extent of upstream unsteadiness is characterized in terms of the DeHaller number for each case.

5.3 Impeller unsteadiness trend with the DeHaller number

L* is defined as the chord-wise distance from the impeller trailing edge where the fluctuations in unsteady loading have decayed to 50% of the initial disturbance strength. It is a metric for the attenuation of the unsteady loading disturbance imparted to the blade due to static pressure fluctuations in the impeller. Figure 5-11 provides an illustration to clarify the definition of L*. L* assumes a value of 0.8 for case 5, a value of 0.36 for case 6, and a value of 0.16 for case 7.

Figure 5-12 shows the variable L* plotted against DeHaller number for all the cases which have been examined. The chart includes the four unsteady calculations from chapter 4 (cases A-D) and the five calculations discussed in the present chapter (cases 5-9). Figure 5-12 serves to determine if there is a correlation between the attenuation of the unsteady disturbance (characterized by L*) and the impeller loading (characterized by DeHaller number).

The dashed line in Figure 5-12 represents calculations 5-8 presented in this chapter. The figure shows that for the two cases with the highest loading (lowest DeHaller number), L* is approximately .8. As DeHaller number is increased, L* is reduced, indicating improved attenuation of the unsteady disturbance. This trend has been qualitatively observed in previous sections, and this figure serves to quantify the trend that decreased diffusion associated with increased corrected mass flow is responsible for the improved attenuation in the unsteady load on the impeller blade.

The result for Case 9 is indicated in Figure 5-12. Case 9 uses a decreased inlet flow angle to match the 3D situation, as described in chapter 2. Case 9 has been implemented at a higher mass flow (1.0), but the overall diffusion is similar to Case 8 (both have a DeHaller number of approximately 0.7). Despite the fact that the overall diffusion is similar, the value of L* is only 0.35 for case 9, which is significantly lower than the L* of 0.8 observed in case 8. This result suggests that stage loading may not be the only parameter that sets the level of unsteady loading in a centrifugal stage.

The results from the coupled stage models are also shown in Figure 5-12. Cases A and B, which have a DeHaller number of approximately 0.8, have L* values of approximately 0.75. This result is in agreement with the isolated impeller result which had an L* of 0.8 at a similar DeHaller number. Case C, which has a DeHaller number of approximately 0.95, shows a strong decrease in attenuation. The general trend is similar to the isolated impeller results, but the change in attenuation is stronger for the coupled case (L* of 0.15 vs. 0.35). Case D, which has a DeHaller number of approximately 1.2 has an L* value of 0.15. This result is also in agreement with the isolated impeller case. Overall, these results show that the general trend of improved attenuation with decreased loading is consistent between the coupled model and the isolated impeller model. This supports the hypothesis that changes in stage loading, not changes in the throat geometry, are responsible for the improved attenuation of the unsteady loading on the impeller blade observed in the results presented in chapter 4.

5.4 Summary

This chapter presents results from an unsteady impeller model that accounted for the presence of a downstream diffuser via an unsteady static pressure boundary condition. The goal of the model is to determine if changes in corrected mass flow are responsible for the changes in attenuation of the static pressure disturbance observed in chapter 4.

The unsteady flowfield was calculated at five specific operating conditions, and the results have been interrogated to arrive at the following;

- The overall trend of impeller unsteady loading attenuation with respect to changes in corrected mass flow has been replicated by the 2D isolated impeller model
- Results with increase flow angle (increased Mach number) show improved attenuation at equivalent diffusion ratios

The implication of this result is:

- The driver responsible for the changes in attenuation is the decreased stage loading (characterized by the DeHaller number) associated with increased corrected mass flow, which is the hypothesis put forth in chapter 4.
- Stage loading may not be the only parameter that sets the level of attenuation in the impeller.

Impeller Pressure Ratio, 100% Speed
Quasi-2D Models
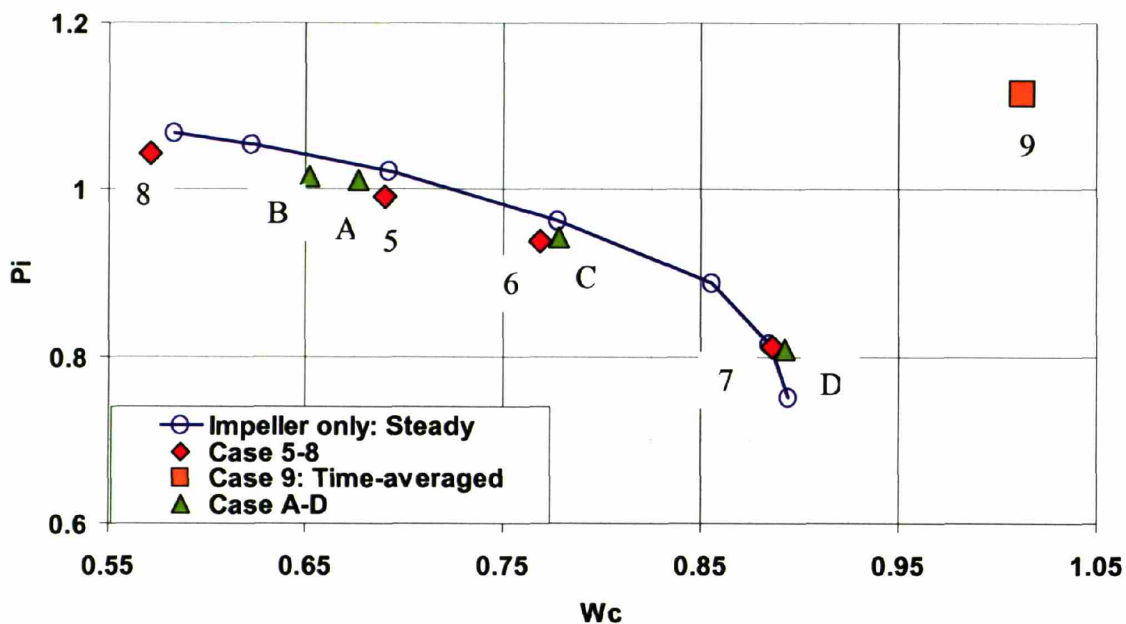
Figure 5-1 Computed impeller pressure ratio for quasi-2D cases, with closed symbols indicating time-averaged results

Impeller Efficiency, 100% Speed
Quasi-2D Models
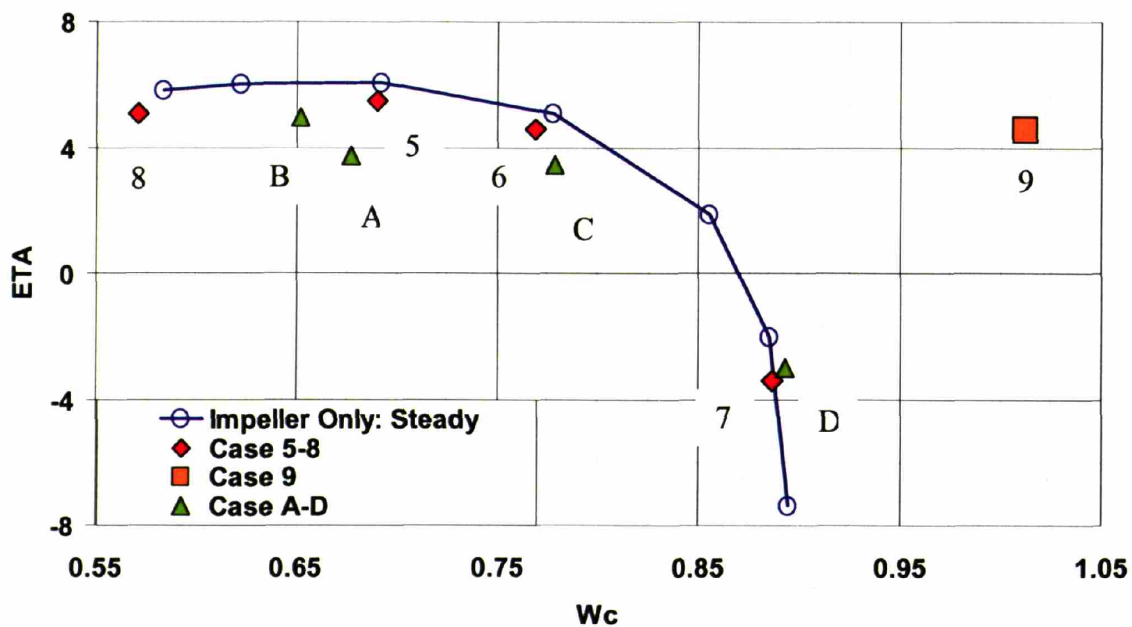
Figure 5-2 Computed impeller efficiency for quasi-2D cases
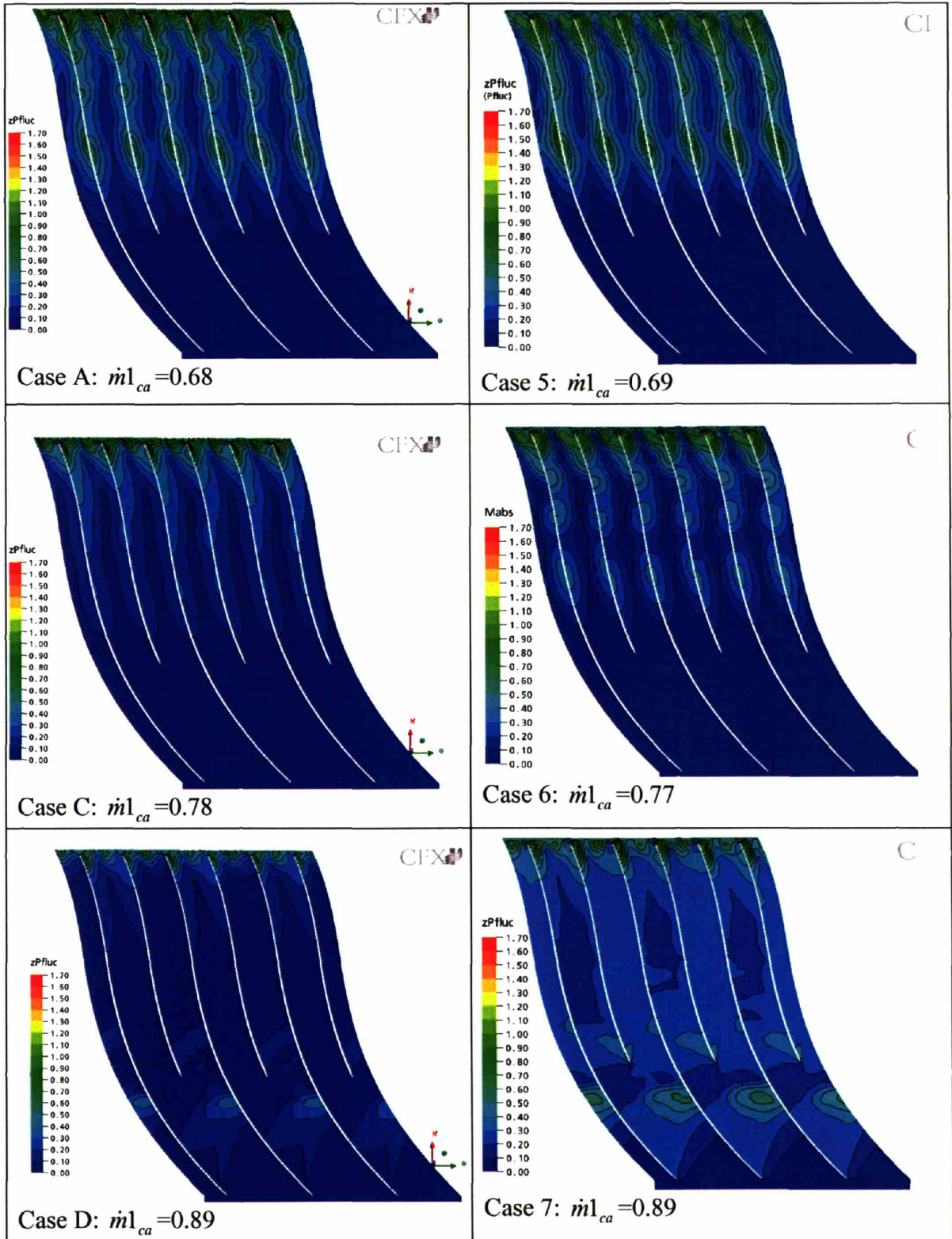
Figure 5-3 Contour of P_f for coupled quasi-2D model of centrifugal compressor (Case A, C, and D) to compare with those for the isolated impeller (Case 5,6,7) subjected downstream static pressure field.
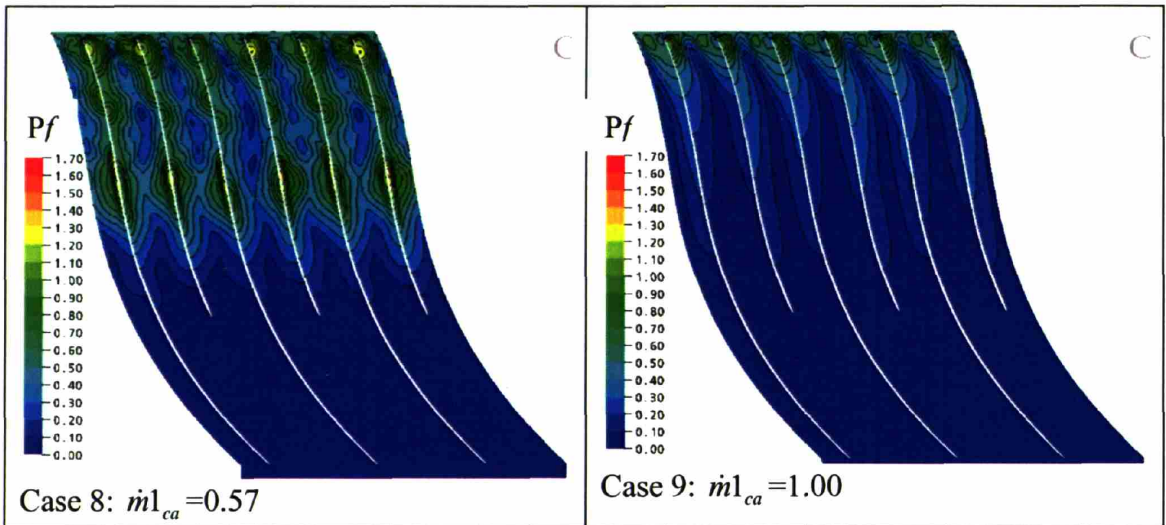
Figure 5-4 Contours of P$_f$ for cases 8 and 9, showing strong unsteadiness for case 8, which has decreased corrected mass flow relative to case A
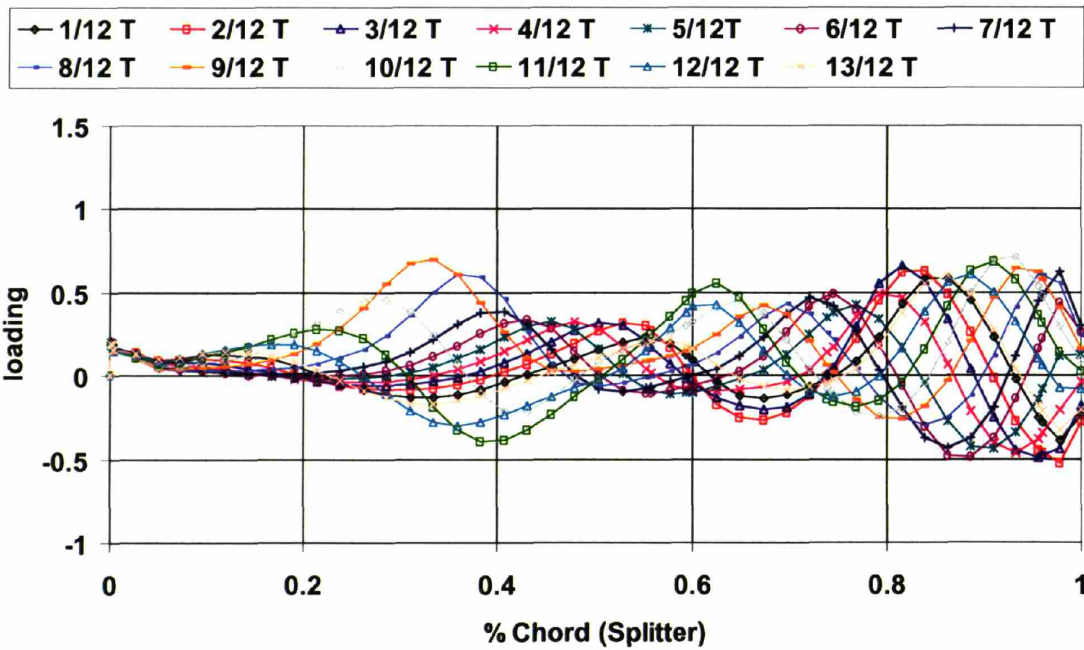
Figure 5-5 Chordwise loading distribution for case 5, showing strong fluctuations of unsteady load in the leading edge region

Unsteady Splitter Loading: 2D Isolated Impeller
Case 6
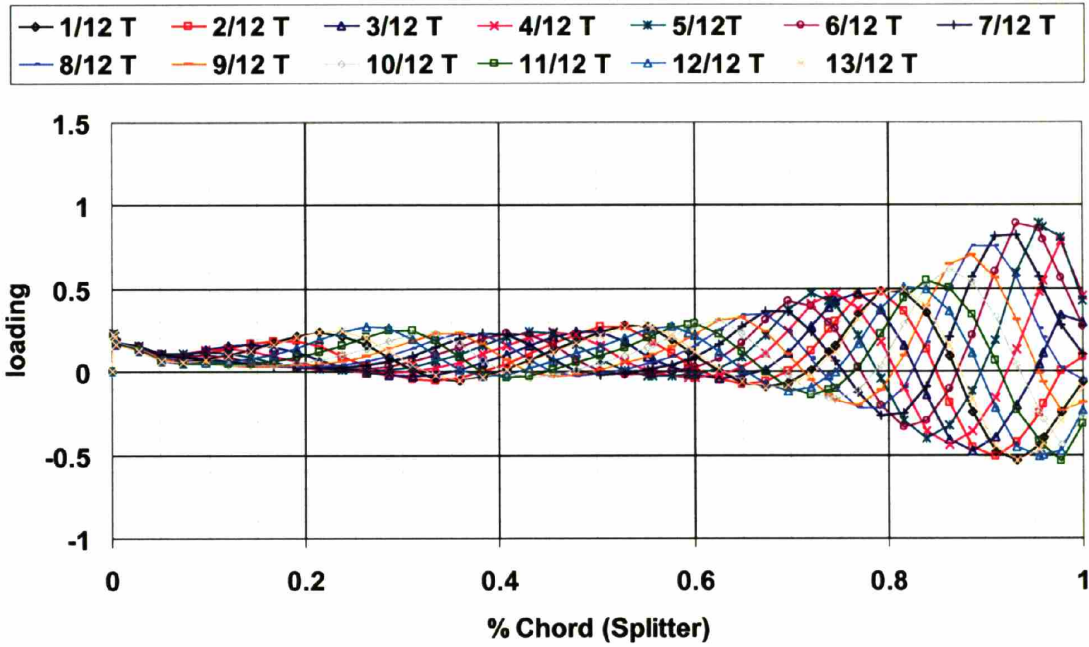
Figure 5-6 Chordwise loading distribution for case 6, showing moderate fluctuations of unsteady load in the leading edge region

Unsteady Splitter Loading: 2D Isolated Impeller
Case 7
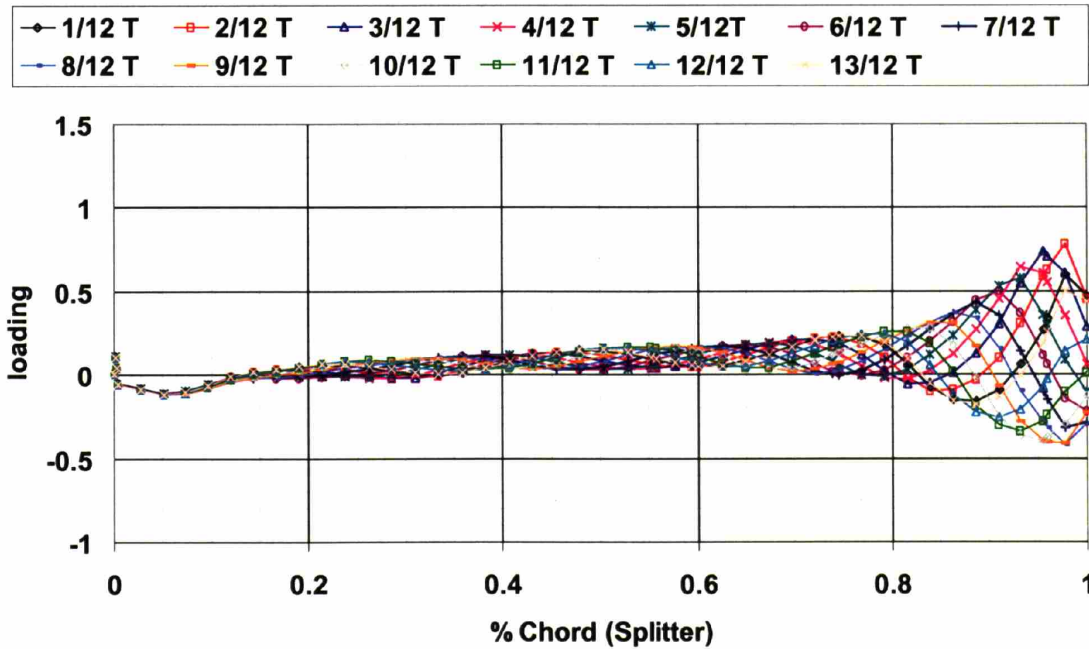
Figure 5-7 Chordwise loading distribution for case 7, showing small fluctuations of unsteady load in the leading edge region

111

Unsteady Splitter Loading: 2D Isolated Impeller
Case 8
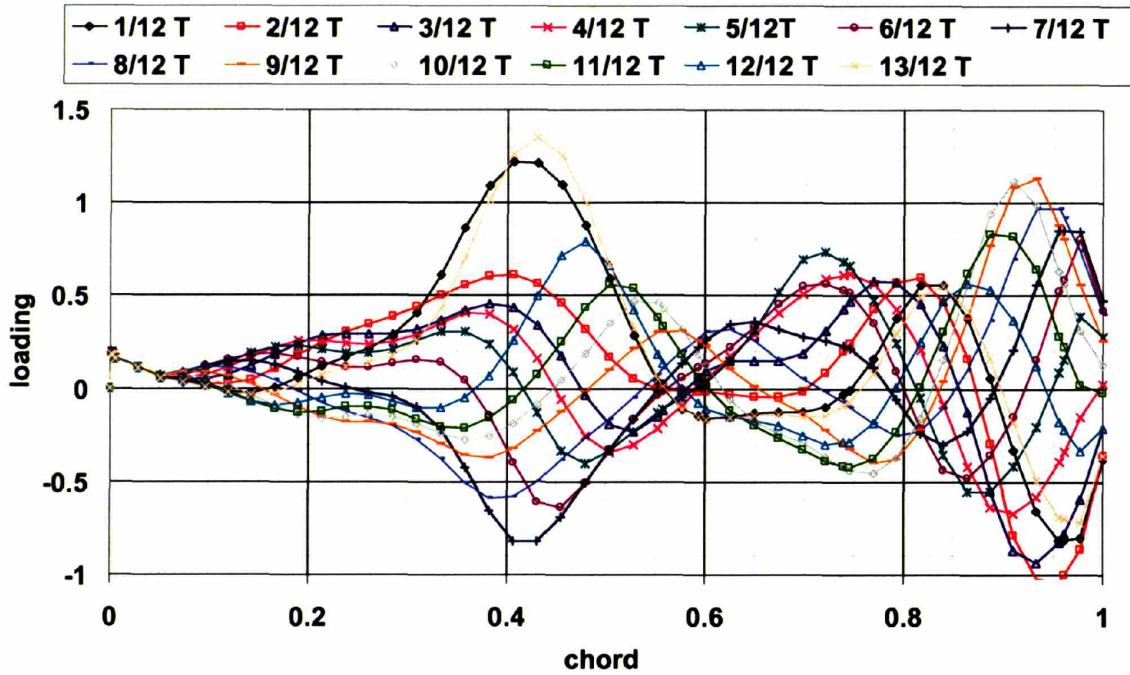
Figure 5-8 Chordwise loading distribution for case 8, showing increased fluctuations of unsteady load in the leading edge region, relative to case 5

Unsteady Splitter Loading: 2D Isolated Impeller
Case 9
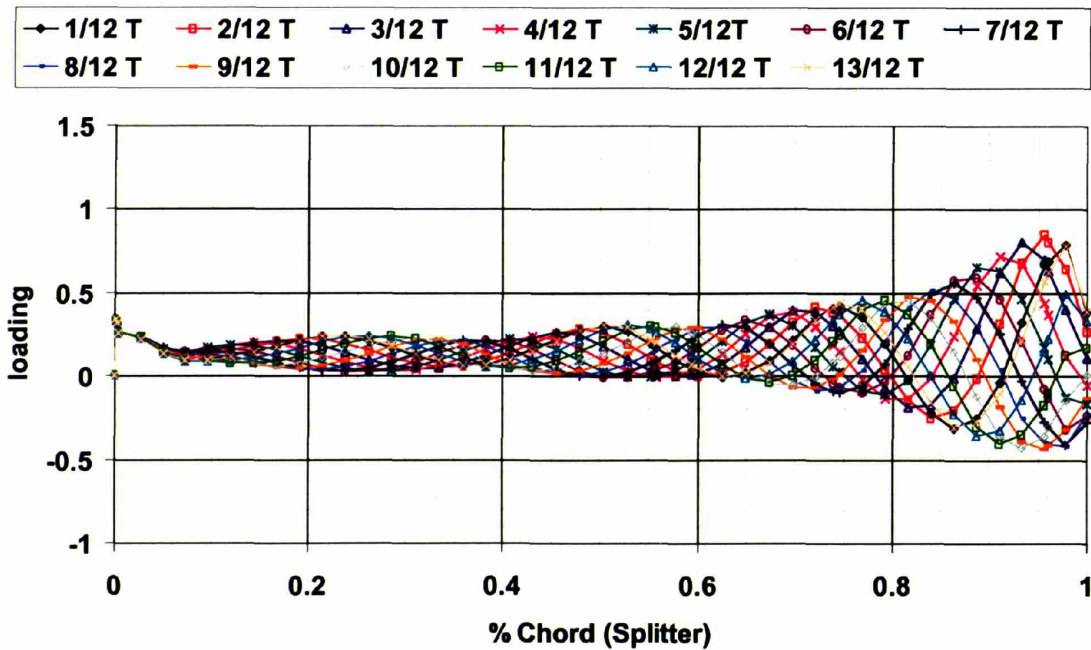
Figure 5-9 Chordwise loading distribution for case 9, showing moderate fluctuations of unsteady load in the leading edge region
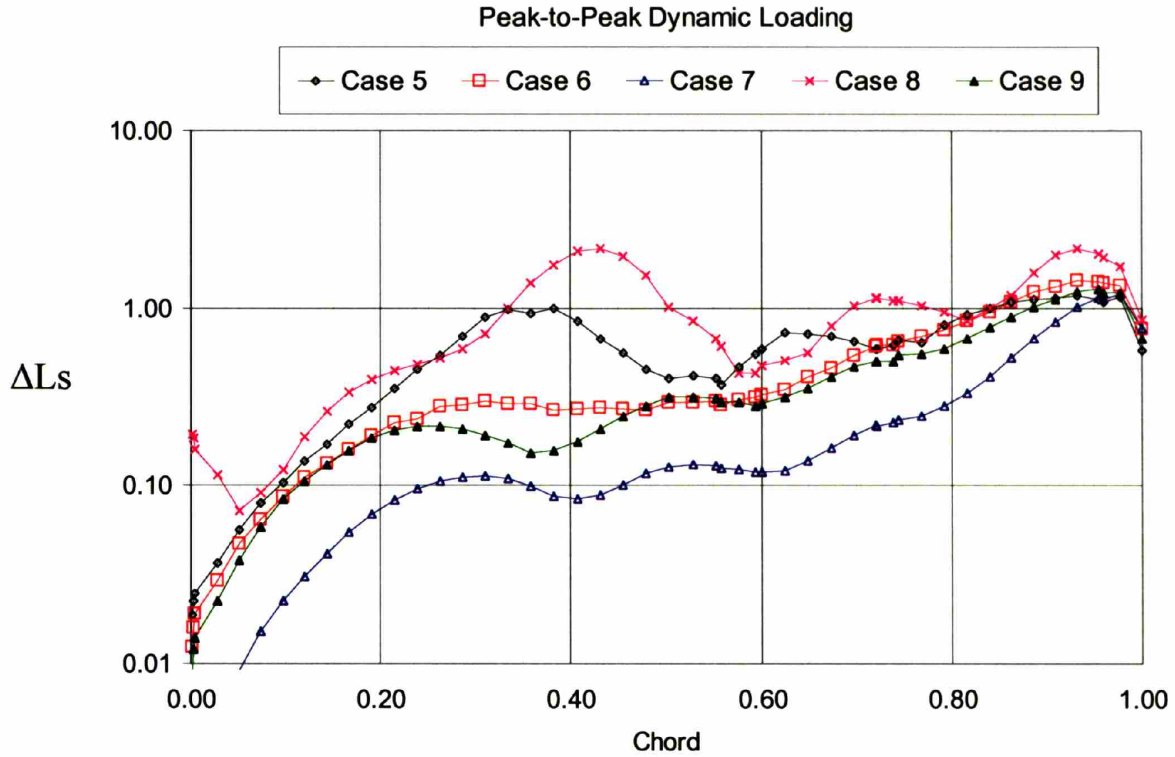
Figure 5-10 Strength of splitter blade loading fluctuations for cases 5-9
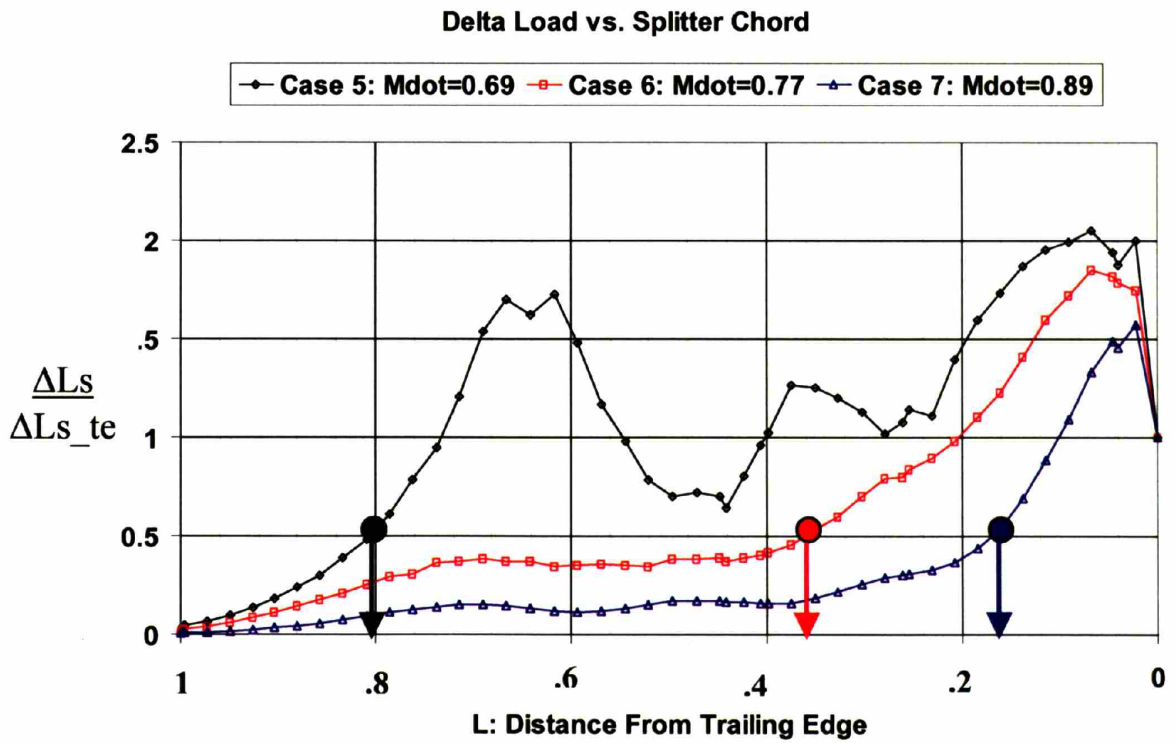
Figure 5-11 Strength of load fluctuations for cases 5-7 to illustrate the variable L*

113

L* vs. DeHaller Number
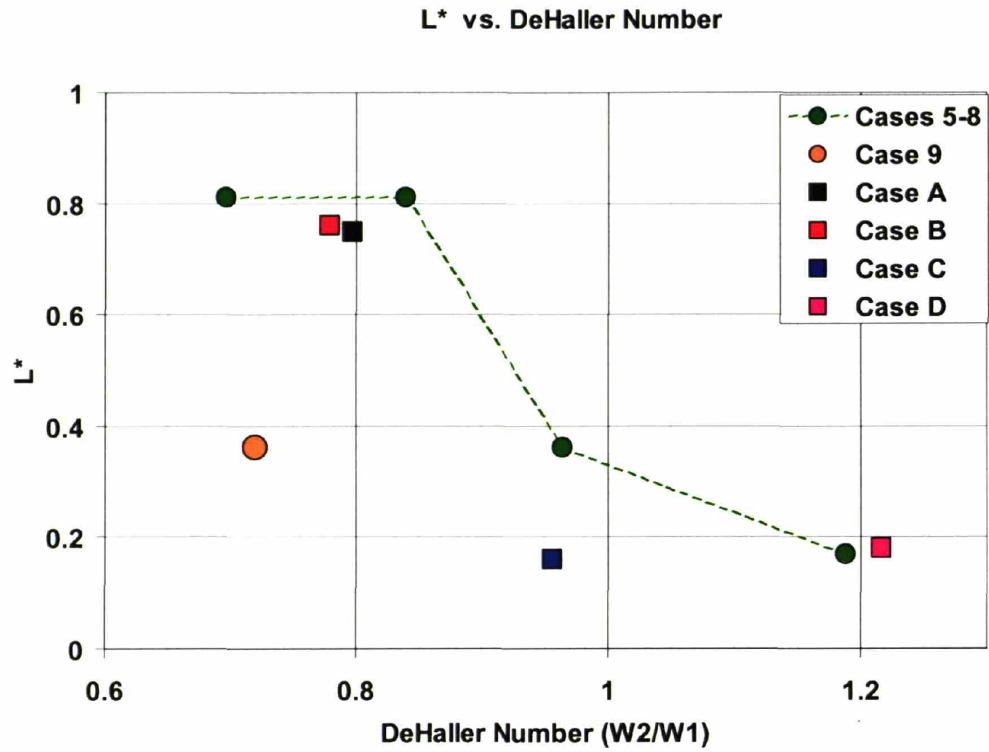
Figure 5-12 L* plotted vs. DeHaller Number, showing the trend that cases with low DeHaller number (increased diffusion) exhibit increased upstream unsteadiness

6. Results for the 3D Unsteady Stage Model

6.1 Introduction

This section presents the results for the 3D unsteady flow simulations in the centrifugal compressor stage. The results of the unsteady behavior at two corrected mass flows are interrogated. The flow results are assessed against the results from the 2D models to determine if the 2D approximation is adequate for capturing the important unsteady flow behavior. This serves to determine if the hypothesis developed in chapters 4 and 5 hold in the 3D flow situation.

6.2 Results of 3D calculation

6.2.1 Time-averaged operating conditions

Calculations 10 and 11 consist of two 3D unsteady calculations in which the normalized corrected mass flow per unit area is set to 1.05 and 1.10. Figure 6-1 shows the stage pressure ratio plotted against the inlet corrected mass flow, which includes the results from calculations 10 and 11. It shows that the time-averaged pressure ratio is close to that which has been calculated from the steady mixing plane model in chapter 2. At a corrected mass flow of 1.05, the calculated pressure ratio is almost identical. Figure 6-2 shows the stage efficiency. It also shows that time-averaged efficiency is close to that which has been calculated from the steady mixing plane model. Both figures show that the time-averaged stage performance is in accord with the measured stage performance. Near the design point, the computed stage pressure ratio is within 5% of the measured value, and stage efficiency is within 2 points of the measured value.

6.2.2 Source of Unsteadiness: Local static pressure variation

Before assessing the magnitude of the unsteady load acting on the splitter blade, it is of interest to first elucidate the source of unsteadiness, as was done in chapter 4. Figure 6-3 shows the time-averaged normalized static pressure distribution at mid-span in the impeller-diffuser interaction region for case 10. As in Figure 4-2, the letter "S" denotes the location of the splitter blade at each instant in time. Similar to the results shown in chapter 4, there is a strong circumferential static pressure gradient that is stationary in the absolute reference frame. The gradient is associated with the strong streamline curvature that occurs upstream of the diffuser passage. This is illustrated in Figure 6-4. Because this disturbance is fixed in the absolute reference frame, the impeller sees this as an unsteady disturbance.

At time t=5/12 τ, the splitter pressure surface is in front of the zone of high static pressure. At the next instant, 6/12 τ, the splitter is close to the region of high static pressure, and there is some increase in static pressure on the pressure surface. At time 7/12 τ, there is an increase in pressure to 1.6. Time 8/12 τ shows the highest level of static pressure (1.8), and also shows that the high static pressure disturbance has propagated upstream. Note at this instant the pressure on the suction surface is approximately 1.1. This leads to a high static pressure difference of 0.7. The next two instances in time further illustrate the propagation and decay of the static pressure disturbance as the impeller continues to rotate in time. Interrogation of the unsteady static pressure field illustrates that the static pressure disturbance associated with the diffuser vanes is responsible for the unsteady loads acting on the blade.

6.2.3 An assessment of unsteadiness in the impeller

Figure 6-5 shows contours of P_f for case 10 and case 11. The results show some higher levels of unsteadiness for case 10 that has a computed mass flow 5% lower than case 11. Case 10 has peak levels of 0.4 near 50% chord, while case 11 has levels of 0.2. Thus the magnitude of pressure unsteadiness for case 10 is twice that of case 11 which has a computed mass flow 5% greater that that of case 10.

116

The unsteady static pressure field on the blade surface is extracted to calculate the time-accurate loading on the blade. Figure 6-6 shows the unsteady blade loading for case 10, which has a computed normalized mass flow of 1.05. It shows peak load values of 0.7. It also shows that the loading disturbance imposed on the blade decays upstream, although the results indicate increased levels of unsteadiness in the first 20% of the splitter chord. Figure 6-7 shows the unsteady splitter loading for case 11, which has a computed normalized mass flow of 1.10. The peak values of unsteady loading are similar to that which have been observed in case 10. The decay of the disturbance does show differences relative to case 10. The loading fluctuations near the leading edge of the splitter are significantly reduced.

The observed reduction in leading edge unsteadiness is further elucidated in Figure 6-8, which shows the parameter ΔL_s in semi-log scale for the two cases. The trailing edge (0.8 thru 1.0 chord) shows similar strength of load fluctuations. However, at the leading edge there are clear differences. Case 10 has unsteady loading fluctuations of 0.2, while case 11 has values of 0.05. These results are similar to the observations seen in chapters 4 and 5. Cases with increased mass flow, and therefore decreased diffusion, exhibit stronger upstream attenuation of the unsteady loading disturbance.

As mentioned in chapter 1, there are two specific crossing which occur in the operating range, one of which (M6) exhibited high response. The impeller is at a similar operating condition for both crossings. Thus it can be assumed that the unsteady loading is the same for both cases. Figure 6-9 shows the unsteady loading at one instant in time along with the normalized mode shapes. It appears that the spatial distribution of the unsteady load is more in-line with the 6th mode shape at the trailing edge. It does not appear that the spatial distribution of the unsteady load is more in-line with the 6th mode than the 5th across the rest of the splitter surface. This does not provide a clear explanation of why the 6th mode exhibited high levels of vibration while the 5th mode did not.

The implication of these results is that there is a strong unsteady load present on the splitter blade, and these unsteady loads are the likely cause of the aeromechanics difficulty. Pressure loading fluctuation magnitudes of about one tip dynamic head are

117

present in the last 85% of the splitter chord. In addition, there is unsteady loading present in the leading edge of magnitude about a quarter of the tip dynamic head.

6.2.4 Summary of results

To summarize, the calculated time-averaged performance based on the 3D unsteady flow simulations is in accord with the measured rig data. The unsteady flowfield shows strong unsteady loading present at the splitter trailing edge, as well as unsteady fluctuations at the leading edge. These results indicate that the diffuser stimulus is the source for the strong unsteady loading.

6.3 Comparison of unsteady behavior between 3D case and 2D approximations

6.3.1 Comparison of peak unsteady load

Figure 6-10 shows the computed mass flow and impeller pressure ratio for cases A, 9, and 10. Note that the computed mass flow for case A is lower than that of cases 9 and 10, but that the impeller pressure ratio is similar. Comparison of the unsteady splitter loading between case 10 and case A (intended to simulate case 10) show significant differences, while comparison between case 9 and case 10 are in good agreement.

Figure 6-11 shows instantaneous splitter loading for case A, case 9 and case 10. Timesteps have been chosen so that the splitter is in an identical circumferential position relative to the diffuser static pressure disturbance. Several observations are made to determine whether the 2D approximation is adequate for capturing the unsteady load behaviors.

The peak value of the unsteady load is strongly over-predicted by case A. The computed peak strength of the unsteady load for case A is approximately 70% higher (1.1 vs. .65) than case 10. In contrast, case 9 has a computed peak strength of 0.8, which is within 15% of that from the 3D model case 10.

The results are further interrogated to identify the cause for the change in peak loading between cases A and case 10. First, because case 9 and case 10 are in accord, the 2D approximation is eliminated as a source for this difference. The underlying reason is that any difference due to 3D effects would have been present in case 9, which they were not. Table 6-1 shows the calculated mass flow, DeHaller number, and flow angle for the three cases. One significant difference in the value for α_2, the impeller exit absolute flow angle. The flow angle in case A in almost 6° greater than that of cases 9 and 10. Previous work by Phillips indicates that diffuser is sensitive to inlet flow alignment [18]. This is elucidated in Figure 6-12 that shows time-averaged static pressure at the diffuser inlet plane for cases A and 10. It shows that case A, which has increased flow angle relative to case 10, has a stronger circumferential static pressure distribution. The interrogation of the flow results indicates that a change in diffuser inlet angle may be the source of the computed difference in peak dynamic load acting on the splitter blade between case A and case 10.

Case	A	9	10
$\overline{\dot{m}}_{ca}$	0.68	1.00	1.05
DeHaller	0.8	0.72	0.62
α_1	36.5	0.0	0.0
β_1	-0.5	0.0	-1.0
α_2	-5.6	-0.8	0.0

Table 6-1Comparison of flow angles for Case A, Case9, and Case 10

6.3.2 Comparison of spatial distribution of unsteady load

The second major difference is the spatial distribution of blade loading. The likelihood for strong vibratory response is high when the spatial distribution of blade loading coincides with the structural mode shape for a given frequency crossing. Figure 6-11 shows that case A has three distinct load "peaks" along the chord, while case 10 has four. In contrast, case 9 shows a spatial distribution very similar to case 10. Although the alignment of the load peaks may be somewhat different, both results show four distinct loading peaks.

Interrogation of the flow results is performed to identify the likely source of this difference between case A and case 10. Figure 6-13 shows the time-averaged and mass-flow averaged relative Mach number along the impeller mid-span. It shows that case A, which is at a lower corrected mass flow than cases 9 and 10, has significantly lower Mach numbers. A simple analysis of the disturbance wavelength is invoked to illustrate the effect of relative Mach number on the spatial distribution of blade loading.

The frequency of the disturbance imposed on the impeller is related to the rotational speed of the rotor and the number of stationary vanes,

$$\omega = N_d \Omega \qquad \qquad \text{(eq 6.1)}$$

where N_d is the number of stationary vanes and Ω is the rotational speed in revolutions per second. The speed at which the disturbance propagates upstream in the rotor can be expressed by the relationship for an acoustic wave in a moving media

$$c = a_0 - w \qquad\qquad \text{(eq 6.2)}$$

where c is the speed of propagation, a_0 is the local speed of sound, and w is the local velocity. The wavelength of the disturbance in the rotor frame can be approximated using

$$\lambda = c / \omega \qquad\qquad \text{(eq 6.3)}$$

and using the definition of relative Mach number

$$M_{rel} = w / a_0 \qquad\qquad \text{(eq 6.4)}$$

to arrive at

$$\lambda = \frac{a_0(1 - M_{rel})}{N_d \Omega} \qquad\qquad \text{(eq 6.5)}$$

Thus the number of peaks in the spatial loading distribution is estimated to be Lc/λ to arrive at

$$\# peaks = \frac{N \Omega L c}{a_0(1 - M_{rel})} \qquad\qquad \text{(eq 6.6)}$$

The ratio of peaks between case A and case 10 can be expressed by

$$Peak\ Ratio = \frac{(1 - M_{rel A})}{(1 - M_{rel 10})} \qquad\qquad \text{(eq 6.7)}$$

121

and this value is equal to .78, which is close to the ratio .75 (or ¾) observed in the results. The implication of this result is that the relative Mach number is a parameter that sets the spatial distribution of the unsteady loading along the chord.

The effect of Mach number is further elucidated in Figure 6-14. It shows the time-averaged relative Mach number and the quantity P_s' for cases A and 10, where P_s' is defined as

$$P_s' = P_n - \overline{P_n} \qquad\qquad (eq\ 6.8)$$

The quantity P_s' is the local static pressure relative to the time-averaged static pressure, and can be thought of as viewing the unsteady portion of the time-accurate flow field. This figure shows case A has lower relative Mach numbers throughout the blade row. Inspection of the P_s' field at one instant in time shows that there are three distinct regions where static pressure is above the average value. This leads to the three distinct loading peaks observed in Figure 6-11. By comparison, case 10, which has higher Mach numbers, exhibits four peaks.

6.3.3   Comparison of the upstream extent of the unsteady load

The upstream extent of the unsteady loading is illustrated in Figure 6-15, which shows the variable ΔLs along the splitter chord for all three cases. In the 0.6 to 1.0 chord region, cases A and 9 replicate the decay rate of the initial disturbance as predicted by the 3D model, case 10. In the 0.2 to 0.4 chord region, the loading fluctuation predicted in case A is almost 1 order-of-magnitude stronger than case 10, while case 9 is only slightly stronger than case 10. Clearly, the 2D coupled case severely over predicts the levels of unsteadiness in the blade row. The source of this difference is not currently known.

6.3.4   Summary of comparisons between quasi-2D and 3D results

The implication of these results is that the 2D uncoupled model is an adequate approximation for the unsteady flow in the impeller. The 2D uncoupled model captures three particular unsteady characteristics present in the 3D model: Peak magnitude of the unsteady load, spatial distribution of the unsteady load, and decay of the unsteady loading disturbance. An additional implication is that the 2D coupled model is shown to be an inadequate approximation for the unsteady flow. This is driven by the fact that the correct mass flow per-unit-area can not be replicated in the 2D coupled model due to the 3D diffuser geometry.

6.4 Summary

The results of the 3D unsteady calculation have been interrogated to arrive at the following key results:

- The downstream diffuser is a source for strong unsteady loading on the splitter blade
- Results of a quasi-2D model agree with the calculated 3D unsteady loading characteristics: Peak loading, spatial distribution, and upstream attenuation.

The implication of these results is as follows:

- A quasi-2D isolated impeller model which models the diffuser as a moving static pressure wave is an adequate model of the full centrifugal stage
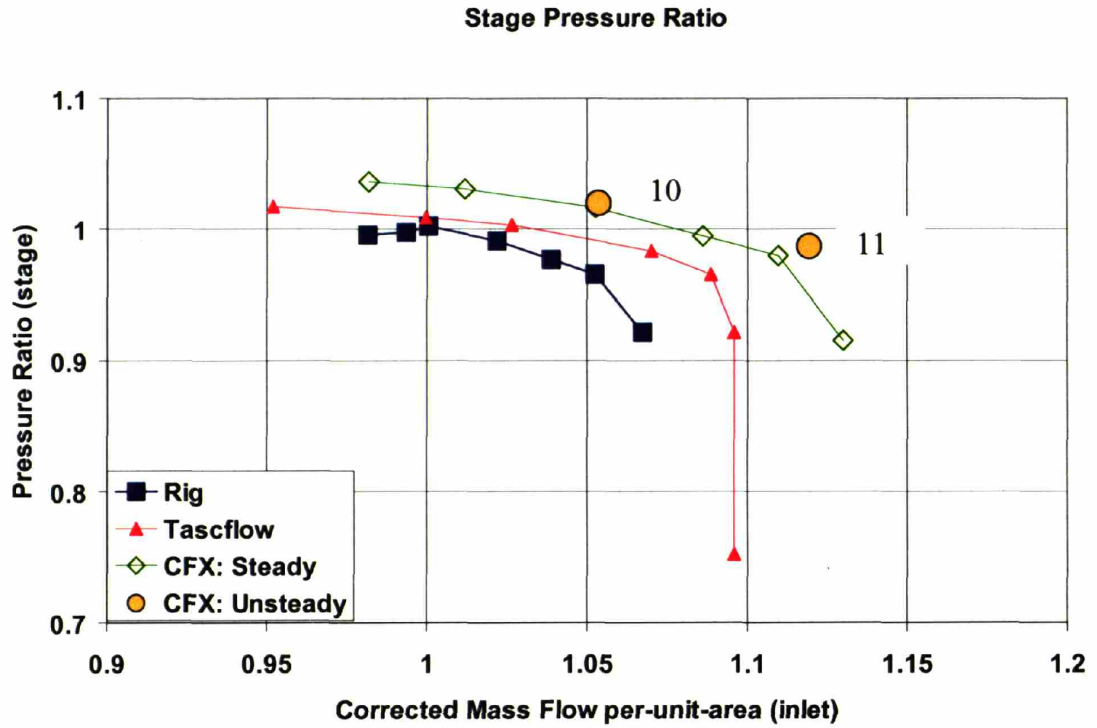
Stage Pressure Ratio

Figure 6-1 CFX computed stage pressure ratio, showing reasonable agreement between experiment and time-averaged calculations
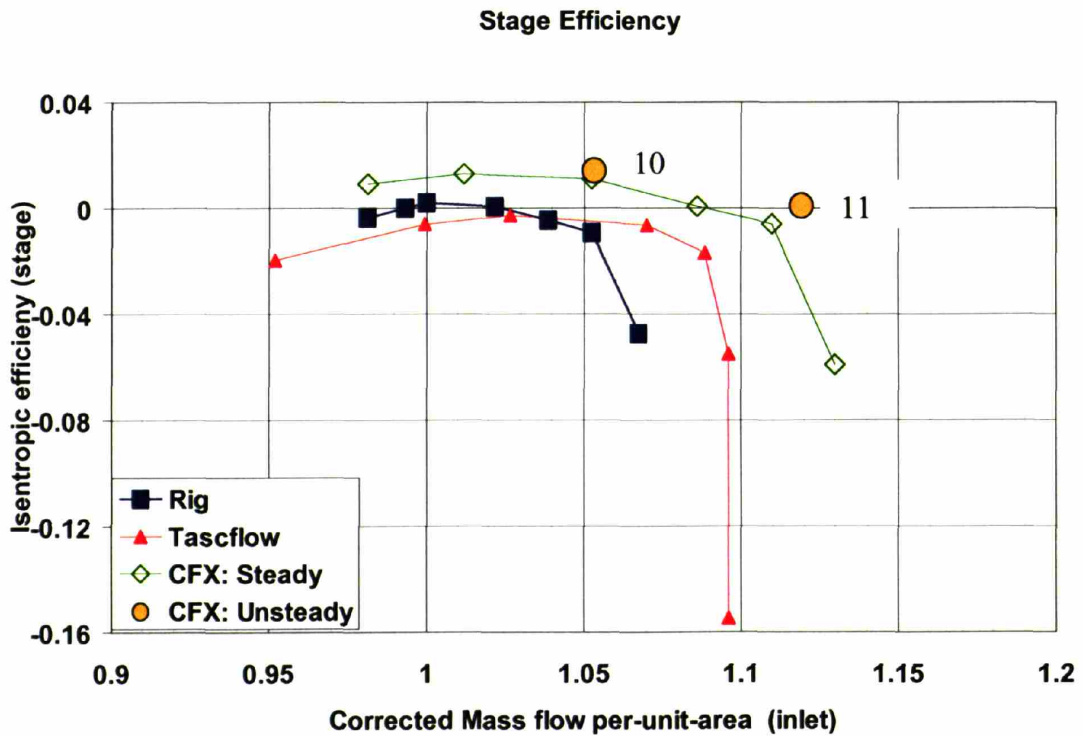
Stage Efficiency
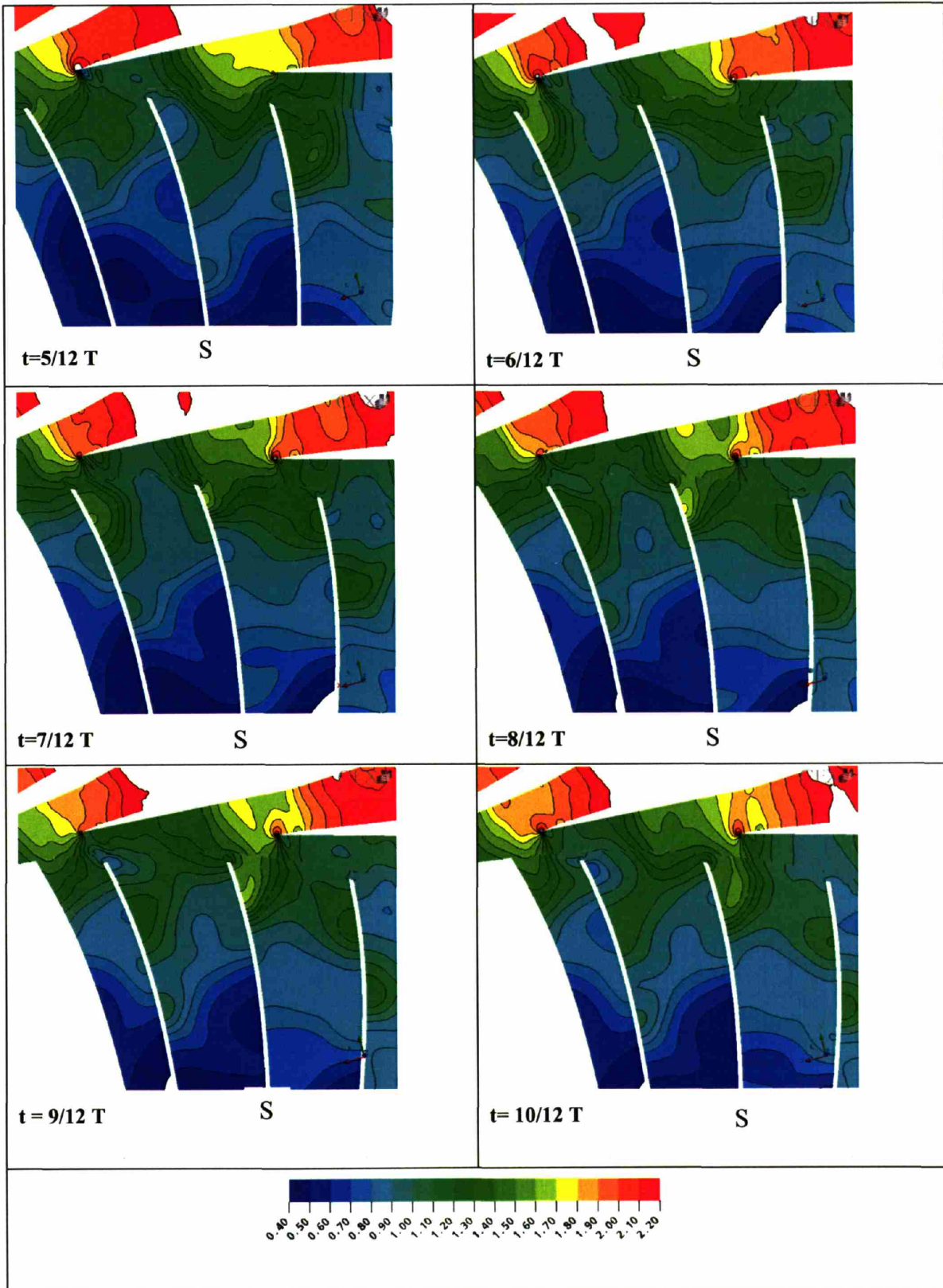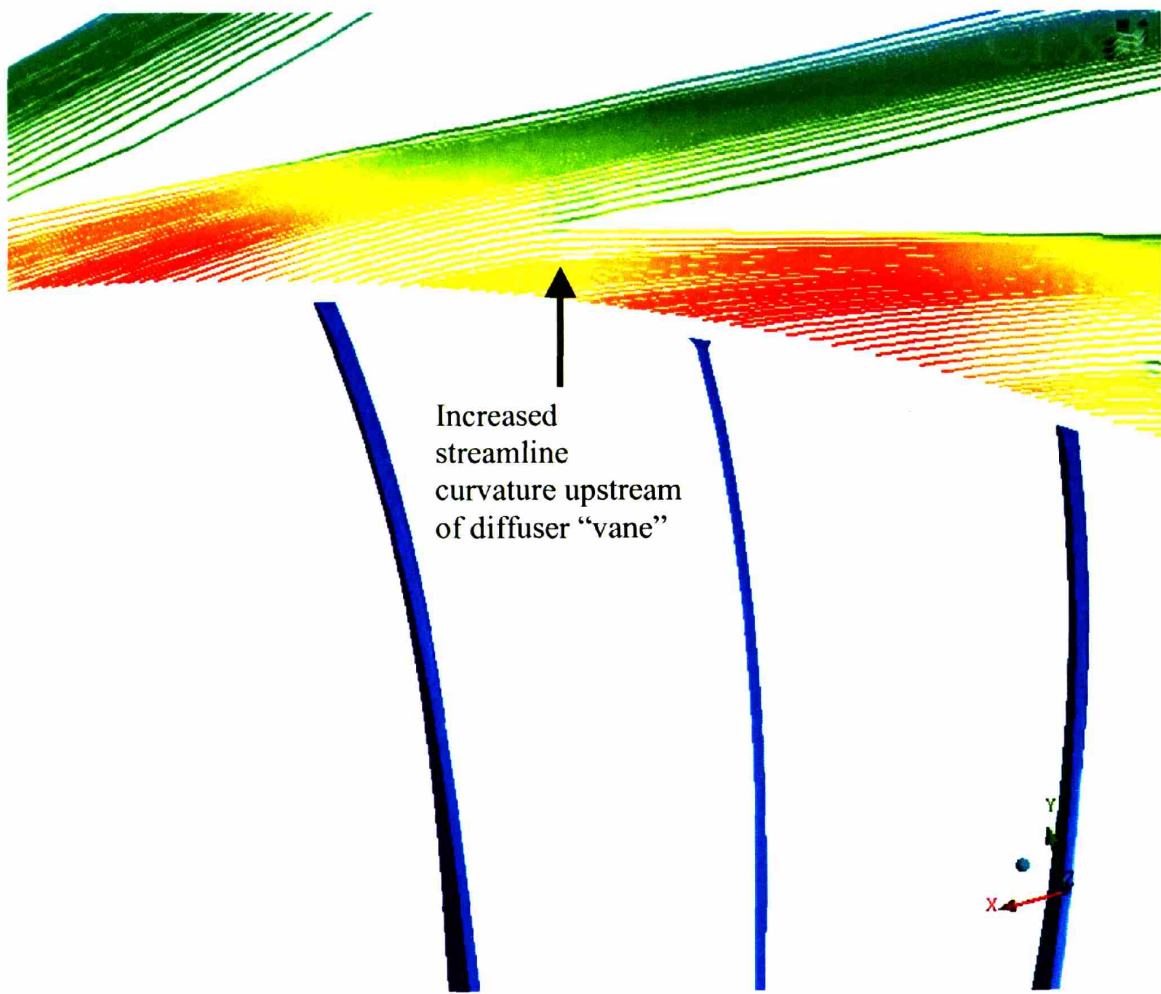

Figure 6-2 CFX computed stage efficiency, showing reasonable agreement between experiment and time-averaged calculations

124

t=5/12 T   S

t=6/12 T   S

t=7/12 T   S

t=8/12 T   S

t = 9/12 T   S

t= 10/12 T   S

0.40 0.50 0.60 0.70 0.80 0.90 1.00 1.10 1.20 1.30 1.40 1.50 1.60 1.70 1.80 1.90 2.00 2.10 2.20

Figure 6-3 Static pressure distribution for 6 instants during ½ diffuser passing period

Increased
streamline
curvature upstream
of diffuser "vane"

Figure 6-4 Flow streamlines (based on time-averaged velocity) in the diffuser entrance region
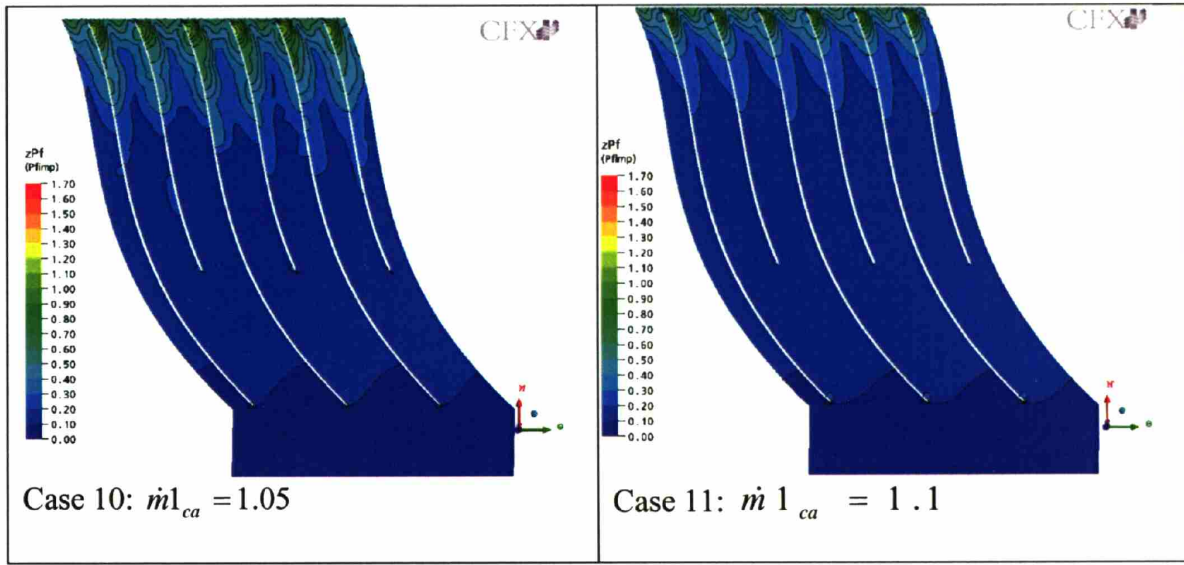
Figure 6-5 Contours of P_f for Cases 10 and Case 11, showing moderate levels of unsteadiness in case 10, and decreased levels of unsteadiness in case 11
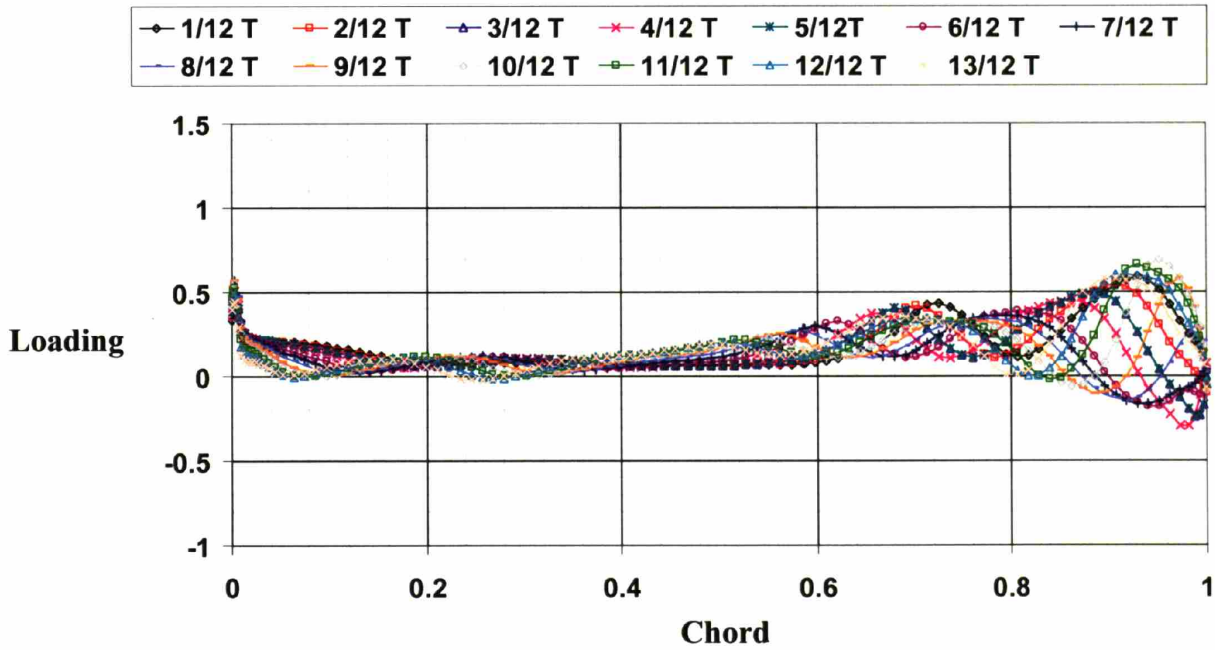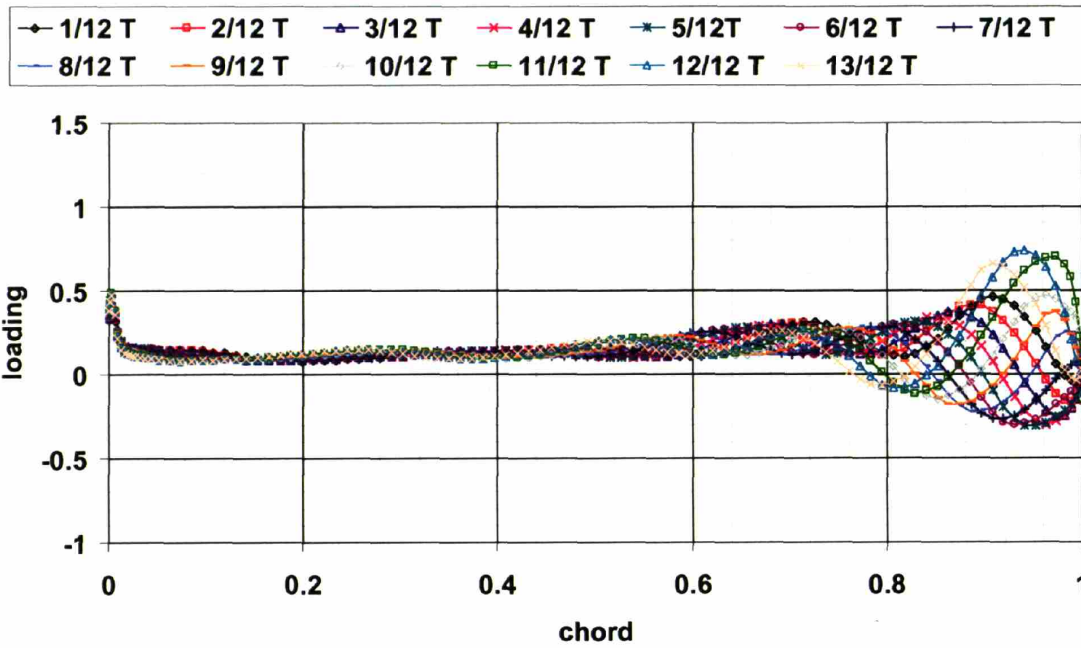

Figure 6-6 Chordwise loading distribution for case 10, showing strong loading fluctuations at trailing edge. Moderate levels of unsteady load fluctuations can also be observed in the leading edge region

Splitter Loading: 50% Span
Case 11: Mdot=1.10

Figure 6-7 Chordwise loading distribution for case 11, showing strong loading fluctuations at trailing edge, and negligible load fluctuations near the leading edge

Loading Fluctuations: Cases 10 and 11
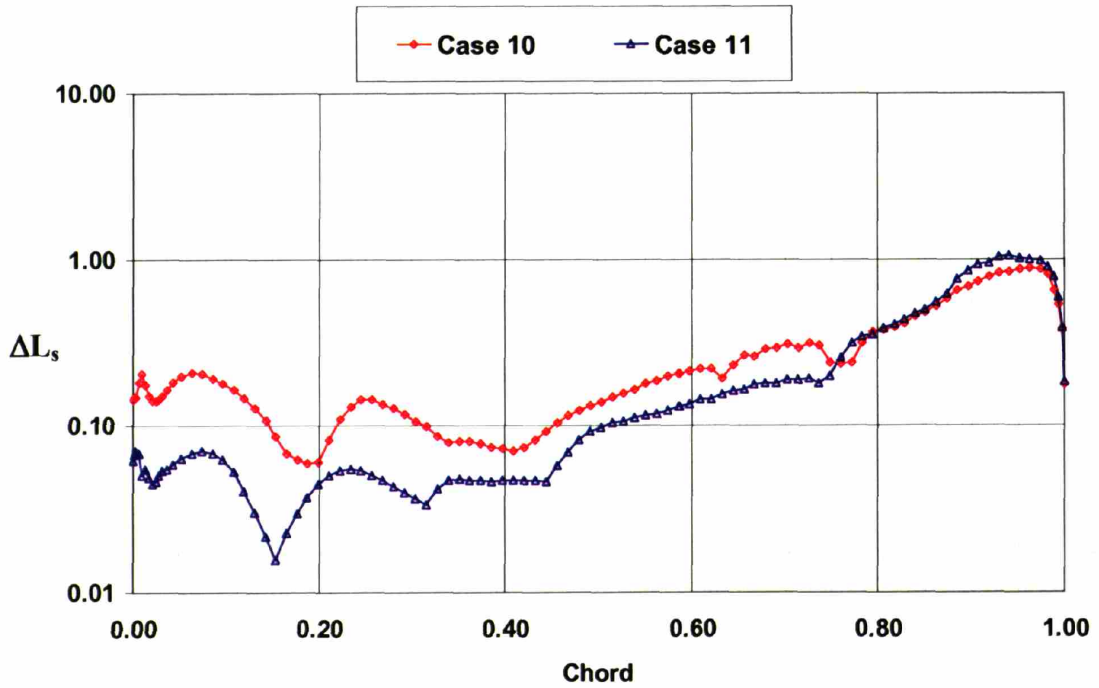
Figure 6-8 Strength of unsteady loading fluctuations for cases 10 and 11, showing stronger levels of unsteady loading in the leading edge region for case 10
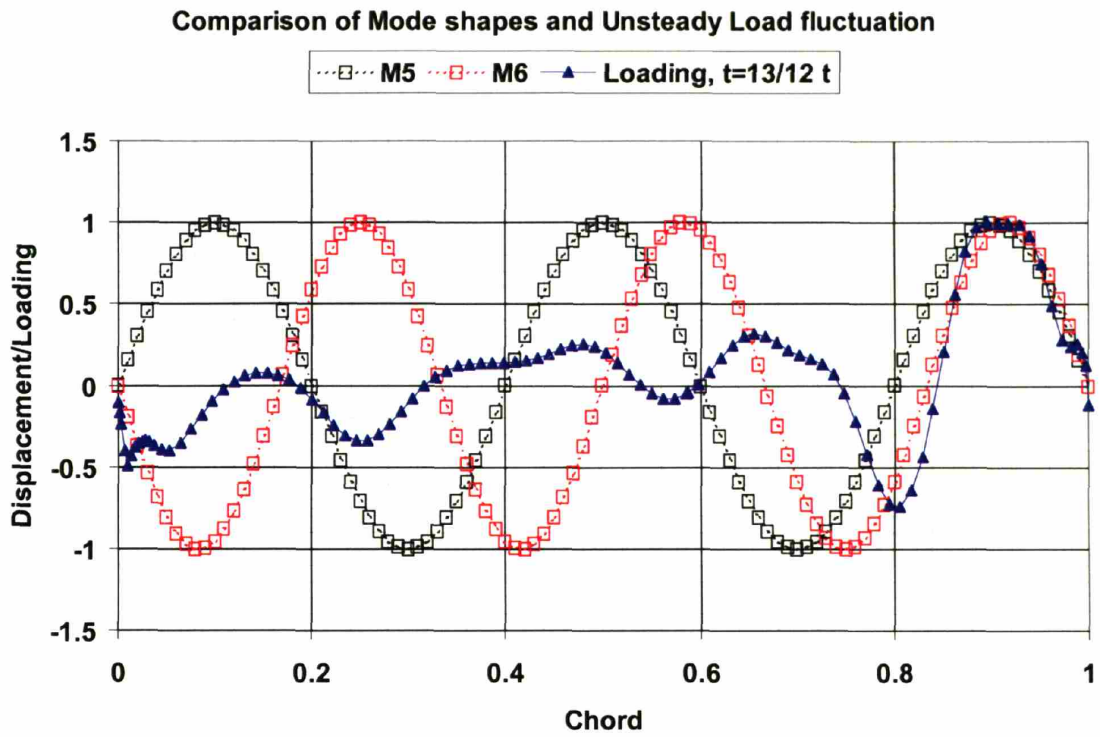
Comparison of Mode shapes and Unsteady Load fluctuation

···▣··· **M5** ···▣··· **M6** —▲— **Loading, t=13/12 t**

Figure 6-9 Comparison of mode shapes and load fluctuation

Impeller Pressure ratio vs. Mass Flow: 100% Corrected Speed

—▫— **2D, mod alp1** —▲— **3D** —○— **2D, original alp1** ■ **Case A** ▲ **Case 10** ● **Case 5**

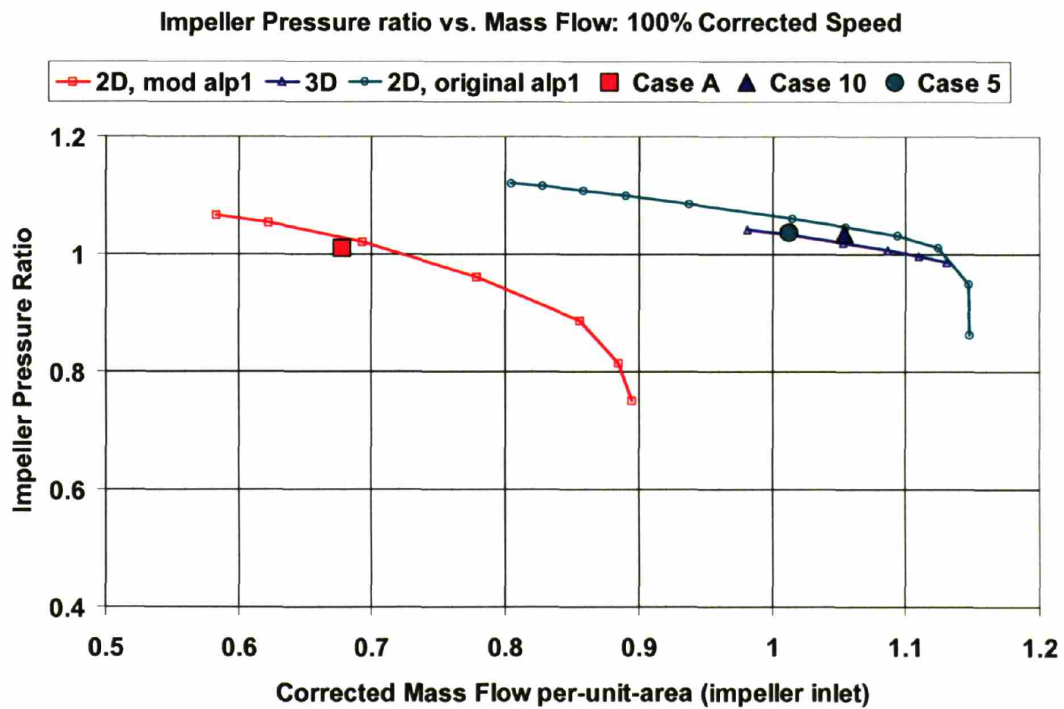**Figure 6-10 Impeller pressure ratio for cases A, 5, and 10, showing that the impeller pressure ratio is similar for all three cases**
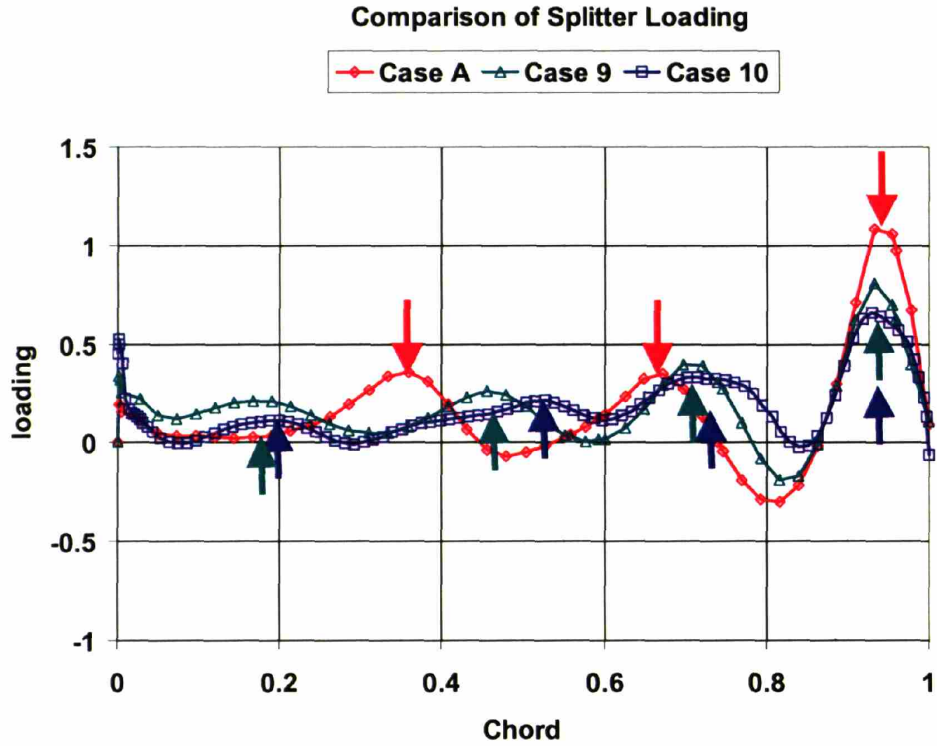
Comparison of Splitter Loading

Figure 6-11 Comparison of splitter unsteady loading between cases A, 9, and 10, showing that case A has three distinct peaks while case 9 (2D isolated impeller) and case 10 (3D) have four
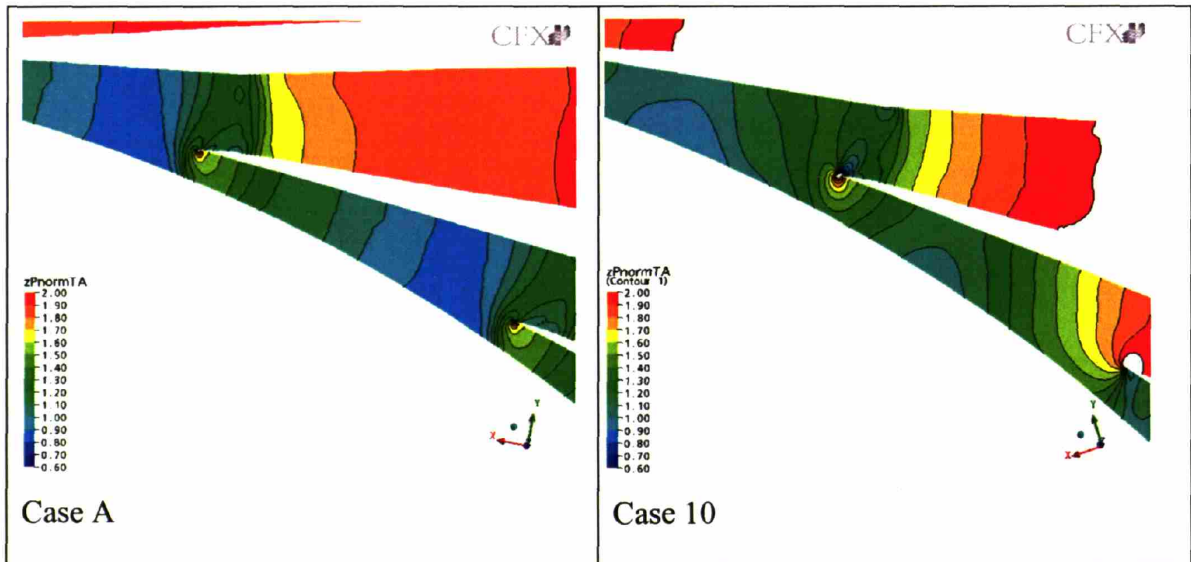

Figure 6-12 Comparison of time-averaged diffuser static pressure distribution, showing the difference between case A (2D stage model) and case 10 (3D stage model)

Comparison of time-averaged relative Mach number

Case A Case 10 Case 9

S/Sref
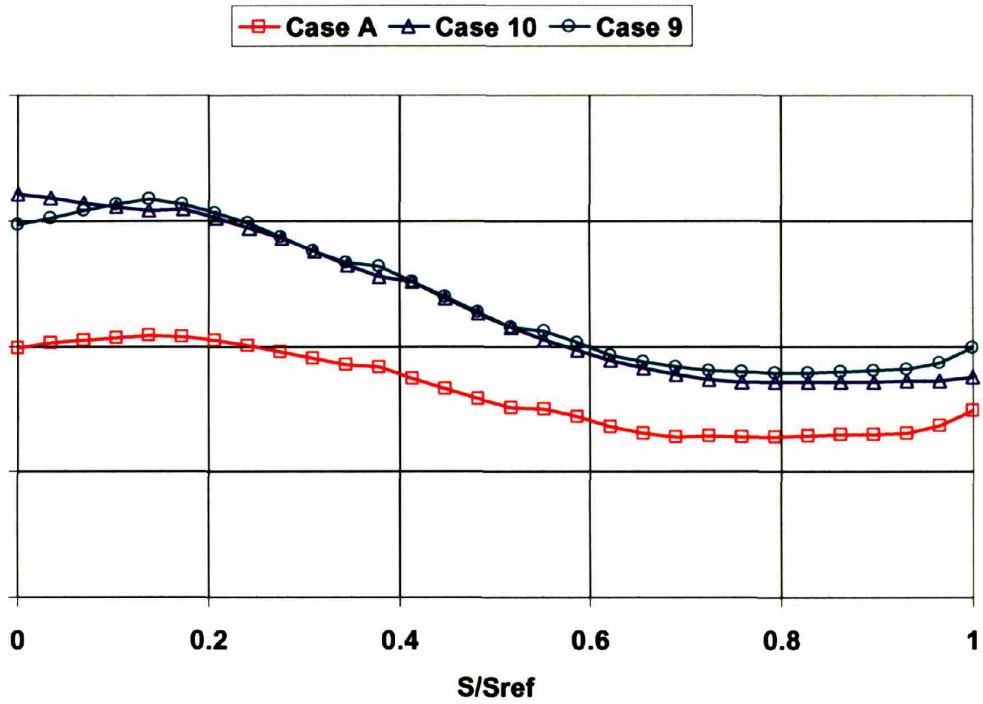
Figure 6-13 Time-averaged and area-averaged relative Mach number along impeller flowpath showing lower Mach numbers for Case A.
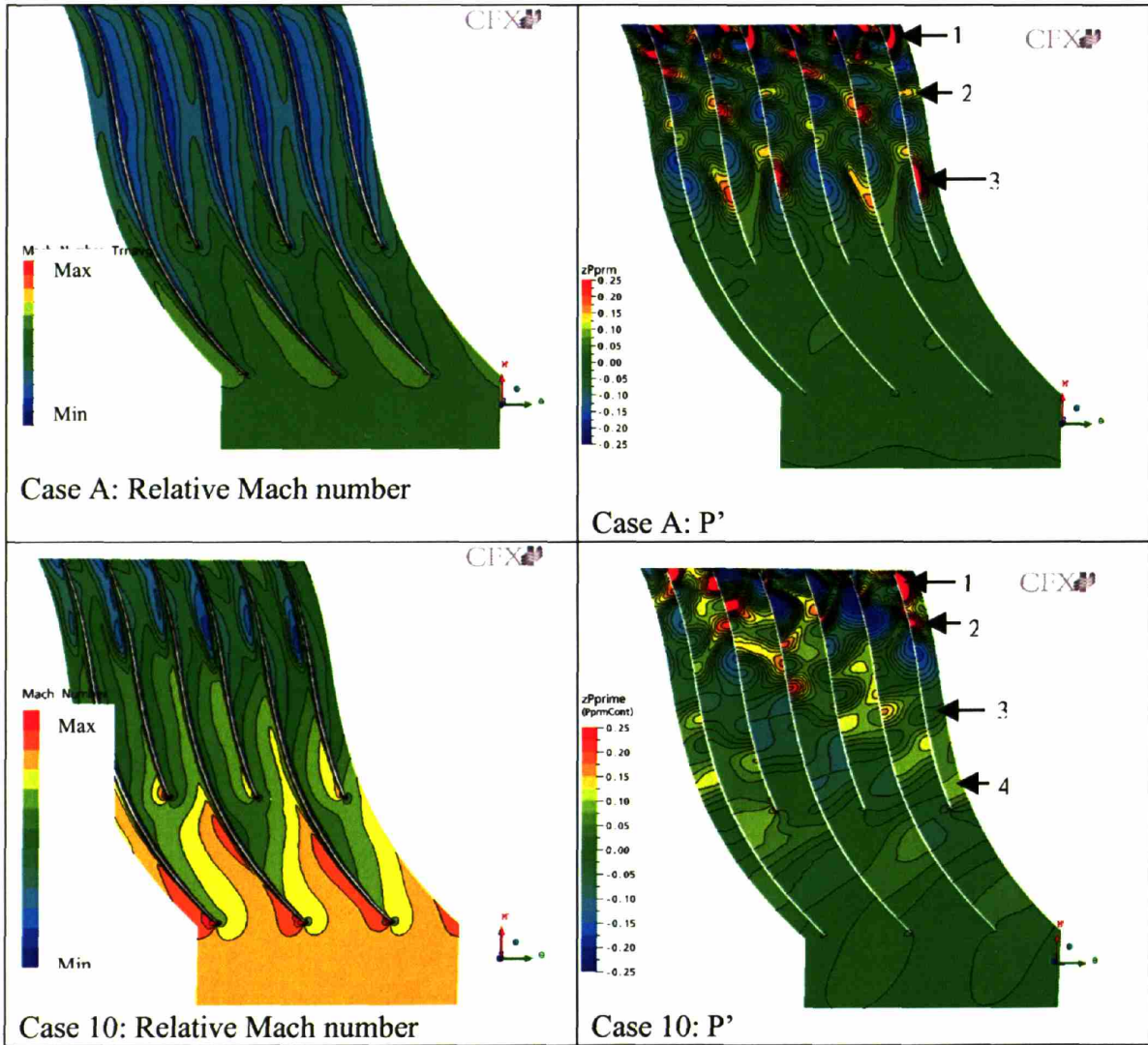
Figure 6-14 Contours of Mach number and P', showing the effect of mean flow Mach number on the spatial distribution of the static pressure disturbance. The higher Mach number in case 10 decreases the speed of the upstream traveling disturbance, thus increasing the number of peaks per splitter chord.

Figure 6-15 Comparison of splitter loading fluctuation between Case A and Case 10

7. Summary and Conclusions

7.1 Summary

A computational investigation of a modern centrifugal compressor stage is undertaken in order to characterize the unsteady flow processes that control the le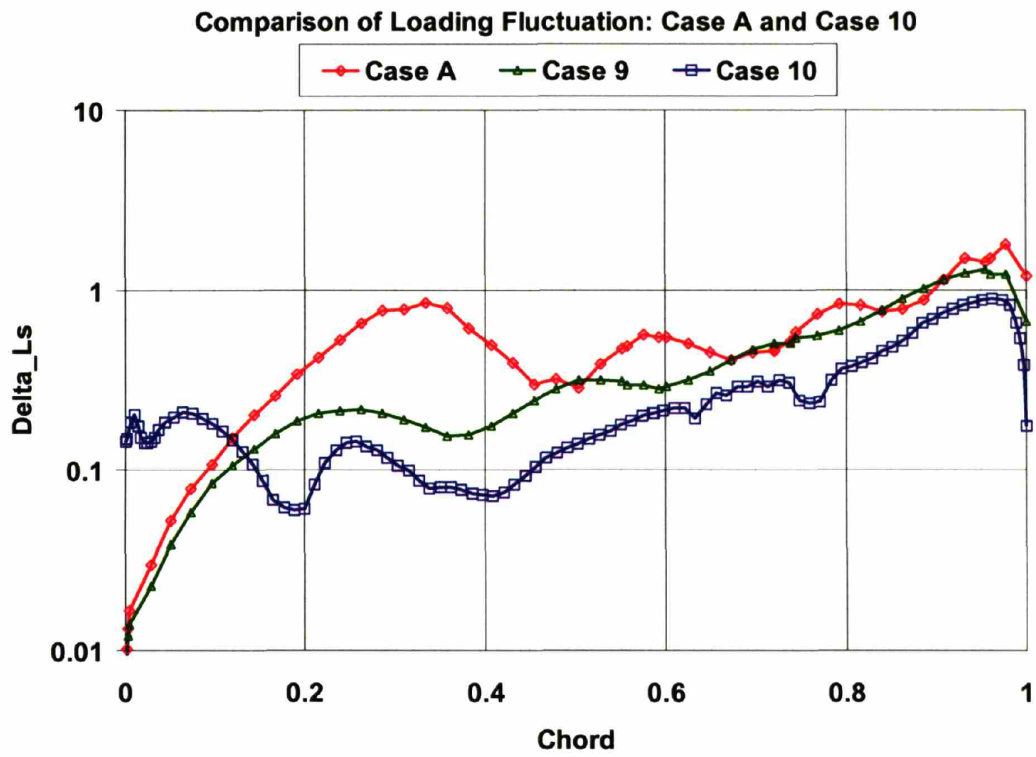vel and the extent of unsteady loading on the rotating impeller blades. The source of the unsteady loading, mainly the interaction between the diffuser static pressure disturbance and the rotating impeller is shown to be a cause of the aeromechanics difficulty experienced on this machine. Computations are implemented in order to quantify the changes in splitter loading due to changes in impeller-diffuser gap, stage loading, and relative Mach number.

7.2 Conclusions

(1) There can be an upstream manifestation of a downstream stimulus for a centrifugal compressor stage with a Mod-2 diffuser. The upstream manifestation is considerable unsteady loading in the splitter blade leading edge while the downstream stimulus is the unsteady interaction between the rotating impeller and the stationary downstream diffuser

(2) The three key controlling parameters that set the level and upstream extent of the unsteady blade loading are impeller-diffuser gap, stage loading (characterized by the DeHaller number), and relative Mach number. The impeller-diffuser gap sets the strength of the unsteady loading while the DeHaller number sets the extent of the upstream manifestation of unsteady loading.

(3) A quasi two-dimensional model in which an unsteady pressure boundary condition is imposed at the impeller exit is used to approximate the presence of a downstream diffuser. The results of the unsteady loading from this model is shown to yield unsteady splitter blade loading that is in accord with that which has been calculated by the three-dimensional unsteady stage model.

(4) The effect of time-averaging unsteady inlet conditions does not lead to an over-prediction in maximum flow capacity for a fluid device. However, time-averaging of the inlet conditions can lead to over-predictions of mass flow for a device which has a time-average pressure ratio that is below that for choked flow.

7.3 Recommendations for future work

There are several issues that have not been resolved by this research, and they are as follows:

- The process responsible for the observed difference in vibratory response between the 5th and 6th mode is not identified
- A rigorous explanation of how stage diffusion effects the upstream influence of the static pressure disturbance in not provided
- The observed trends of upstream influence with stage loading and relative Mach number are not demonstrated based on physical experiments.

The following research tasks are recommended for future research efforts:

- Perform forced response analysis for the two specific crossings in order to characterize the difference in peak strain between the 5th and 6th mode. This would serve to assess whether a combined CFD/FEM analysis replicated the observed behavior. Currently, it is not known why the 6th mode exhibited stronger response than the 5th mode. One possible outcome is to addresses whether higher levels of peak strain occur when the spatial loading distribution is more closely related to the structural model shape
- Develop a simple model problem that can yield a closed-form solution for the static pressure field upstream of an imposed unsteady disturbance. The goal is to provide a more rigorous explanation for

the effect of diffusion and relative Mach number on the attenuation of the loading disturbance.

- Setup a series of physical experiments to measure the unsteady flow behavior in this centrifugal stage and record unsteady data such as blade surface static pressures. The unsteady data could then be used to assess whether CFX provides an adequate prediction of the unsteady behavior. Currently, the time-averaged performance is the only data available used to substantiate the CFX predictions.

Bibliography

[1]: Wilson, David Gordon; <u>The Design of High-Efficiency Turbo machinery and Gas Turbines</u>

[2]: Moussa, Zaher; <u>Centrifugal Compressor Aerodynamics</u>, GE Advanced Coarse Notes

[3]: Cumpsty, N.A; <u>Compressor Aerodynamics</u>

[4]: Srivastava and Macrorie; *Stage Analysis of Centrifugal Compressors for Design: CFD Validation*;

[5]: Roberts and Steed ; *A Comparison of Steady-State Centrifugal Stage CFD Analysis to Experimental Rig Data,*

[6]: Shum, Patrick; *Impeller-diffuser Interactions in Centrifugal Compressors*

[7]: Murray, Neil Paul; *Effects of Impeller-Diffuser interactions on Centrifugal Compressor Performance*

[8]: Sheng, Chunhua; *Full Annulus simulation of a high-sped centrifugal compressor using an unstructured RANS flow solver;* ASME turbo expo proceeding GT2004-53657

[9]: Smythe, Caitlin; *Forced Response Predictions in Modern Centrifugal Compressor Design*

[10]: Kielb, Robert; *CFD for Turbomachinery Unsteady Flows- An Aeroelastic Design Perspective*; AIAA paper 2001-0429

[11]: Ziegler, Kai U.; *A Study on Impeller-Diffuser Interaction: Part II-Detailed Flow analysis;* ASME turbo expo proceeding GT-2002-30381

[12] Galpin, Broberg, Hutchinson ; *Three-dimensional Navier Stokes Predictions of Steady State Rotor/Stator Interaction with Pitch Change*; Third annual conference of the CFD society of Canada, June 1995

[13] Solver Theory, Turbulence Theory: CFX Manual v. 5.7.1

[14]: Vieser, Esch, and Menter ; *Heat Transfer Predictions using Advanced Two-Equation Turbulence Models*;

[15]: Thompson; <u>Compressible Fluid Dynamics</u>

[16]: Greitzer, Tan, and Graf ; <u>Internal Flows: Concepts and Applications</u>

[17]: Wennerstrom; *Low Aspect Ratio Axial Flow Compressors: Why and What it Means*;

[18]: Phillips, Steven Michael; *A Computational Investigation of the Effect of Inlet Flow Conditions on Vaned Diffuser Performance*